Nanophotonic Structures for Coupling to Quantum Emitters in the Visible

Citation

Choy, Jennifer Tze-Heng. 2013. Nanophotonic Structures for Coupling to Quantum Emitters in the Visible. Doctoral dissertation, Harvard University.

Nanophotonic structures for coupling to quantum emitters in the visible

A DISSERTATION PRESENTED
BY
JENNIFER TZE-HENG CHOY
TO
THE SCHOOL OF ENGINEERING AND APPLIED SCIENCES

IN PARTIAL FULFILLMENT OF THE REQUIREMENTS
FOR THE DEGREE OF
DOCTOR OF PHILOSOPHY
IN THE SUBJECT OF
APPLIED PHYSICS

HARVARD UNIVERSITY
CAMBRIDGE, MASSACHUSETTS
APRIL 2013

Thesis advisor: Marko Lončar

Jennifer Tze-Heng Choy

Nanophotonic structures for coupling to quantum emitters in the visible

Abstract

This thesis is about the design, fabrication, and characterization of nanophotonic elements in the visible that can enhance light-matter interaction for single quantum emitters. We focus on two material systems: single photon sources based on the nitrogen-vacancy (NV) center in diamond with improved spontaneous emission rates and collection efficiencies, and passive TiO_2 devices that comprise a potentially broadband (from the visible to the infrared), low loss photonics platform and that are suitable for probing and manipulating single colloidal quantum dots.

We first discuss the requirements for using color center emission in bulk diamond crystals for potential applications in quantum information processing, and provide examples of using nanowire structures and planar resonators made in diamond for engineering the the NV center's pump and collection efficiencies, and spontaneous emission rates, respectively.

We also describe the integration of diamond with plasmonic structures. We have designed and implemented diamond-silver apertures for broadband enhancements of the spontaneous emission rates of NV centers. We show that shallow-implanted NV centers in diamond nanoposts provide a good system for controlling the NV center spontaneous emission rates, allowing for quenched emission with long lifetimes in the bare case, and enhanced emission with fast decay rates (corresponding to a Purcell factor of around 6) when coated with silver. We add plasmonic gratings around the diamond-silver apertures to improve the collection efficiency of the system, and observe over two-fold improvement in collection.

We demonstrate the fabrication of chip-scale linear optical elements such as waveguides and racetrack resonators in low-loss TiO_2 thin films. The fabricated waveguides operate over a wide bandwidth with propagation losses from from 30 dB/cm in the visible to 4 dB/cm in the IR, while racetrack resonators can critically couple to waveguides and have quality factors as high as ~ 22000 in the red wavelengths. We present the fabrication of dielectric slot waveguides and their integration with colloidal quantum dots. Finally, we describe efforts to study and control charge transfer processes between quantum dots and TiO_2 on a single emitter level.

Contents

Author List

Portions of Chapter 2 appeared in the following publications:

- "Diamond nanophotonics and applications in quantum science and technology," B. J. M. Hausmann, J. T. Choy, T. M. Babinec, B. J. Shields, I. Bulu, M. D. Lukin and M. Lončar, Phys. Status Solidi A, 209, 1619–1630 (2012)
- "Single-color centers implanted in diamond nanostructures," B. J. M. Hausmann, T. M. Babinec, J. T. Choy, J. S. Hodges, S. Hong, I. Bulu, M. D. Lukin, M. Lončar, New J. Phys., 13, 045004 (2011)
- "Design and focused ion beam fabrication of single crystal diamond nanobeam cavities," T. M. Babinec, J. T. Choy, K. J. M. Smith, M. Khan, and M. Lončar, J. Vac. Sci. Technol. B, 29, 010601 (2011)

Portions of Chapter 3 appeared in the following publications:

- "Plasmonic resonators for enhanced diamond NV-center single photon sources," I. Bulu, T. M. Babinec, B. J. M. Hausmann, J. T. Choy, M. Lončar, Opt. Express, 19, 5268–5276 (2011)
- "Enhanced single photon emission from a diamond-silver aperture," J. T. Choy, B. J. M. Hausmann, T. M. Babinec, I. Bulu, M. Khan, P. Maletinsky, A. Yacoby, and M. Lončar, Nature Photon., 5, 738–743 (2011)

Chapter 4 is a manuscript in preparation and will be submitted as:

- "Spontaneous emission and collection efficiency enhancement of single photon emitters in diamond via plasmonic cavity and grating," J. T. Choy, I. Bulu, B. J. M. Hausmann, E. Janitz, I. Huang, and M. Lončar (2013)

Sections 1–4 of Chapter 5 appeared in the following publications:

- “Submicrometer-wide amorphous and poly-crystalline anatase TiO_2 waveguides for microphotonic devices,” J. D. Bradley, C. C. Evans, J. T. Choy, O. Reshef, P. B. Deotare, F. Parsy, K. C. Phillips, M. Lončar, and E. Mazur, Opt. Express, 20, 23821–23831 (2012)
- “Integrated TiO_2 resonators for visible photonics,” J. T. Choy, J. D. B. Bradley, P. B. Deotare, I. B. Burgess, C. C. Evans, E. Mazur, and M. Lončar, Opt. Lett., 37, 539–541 (2012)

Section 5 of Chapter 5 is currently unpublished and the contributors to the work include: R. Jensen, Q. Quan, M. Bawendi, and M. Lončar

List of Figures

To my family

Acknowledgments

I am very grateful for the opportunity to work with and learn from Prof. Marko Lončar during the time I have spent in his group. I came into the group with no prior experience in optics, and Marko took an active role in equipping me with all the fundamentals. During the steep learning curve in the first couple of years, I never felt isolated nor left behind because Marko was always a powerhouse of positivity and new ideas. I have enjoyed this level of support from him throughout graduate school, which has allowed me to explore different projects and remain optimistic even when specific experiments did not work. Marko's enthusiasm and generosity have permeated throughout the group, and it has been a special experience growing with the group the last six years and fostering strong kinships with my labmates along the way.

I thank Prof. Evelyn Hu and Prof. Amir Yacoby, for their support, the constructive comments on my work, and for being on my defense committee. I also thank Prof. Federico Capasso and Prof. Lene Hau for being on my qualification committee. In particular, I thank Prof. Capasso for the helpful interactions with him and members of his group about my project.

I am grateful to have found a warm research lab family in the Lončar group. I would like to first thank Birgit Hausmann for being a close collaborator on all the diamond-related projects and a caring, thoughtful friend over the years. In addition to her scientific knowledge, I have become a better researcher by working with her. I am also very grateful of the work that Tom Babinec and Birgit did in establishing the experimental diamond research efforts in the group. I thank Tom for teaching me many things about optics and optical setups. I thank Irfan Bulu for his efforts on the theoretical side of the diamond plasmonics project, and for the helpful discussions on all aspects of the work. Fabrication is a large part of this thesis, and I want to acknowledge Parag Deotare who was very generous with his time when I first started out in the cleanroom and shared his many wisdoms and tricks on fabrication. On top of that, Parag has been a kind and perceptive friend. I also thank Ian Burgess and

Qimin Quan for their collaboration on various projects and for always being available as great friends and colleagues.

I feel very lucky to be in the company of the first group of graduate students in the lab. In addition to those aforementioned, I especially thank both Raji Shankar and Yinan Zhang for the many “laughters” shared throughout my PhD and their incredible friendship. Even though we have not yet collaborated on any specific project, Raji has been a great source of advice and an empathetic listener to any troubles and successes of my experiments, and she brings this generosity and care to all aspects of our friendship. Yinan’s personality and big heart have brought a lot of smiles and indelible moments to everyday life in graduate school and his ability to find beauty in his work and the world around him has been inspiring. I also thank Ian Frank for his sense of humor and for sharing his knowledge on a diverse set of topics. I have been fortunate to work with several post-docs in the group and have learned a great deal from them, especially early on in my PhD career. In addition to Irfan, I thank Mughees Khan, Murray McCutcheon, Dan Floyd, and Osman Bakr in this regard. Over the last year, it has been a pleasure to work with I-Chun Huang, Srujan Meesala, and Erika Janitz. I would like to thank the entire Team Diamond in the Lončar group, especially Mike Burek, Haig Atikian, Dan Ramos, Khadijeh Bayat, and Vivek Venkataraman. I thank Leonard Kogos, Wallace Hui, Anna Shneidman, Rick Leijssen, Ray Ng, Young-Ik Sohn, and Kita Shota, for their support in and out of the lab. Finally, I thank Kathy Masse and Xio Forbez for always being helpful and patient with the administrative side of things.

I have been fortunate to collaborate with many researchers outside of the group. I thank my collaborators Prof. Eric Mazur and his group, particularly Jon Bradley, Chris Evans, and Orad Reshef, for their efforts in the TiO_2 project, especially in providing the thin-film material that enabled the work. In addition, I thank Russ Jensen, Lisa Marshall, and Prof. Moungi Bawendi for their collaboration on the quantum dot project, from providing quantum dot samples to the many invaluable discussions we have had. I especially thank Russ for being a supportive collaborator and friend, and his patience and persistence on the project.

There are a few groups at Harvard and MIT that are pursuing diamond optics and magnetometry, and we have benefitted greatly from their knowledge. In particular, I would like to thank Jonathan Hodges for providing his confocal scanning program, Patrick Maletinsky, Sungkun Hong, Mike Grinolds for their experimental support on figuring out the fabrication of shallow-implanted NV structures and performing ESR measurements, and Tsung-Li Liu and Shanying Cui for their helpful suggestions on

silver film deposition. In addition to the Hu group and Yacoby group, I would like to thank members of Prof. Mikhail Lukin, Prof. Ron Walsworth, and Prof. Paola Cappellaro's groups, especially Yiwen Chu, Brendan Shields, Nathalie de Leon, Igor Aharonovich, Jonathan Lee, and My Linh Pham, for always opening their doors to discussions and technical support. I also extend my thanks in this regard to the photonics community at Harvard, especially to members of the Capasso group and Mazur group.

All devices shown here have been fabricated at the Center for Nanoscale Systems at Harvard and I am grateful to all the staff members for their help, especially Jiangdong Deng, Ed Macomber, Ling Xie, and Yuan Lu. I would like to acknowledge funding from the NSF Graduate Research Fellowship and the Center for Excitonics. I thank Element 6 for providing diamond samples, and I am also grateful for my various interactions with Dan Twitchen and Matthew Markham.

I am lucky to have a stalwart support system in all my friends in and outside of the Boston area. In particular, I thank Mikhail Kats for bringing a lot of happiness to my life, his infectious passion for science and everything else, and all the scientific insights he has shared. I thank Van Do and Monica Allen, for their companionship when fulfilling our course requirements and their friendship over the years. I also thank Mr. and Mrs. Lung who have become my surrogate grandparents during my stay at Harvard, often bringing me food and making sure that I am doing well. Music has been an important part of my life in graduate school, and I am grateful to Yaeko Miranda for keeping my interest in music alive through her violin lessons, even during the busiest of times. I would like to thank Kelley Rivoire, Jenny Zhang, and Faye Kasemset, who have moved away from Boston after college but kept close tabs on me and have provided great moral support throughout graduate school.

I am eternally grateful to my past mentors: my 9th grade teacher Dr. Dean Saghafi, who encouraged me to go into research and has been a source of life wisdom ever since, Dr. Jodi Evans, my mentor in my first experience in a professional lab, and Prof. David Cory, my academic and research advisor from college who has continually supported my professional development.

Finally, I have had the luxury of feeling the full support from my family in all my endeavors. I thank all my aunts, uncles, and cousins, many of whom have served as inspirations and role models for me throughout my life. I thank my parents and grandmother for their unconditional love and for all that they have taught me. They have worked hard to give me every possible opportunity to do well and succeed in life, and asked nothing of me but that I do the best I can and stay happy.

Chapter 1

Introduction

Engineering light-matter interactions has been the cornerstone of photonics research. For example, the ability to manipulate the optical properties of a material by modifying its structure on a wavelength-scale has led to the development of powerful tools in the fields of communications, computing, metrology, and sensing. Meanwhile, in the limit where object sizes are deeply sub-wavelength, quantum confinement leads to discrete energy levels that can correspond to optical frequencies. Such quantum systems can be found in atoms, molecules, and in the solid-state (for instance, in the forms of nanoparticles or defects in a bulk crystal lattice), and have applications in the generation of novel light sources for quantum information processing, biological imaging, and precision metrology.

For all the aforementioned applications, the speed of operation is limited by the rate of emission of the quantum system. Moreover, the emitter radiation pattern depends on its environment and is generally poorly coupled to the critical cone set by the collection optics. Therefore, to fully exploit the light emission from these quantum systems, we need to i) enhance the emission rate and ii) efficiently collect the emitted photons. Concurrently, with emerging applications in quantum communication, on-chip nonlinear frequency generation, and on-chip single molecule spectroscopy, there is need to develop chip-scale linear optical elements such as waveguides and resonators for low loss transmission and routing the signal to other optical elements.

The focus of this thesis is the development of nanophotonic tools that can strongly modify the light-matter interaction for single quantum emitters and provide an efficient interface between emitters and collection optics. The presented approaches were chosen for their potential scalability and ease of integration between the emitter and optical structure. The devices shown here mainly operate in the visible (600–800 nm), where certain solid-state emitters are known to have excellent properties and allow for room temperature operation, and sensitive detectors are widely available. However, the two material platforms used, diamond and titanium dioxide (TiO_2) are both wide bandgap materials and are transparent from the visible to the IR, so that the devices can be scaled to operate at longer wavelengths.

1.1 Outline of thesis

The thesis can be divided into two main sections: the demonstration of single photon sources based on color centers in diamond with improved spontaneous emission rates and collection efficiencies (Chapters 2–4), and the use of TiO_2 (Chapter 5) as a photonics platform from the visible to the IR.

Chapter 2 provides the background on the optical properties of diamond and the nitrogen-vacancy (NV) center, and outlines the important requirements that the proposed applications impose on the color center emission. Two particular structures that have been used to enhance the NV center emission are presented: diamond nanowires [1,4] and photonic crystal cavities, for which the design [5] and a summary of implementation approaches are discussed.

Chapters 3 and 4 describe the integration of diamond with plasmonic structures. Chapter 3 provides the introduction on plasmonics, and presents results on the modeling [6], and experimental realization [7] of diamond-silver apertures to enhance the spontaneous emission of NV centers. Chapter 4 describes a follow-up work in which plasmonic gratings have been integrated with the plasmonic apertures to improve the single photon collection efficiency.

Chapter 5 discusses the optical properties of TiO_2 thin films and describes demonstrations of chip-scale waveguides [8] and waveguide-coupled racetrack resonators [9]. Results on the fabrication and integration of colloidal quantum dots into dielectric slot waveguides are presented, followed by description of experimental efforts to study and control charge transfer processes between quantum dots and TiO_2.

Chapter 6 summarizes the results shown in this thesis and describes future experiments.

Chapter 2

Bulk and planar diamond nano-photonics

2.1 Optical properties of diamond and its color centers

Diamond is a material with excellent chemical and physical properties, and has become a versatile and powerful testbed for novel technologies in sensing and classical and quantum communications. For instance, diamond-based electronic and opto-electronic devices would benefit from having high thermal conductivity (22 W/cm/K), a large breakdown field (10 MV/cm) [10], and high carrier mobility (4500 cm^2/V for electrons and 3800 cm^2/V for holes) [11]. Meanwhile, the material hardness (10000 kg/mm) and high Young's modulus (1050 GPa) of diamond are advantageous for micro- and nano-electromechanical systems [12]. Finally, diamond-based photonics encompasses linear, nonlinear, and nonclassical platforms that exploit the material's large refractive index ($n \sim 2.4$), wide transparency window from its 5.5 eV bandgap, large nonlinearities (a Raman gain around 13 cm/GW [13]), and vast inventory of color centers [14].

Among these exciting applications of diamond is a class of nonclassical light sources based on naturally-occurring and synthetic color centers that provide the host material with unique optical and spin properties [15]. In a solid-state material, color centers generally arise from vacancies or atomic impurities that lead to defect states with optical transitions within the bandgap. Diamond provides a rigid and stable scaffold for many color centers, some of which can emit a single photon per excitation cycle at room temperature. The most studied single photon sources in diamond include the nitrogen-vacancy (NV) center [16], the silicon-vacancy (SiV) center [17], and nickel- and chromium-related centers [18,19]. While these are all two- or three-level quantum emitters with sharp emission lines in the visible or near infrared, the NV center has especially attracted a great deal of interest due to its optically addressable electron and nuclear spin states, which have long coherence times on the order of milliseconds [20] and seconds [21], respectively. These properties have made spin systems in NV centers potentially useful for applications quantum information processing and magnetometry.

The NV center is formed by a substitutional nitrogen with an adjacent missing carbon atom in the $\langle 111 \rangle$ crystal plane (Fig. 2-1a). The defect can have different charge states, the most well-known of which are the neutral (NV^0), with a zero phonon line (ZPL) at 575 nm, and negatively charged (NV^-). The electronic level scheme for the latter is illustrated in Fig. 2-1b, which shows triplet ground and excited states with a spin-conserving transition at 1.95 eV (637 nm). The ground triplet state is split by 2.87 GHz between the $m_s = 0$ and ± 1 sublevels. There is a long-lived metastable state, a singlet, which allows for interstate crossing from the excited state (preferentially from the $m_s = \pm 1$ spin state) and relaxation back to the $m_s = 0$ ground state. This provides a mechanism for spin polarization of NV centers and is the origin of optically detected state readout of electron spins. The room temperature emission spectrum (Fig. 2-2) of the NV center under above-band green excitation is characterized by a zero phonon line (ZPL) at 637 nm and broad phonon sideband that extends to around 800 nm. At low temperature (4 K), the ZPL would narrow and become more prominent [22]. Fig. 2-2 also shows contributions from single and two-phonon Raman scattering [16].

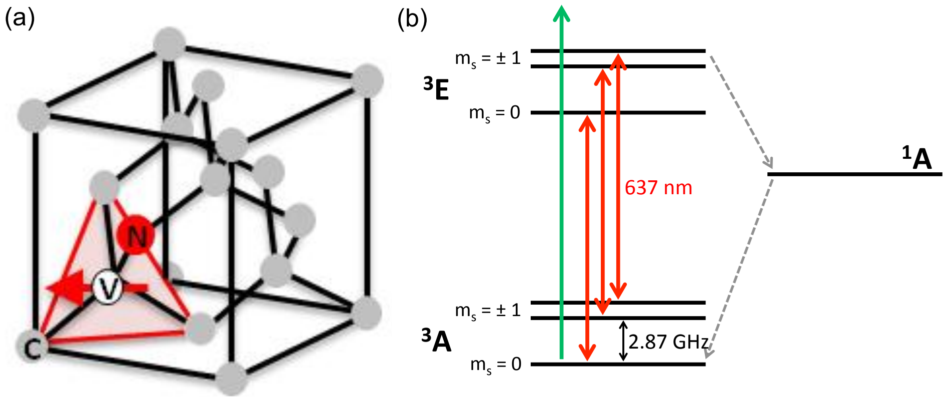

Figure 2-1: (a) Schematic of the NV center [1]. (b) Electronic level diagram for the negatively-charged state of the NV center.

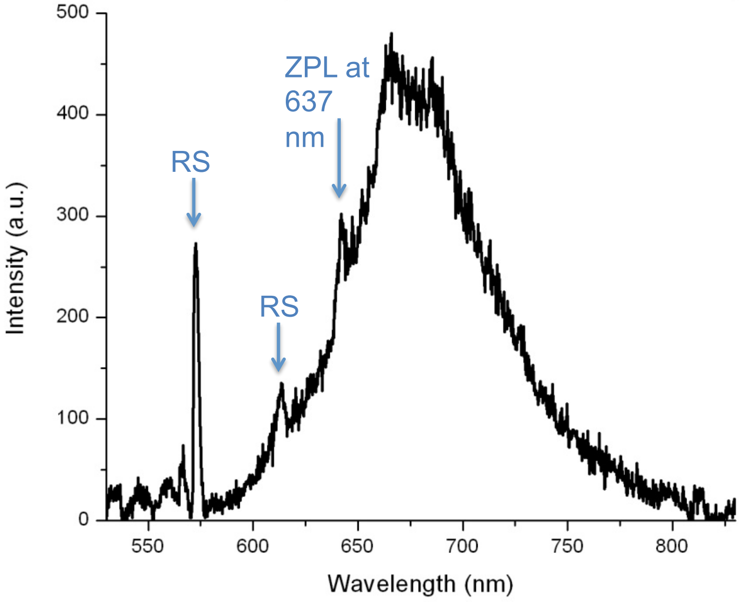

Figure 2-2: Emission spectrum of the NV center, which consists of the zero-phonon line (ZPL) at 637 nm and the vibronic sideband. The Raman scattering (RS) lines are also prominently shown.

2.2 Applications of the NV center and their requirements

Proposals and demonstrations involving the NV center in quantum information processing schemes have either used it as a pure single photon source (in quantum cryptography protocols) [23], or an interface between photons and qubits in a quantum network. Examples of the latter include using the electron and nuclear spins in the NV center as a quantum register with optical and microwave control [24–26], and using NV spins to communicate with superconducting [27] and mechanical resonators [28]. Meanwhile, NV center spins are being used for ultra-sensitive magnetometry [29–31] due to their long coherence times. All these platforms would critically depend on efficient generation and collection of photons from the NV center, and information exchange between single photons and qubits (either in all-diamond or hybrid systems). These applications have thus motivated the efforts to engineer the NV center's emission properties towards:

1. improved in- and out-coupling efficiency between emitted photons and collection optics
2. improved photon production efficiency
3. low multi-photon probability of collected photons
4. generation of transform-limited photons with most of the emission going into the ZPL

Photon collection efficiency: Efficient single photon extraction from NV centers in the bulk diamond crystal is limited by total-internal-reflection (TIR) at the diamond-air interface, due to the relatively large refractive index of diamond. In fact, TIR allows light emission within a solid-angle of less than 25° to escape the diamond crystal, so that the overall collection efficiency is only about 3%. Approaches to overcome this issue have included the fabrication of nanowires [1], and solid-immersion lenses [32–34] in bulk diamond crystals, through which the collected single photon count rates are increased by roughly an order of magnitude. In particular, the nanowire approach will be discussed in greater detail later in this chapter.

Photon production efficiency: The NV center has a relatively long radiative lifetime of 13 ns, whereas for higher repetition rates and faster operations in quantum cryptography and information processing systems, it is desirable to have an excited state lifetime closer to the sub-ns scale. To enhance the radiative decay rates, one can couple the NV center to optical cavities. The cavity-emitter interaction is illustrated in Fig. 2-3 and can be described in terms of the coupling rate g between the emitter and the cavity field, the cavity decay rate κ and the spontaneous emission rate γ.

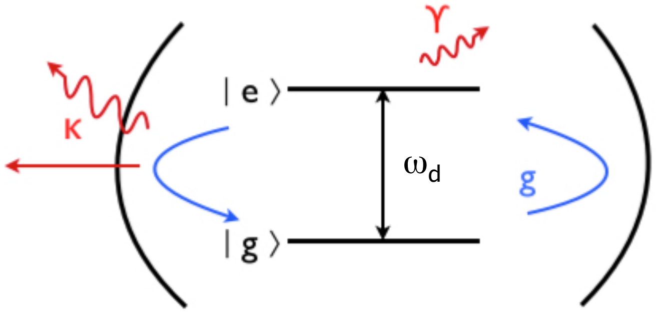

Figure 2-3: Illustration of the interaction between an optical cavity and a dipole emitter with ground $|g\rangle$ and excited $|e\rangle$ separated by ω_d.

Assuming ideal alignment in the position and polarization of the cavity and dipole, as well as perfect overlap between the emission frequency (ω_d) of the dipole and the cavity resonance (ω_c), g is $\mu\sqrt{\frac{\omega_d}{2\epsilon\hbar V}}$, where μ is the dipole moment, ϵ is the dielectric constant, and V is the mode volume. κ is related to the quality factor, Q, which describes the photon storage time by the cavity, by $\frac{\omega_c}{2Q}$. The dynamics of the cavity-emitter interaction depend on the relative strengths of g, κ, and γ. In the weak coupling regime, in which $g^2 > \kappa \cdot \gamma$, the spontaneous emission rate enhancement can be described by the Purcell factor, P_F:

$$P_F = \frac{g^2}{\gamma\kappa} = \frac{3}{4\pi^2}\left(\frac{\lambda}{n}\right)^3 \frac{Q}{V}, \tag{2.1}$$

where $\lambda = \frac{2\pi c}{\omega_d}$. Since P_F varies linearly with Q/V, a high Q and/or small V is desired, corresponding to longer interaction time between emitted photons and cavity leading to enhanced electric fields, and stronger confinement of electric fields around the emitter environment which increases the optical density of states for the spontaneous emission decay. The weak coupling regime is applicable to cases in which a large number of single photons is required, including single photon transistor/photon blockade experiments [35] [36], various entanglement scenarios [37] [38] [39], or efficient read-out from quantum registers [25] [40].

In the case of $g >> \kappa, \gamma$, we enter the strong coupling regime, in which there is coherent exchange of energy between the emitter and the cavity field, and one can no longer define separate lifetimes for the cavity and emitter. Instead, the system has a lifetime set by that of the cavity, and undergoes Rabi oscillations [41]. This limit of light-matter interaction is of interest for deterministic, on-demand, single photon sources [42].

In this chapter and the next, we will provide examples of modifying the spontaneous emission of NV centers in optical cavities under the weak coupling regime. We will also discuss the challenges and requirements for strong coupling.

Photon generation with low multi-photon probability: In quantum cryptography, low multi-photon probability is critical to secure information transfer [23]. While it is possible to emulate a single photon source by attenuating classical light sources, the probability of having only a single photon is still described by a Poissonian distribution, $P_n = \frac{\mu^n e^{-\mu}}{n!}$, where μ is the mean photon number and n is set to 1. Furthermore, the attenuation method leads to photon arrival at low bit rates. By contrast, an ideal single photon source has zero probability of emitting more than one photon at a time.

The photon statistics can be more quantitatively defined by the second-order autocorrelation function, $\mathrm{g}^{(2)}(\tau) = \frac{\langle I(t)I(t+\tau)\rangle}{\langle I(t)\rangle^2}$, where I is the intensity and $\langle\rangle$ is the expectation value. This describes the probability of detecting a photon at time $t+\tau$ given photon arrival at time t. For a classical light source, one observes bunching behavior, in which $\mathrm{g}^{(2)}(0) \geq 1$ and $\mathrm{g}^{(2)}(0) \geq \mathrm{g}^{(2)}(\tau)$ [43]. This is due to the fact that the photon stream has bunches of photons separated by intensity zeros [43]. A nonclassical source is characterized by a dip at $\mathrm{g}^{(2)}(0)$, which is known as anti-bunching, coming from the finite time between consecutive single photon arrivals. The value of $\mathrm{g}^{(2)}(0)$ is related to the number of emitters n by $\mathrm{g}^{(2)}(0) = 1 - \frac{1}{n}$, so for a single emitter, $\mathrm{g}^{(2)}(0) = 0$. In experiments, background from the sample, detector dark counts, and stray light can increase $\mathrm{g}^{(2)}(0)$, so by convention an emitter with $\mathrm{g}^{(2)} < 1/2$ is still considered a single-photon source. A representative $g^{(2)}$ curve for an NV center in experiment is shown in Fig. 2-4. It can be seen that $\mathrm{g}^{(2)}(0)$ does not vanish completely background contribution. Moreover, the bunching ($\mathrm{g}^{(2)} > 1$) observed later later times is due to shelving in the metastable state [16].

Multi-photon probability is an important metric for our devices, as will be discussed later.

Production of transform-limited photons at the ZPL: Due to the strong electron-phonon coupling that leads to a prominent phonon sideband, only $\sim 5\%$ of the overall radiative NV emission goes into the ZPL. This low branching ratio greatly limits applications of the NV center that require the generation and interaction of identical photons from multiple NV centers and motivates the use of optical cavities to enhance the ZPL emission.

In addition to enhanced ZPL emission, the linewidth of the emission needs to be fourier-transform limited to maintain coherence between emitted photons; that is,

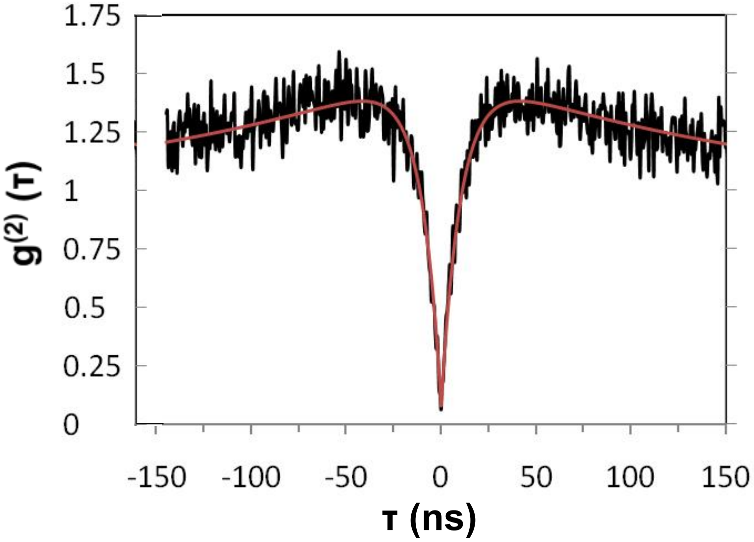

Figure 2-4: $g^{(2)}$ for a single NV center.

the time-bandwidth product, $\Delta t \Delta\omega$, needs to be near or at the uncertainty limit. Sources of decoherence include changes in the local charge environment which lead to spectral diffusion, phonon interactions, and other effects from impurities in the sample. To achieve the transform-limited linewidth of less than 100 MHz in NV centers, a low nitrogen concentration in the diamond sample [44], as well as external feedback control [45], have been implemented.

2.2.1 Material selection and approaches

While single NV centers can be found in diamond nanocrystals [46] and coupled to external optical devices fabricated in non-diamond materials [47, 48], the optical and spin coherence properties of single NV centers found in nanocrystals tend to be inferior to those in bulk diamond. For example, severe spectral diffusion of the ZPL and its broad linewidth at low temperature [49] have limited the applications of diamond nanocrystals. An alternative, enticing approach is to embed individual color centers directly in diamond-based structures. However, the realization of such a monolithic system is met with a set of material challenges associated with diamond, namely the difficulty in growing thin single crystal diamond membranes on sacrificial substrates and the physical and chemical resilience of the material.

Techniques that have bee used to fabricate devices in bulk diamond have included ion slicing, focused ion-beam (FIB) milling, and top-down nanofabrication. Ion slicing [50] has been used to realize thin diamond slabs, but damage introduced into the diamond during the process has prevented applications in quantum science. However, recent techniques based on the regrowth of single crystalline material on sliced membranes [51, 52] are promising. FIB machining sputters away material by impinging a beam of gallium ions on the surface and provides a means of sculpting a wide variety of nanophotonic structures in bulk diamond [5, 53, 54]. Despite the versatility of the method, the resulting devices are one-of-a-kind and for NV centers close to the surface, prone to damage and implantation by gallium ions. Nonetheless, functional photon devices are possible in cases where the emitter is located far away from the processed surface, such as in solid-immersion lenses [32], or with post-processing techniques [55].

Meanwhile, advances in top-down fabrication in single crystal diamond allow for three-dimensional [1, 2] and planar [55–58] nanoscale diamond structures to be made with scalability and high yield. This technique involves the patterning of an etch mask using electron beam lithography and subsequent reactive-ion etching of diamond material in an oxygen-based environment [2]. Thousands of devices can be realized in parallel this way, which suggests that the technique can eventually enable the construction of chip-scale quantum networks. Additionally, the top-down approach can be used in conjunction with ion implantation to provide deterministic positioning of color centers in nanophotonic devices [4]. The structures that are presented in this chapter and the next have been fabricated using the top-down method.

2.3 Diamond nanowires for improved photon collection

As mentioned previously, a suitable platform to increase the photon collection efficiency of color centers in bulk diamond is the diamond nanowire, which provides efficient excitation and collection channels for single photon emission by coupling the color center to the nanowire's waveguide mode. Three-dimensional finite-difference-time-domain (FDTD) simulations of the far field emission of NV centers in bulk and optimally placed in a diamond nanowire show that there is an order of magnitude increase in collection, with similar degree of enhancement in pump (Fig. 2-5a). The spectral- and polarization-averaged collection efficiency is $\sim 30\%$ for a microscope objective with a numerical aperture (N.A.) of 0.95 [2]. The optimal nanowire dimensions have a diameter of ~ 200 nm and a height of $\sim 2\mu m$. The nanowire devices were fabricated in both Ib [1,2] and IIa [4] diamond (Fig. 2-5b) using a top-down nanofabrication that is described below, which results in a high yield of working devices. Whereas Ib diamond crystals are nitrogen-rich and contain random distributions of NV centers, the nitrogen concentration of CVD-grown IIa diamond can be controlled during growth and be made very low, so that NV incorporation can be done via ion implantation and annealing. With this latter approach, we can deterministically place single NV centers in an optimal position along the diamond nanowire, by selecting the dosage and energy of the nitrogen ions.

The nanowires were fabricated by first spincoating a layer of negative electron beam resist (flowable oxide) on the diamond surface and then writing arrays of circularly shaped masks with diameters of roughly 200 nm using electron beam lithography and development in 25% Tetra-methyl ammonium hydroxide. The sample was then subject to an oxygen-based inductively coupled plasma reactive ion etching (ICP RIE) process for 10 mins which resulted in 2-μm tall nanowires [2]. The etch masks were subsequently removed using HF and the sample was cleaned in a boiling 1:1:1 mixture of sulfuric, nitric and perchloric acid. The nanowires were then implanted with ^{15}N at an energy of 1.7 MeV and a dosage of $1 \times 10^9\ cm^{-2}$ and annealed at $750°C$ in high vacuum for 2 h. The chosen implantation energy corresponds to an implantation depth of roughly 1 μm below the diamond surface.

The diamond nanowires were optically addressed in a 0.95 N.A. confocal microscope with a 532nm pump laser. $g^{(2)}$ measurements were taken with a Hanbury-Brown-Twiss (HBT) setup [1], which identified devices with single NV centers (Fig. 2-5d). To evaluate the efficiency of the single photon source, the photon count rate of nanowire is plotted as a function of pump power (Fig. 2-5c). Subtracting the linear background signal (blue) from the overall counts (red) reveals the pure NV signal (black), which can be fitted to the saturation model for the power-dependent intensity $I(P)$, $I(P) = \frac{I_{sat}}{1+P/P_{sat}}$, where I_{sat} and P_{sat} are the saturation intensity and power, respectively. For the nanowire device shown, the background-subtracted intensity saturates 304000 counts per second and the pump power needed to saturate the NV center is 0.34 mW (measured in front of the objective), corresponding to a 10-fold improvement both in photon flux as well as pump power compared to the bulk.

The high single photon flux of the nanowire combined with the low background fluorescence of the ultrapure diamond, allows us to observe sustained photon antibunching even at high pump powers. For instance, a $g^{(2)}(0)$ of around 0.1 was measured in the saturated regime without any background subtraction, which represents a more than a 5-fold reduction compared to nanowire devices demonstrated in type Ib material (Fig. 2-6).

Moreover, the combination of high directionality of emission along with low background fluorescence in the diamond nanowire suggests that it is suitable for photon collection in low N.A. and non-confocal systems. Indeed, we observed similar count rates ($I_{sat} \sim 10^5$) and anti-bunching behaviors in a confocal microscope with a re-

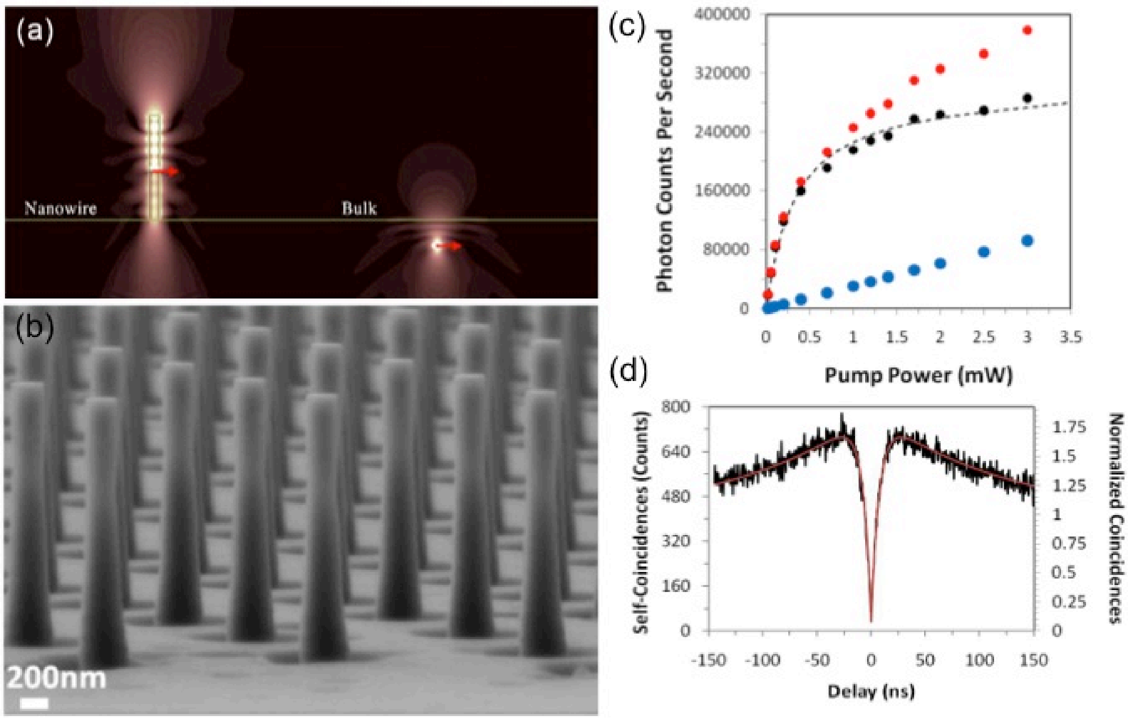

Figure 2-5: (a) Electric field profiles of an NV center in the bulk and in a diamond nanowire [2]. (b) SEM image of an array of nanowires made in electronic grade IIa diamond and subsequently implanted with NV centers. (c) Saturation curve for a nanowire device. The measured count rates, background, and their difference are plotted in red, black, and blue, respectively. Fit to the saturation model is plotted with a dotted line. (c) $g^{(2)}$ of the same nanowire device as in (b), showing that it contains a single NV center. [2].

duced N.A. of 0.6. Finally, with the purity in the material, it became possible to remove the pinhole filtering in the confocal system and collect photons using a multimode fiber (Fig. 2-7). This collection method provides us to another 3-fold increase in collected single photon emission.

2.4 Diamond resonators for modifying spontaneous emission

The nanowire geometry operates by coupling the NV center emission to a broadband waveguide mode. The intrinsic emission properties (such as the radiative decay rate)

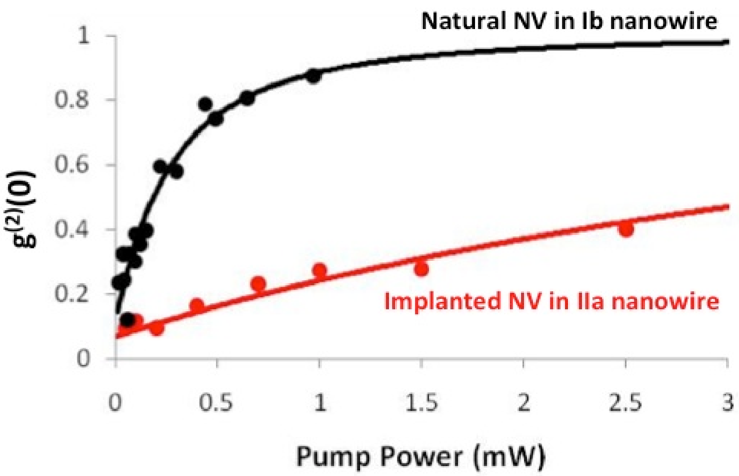

Figure 2-6: The normalized coincidence counts at zero time delay, $g^{(2)}(0)$, as a function of pump power for a single NV center in type Ib (black) and type IIa (red) diamond nanowire. The solid lines represent the expected coincidence counts 1-ρ^2 based on measured saturation data. $\rho = S/(S+B)$, where S is the NV center signal counts, and B is the background fluorescence counts.

remain unchanged. Indeed, the measured lifetime of an NV center in the diamond nanowire is $\sim$ 13 ns, which is on par with that in the bulk and corresponds to a P_F of 1. Engineering the emission rates as well as spectral profiles of the NV center would require placing the emitter in some optical cavity. Narrowband cavities such as ring resonators and photonic crystals can achieve a high Q/V ratio [59], while simultaneously providing good coupling to either on-chip channels (i.e. waveguides) [60] or free-space collection optics via grating outcouplers [61]. Here, we describe one approach to design a high Q/V photonic crystal cavity and also summarize the experimental efforts to couple color centers to these systems.

The following is a description of one of the procedures (along with [62–64]) that can be used to design a diamond photonic crystal. Our nanobeam photonic crystal device consists of a suspended diamond waveguide punctured with a regular one-dimensional lattice of air holes that defines a periodic dielectric profile. An optical cavity and localized mode is formed in the nanobeam by introducing a small shift in the relative position of two holes in the linear array (Fig. 2-8). Three-dimensional light

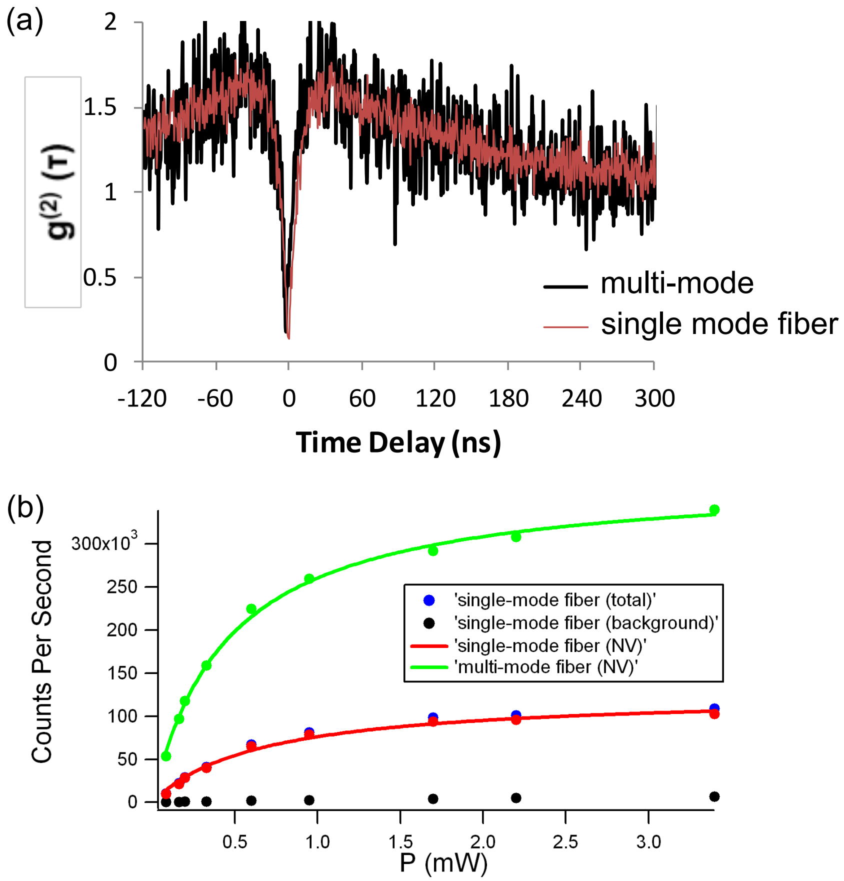

Figure 2-7: Comparison of (a) $g^{(2)}$ and (b) saturation behavior for the same nanowire as taken with a single-mode vs multi-mode fiber.

confinement is then generated by Bragg reflection along the length of the waveguide and by total internal reflection in the two transverse directions. Previous work has shown that additional engineering of the dielectric profile can suppress radiation losses at the interface between the cavity and mirror regions [65–68] if the effective index of the photonic crystal waveguide mode n_{wg} matches that of the Bloch mode $n_{Bl} = \lambda/2a_0$ in the mirrors. In practice, this can be achieved by adiabatically increasing the periodicity a of the holes away from the cavity center while keeping the hole radius r and width w of the beam fixed with respect to a. The result is a dramatic increase in the mirror reflectivity and corresponding cavity quality factor Q with only small change to the overall mode volume V. The resonance wavelength λ of the nanocavity can then be tuned via the cavity length parameter s, which is defined as the gap between the two center holes in the cavity. For each choice of mirror periodicity a, there is an optimal s at which the confinement of the cavity mode is the strongest and Q is maximized.

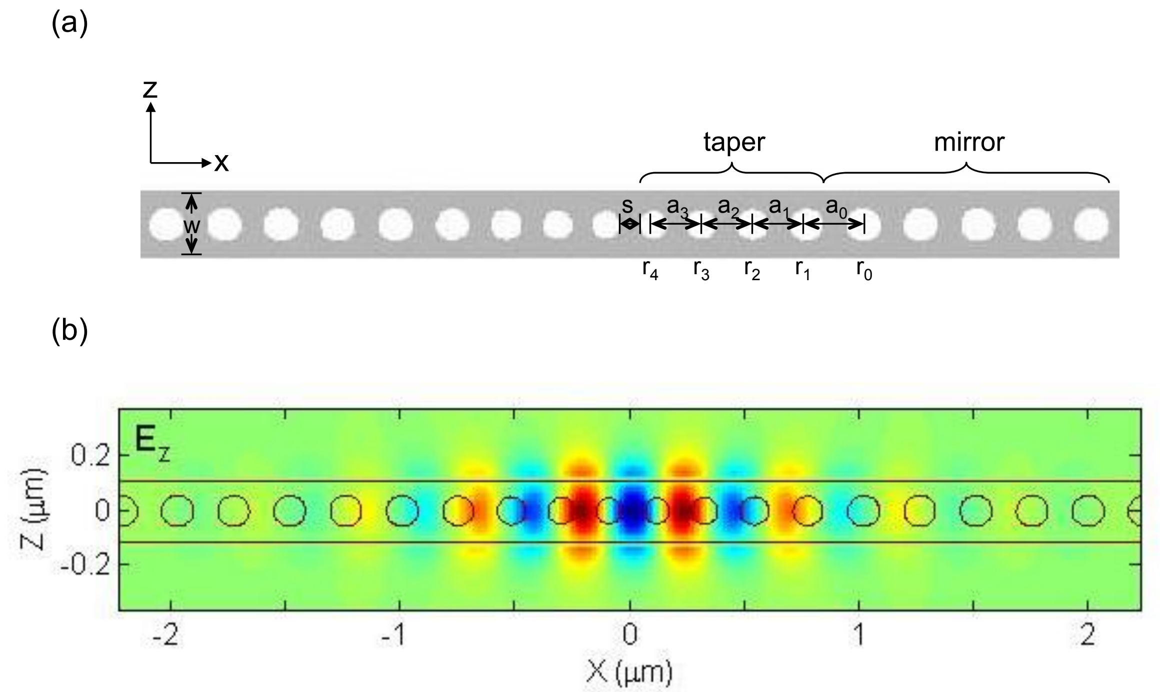

Figure 2-8: (a) Schematic of a 4-taper PhC nanobeam cavity, with the defect formed by a position shift s between the two inner holes. The taper is characterized by a linear decrease in the periodicity of the air holes around the defect. The taper and mirror regions are symmetric in x about the cavity. (b) Electric field profile of a representative cavity design with 4 linear tapers and 16 mirror pairs. This cavity has a theoretical Q of 1.02×10^6 and V of $0.41(\lambda/n)^3$. The resonant wavelength is at 637.5 nm.

We now present a concrete example of one of our air-bridge diamond nanobeam cavity designs that was modeled using a three-dimensional finite-difference time-domain (FDTD) solver (RSOFT). The thickness and width of the diamond nanobeam were set to 150 nm and 264 nm, respectively, which support a single transverse electric (TE) mode. These parameters were somewhat arbitrary and can be modified depending on sample conditions in the future. The ratio of the hole radius to periodicity was fixed at $r = 0.28a_0$ in the mirror section. For the range of $a_0 \sim 220 - 230$ nm, this resulted in a wide photonic bandgap with a ~20% gap-to-midgap ratio at red wavelengths. Finally, we considered a nanobeam cavity that consisted of 15 mirror pairs and a 5-hole linear taper from $a_0 = 225$ nm in the mirror section to $a_5 = 179$nm at the cavity center (inset of Fig. 2-9). As the cavity length s was scanned over the range 70 to 95nm (Fig. 2-9), a quality factor of $Q = 3.6 \times 10^6$ is achieved at a mode volume of $V = 0.45(\lambda/n)^3$. The resonant wavelength for optimal cavity length $s \sim 80 - 85$ nm, where the quality factor is maximized at $Q \sim 10^5 - 10^6$, is between 635 and 638 nm. This provides optimal spectral overlap between the resonator and the zero phonon line (637 nm) of the NV center in diamond.

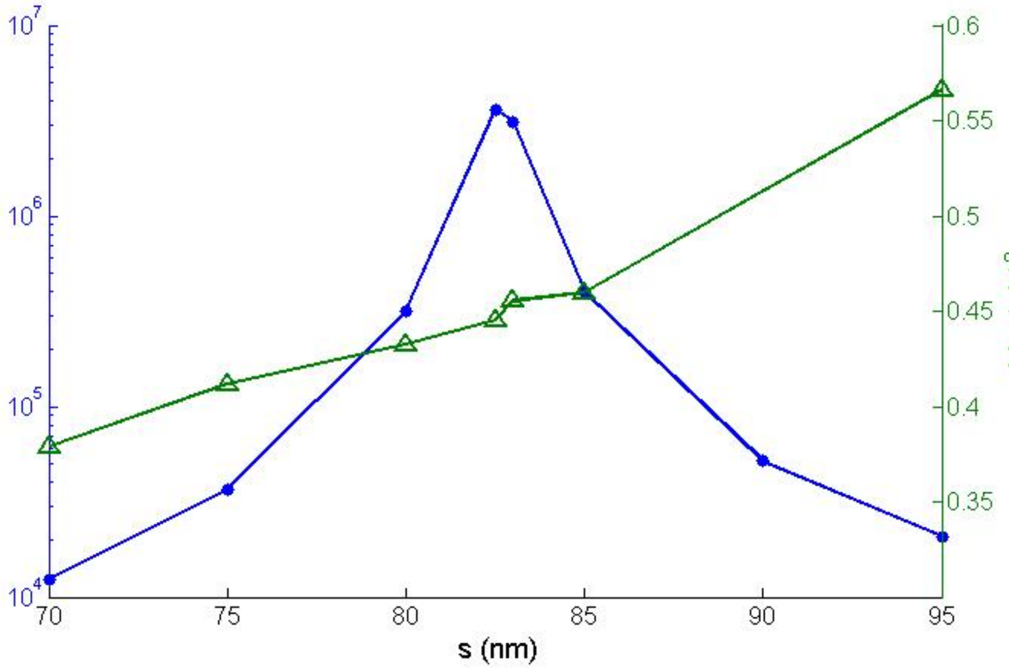

Figure 2-9: Plot of Q and V as a function of cavity length s in a 5-taper cavity with 15 mirror pairs.

The main challenge in generating free-standing or on-substrate devices such as the photonic crystal cavity presented is that mono-crystalline diamond thin films cannot be grown on-substrate. Therefore, FIB milling techniques have been used to generate free-standing photonic crystals [5,69], yielding cavity devices with fairly low Q. Recently, there have been successes in thinning single crystal diamond slabs to $< 1\mu m$ from initial thicknesses of 5-20 μm [55–57]. Based on this approach, ring resonators [56, 57] have been fabricated and characterized for the visible [56, 57] and IR [70] wavelengths, with Q's ranging from moderate ($\sim 10^4$ in the visible) to high ($\sim 10^5$ in the IR). By coupling the resonator with waveguide and grating couplers made on the same diamond chip, the generated single photons from an embedded NV center in the ring can be routed and collected efficiently off-chip. These elements form the basis of an on-chip diamond photonic network. Using a similar fabrication method, suspended photonic crystal cavities were made and coupled to single NV centers, resulting in a Purcell enhancement of around 70 at the ZPL. Finally, the combination of ion-slicing and regrowth [51, 52] and angled-etching [71] techniques are also promising.

Chapter 3

Metallic resonators for enhancing single photon emission

3.1 Introduction

In the previous chapter, we summarized approaches to couple NV centers to narrowband optical cavities in order to selectively enhance the emission into the ZPL. While this approach is ideal for applications in which a large number of ZPL photons is needed, precise spectral alignment between the cavity resonance and ZPL often requires careful tuning and the method does not leverage the inherent broad emission of the emitter. Broadband enhancement of the NV center emission might be desirable in cases that require a high overall yield of single photons and high repetition rate of the process, such as fast optical readout of the NV spin state. In this chapter, we describe an alternative approach to enhance NV center emission, by coupling the emitter to plasmonic structures. Whereas modes in photonic crystal cavities are diffraction-limited, evanescent surface waves bound to the interface between a metal and dielectric can have mode volumes much smaller than $(\frac{\lambda}{2n})^3$, thus they can strongly modify the spontaneous emission of an interacting emitter. These surface charge oscillations that are coupled to surface electromagnetic fields are known as surface plasmon polaritons (SPP) and are polarized in the transverse-magnetic (TM) direction. Due to the lossy nature of metals, structures using SPP have broad bandwidths and provide a viable platform for broadband Purcell-enhancement of NV centers.

Here, we present a geometry to couple single NV centers to guided modes in silver-coated diamond cylinders. Silver (Ag) is the material of choice since it provides the lowest loss in the visible among other metals. We will first look at the dispersion properties of surface waves that form on diamond-silver interfaces and then discuss light propagation through a diamond cylindrical structure surrounded by silver.

3.2 Diamond-silver apertures

3.2.1 Dispersion at the interface between diamond and silver

The optical properties of metal can be described using the Drude model, which assumes that a gas of free electrons of number density n moves against fixed positive ions. Under an applied electromagnetic field, electrons undergo oscillations, which are damped upon collisions with the heavier positive ions. The collisions occur at frequency γ. The complex dielectric function of the free electron gas, $\epsilon(\omega)$, is:

$$\epsilon(\omega) = 1 - \frac{\omega_p^2}{\omega^2 + i\gamma\omega}, \tag{3.1}$$

where $\omega_p = \sqrt{\frac{ne^2}{\epsilon_0 m}}$ is the plasma frequency. e and m represent the electron's charge and mass, respectively, and ϵ_0 is the electric permittivity of vacuum. For noble metals (such as gold and silver), this model is valid for a large range of frequencies from the visible (around 500 nm on) to the near- and far-IR. When $\omega < \omega_p$, the real part of ϵ is negative, and within this regime the material maintains its metallic behavior [72].

For Ag, $\omega_p = 1.37 \times 10^{16}$ rad/s and $\gamma = 7.29 \times 10^{13}$ rad/s [73]. The real and imaginary parts of the dielectric function as calculated by the Drude model are plotted in Fig. 3-1, along with vales from Johnson & Christy [74] and Palik [75]. We have also included measured values from spectroscopic ellipsometry of our sputtered films over a small range of frequencies (500–1000 nm) that are relevant to our system.

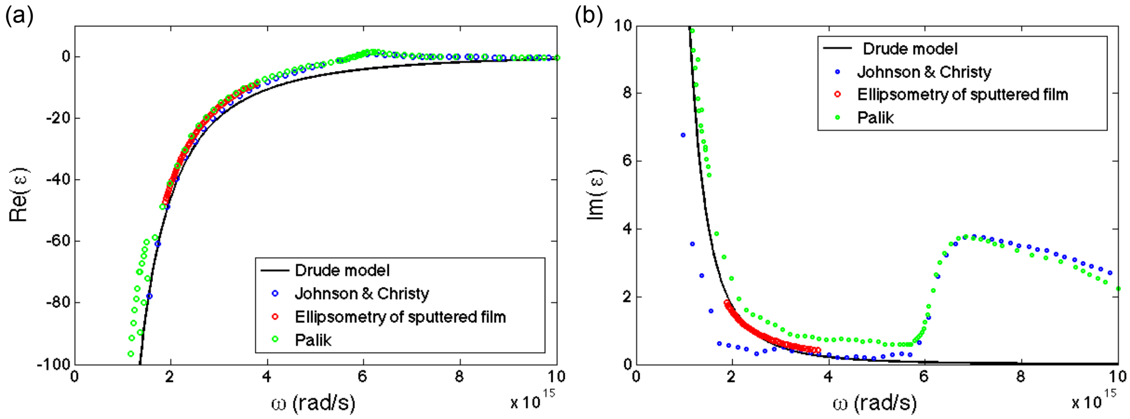

Figure 3-1: The (a) real and (b) imaginary parts of the dielectric function (ϵ) of silver.

Fig. 3-1 shows that there is generally a good agreement between the Drude model and measured data over the wavelengths of operation (shown in red). The discrepancies in the imaginary part of ϵ are likely due to variations in film quality that arise from different deposition conditions. As will be seen later, the differences would manifest mostly in the propagation lengths of the surface waves. Above $\sim 6 \times 10^{15}$ rad/s, intraband transitions occur and limit the validity of the Drude model [72].

For the rest of this discussion, we use either the values from Johnson & Christy or our measured data from ellipsometry to describe the ϵ of Ag. A flat interface between a dielectric (such as diamond) and metal (Ag) is the simplest system to support surface waves (as long as $|\epsilon_{dielectric}| < \epsilon_{metal}$). The SPP have wavevectors β which follow the dispersion relation:

$$\beta = \frac{\omega}{c}\sqrt{\frac{\epsilon_{metal}\epsilon_{dielectric}}{\epsilon_{metal} + \epsilon_{dielectric}}}, \tag{3.2}$$

where c is the speed of light. Fig. 5-7 plots the dispersion relation for both diamond/Ag and air/Ag interfaces, along with light lines in the dielectric ($\beta = n\omega/c$). The ϵ of diamond is assumed to be constant at 5.76. At large values of β, the frequency approaches the surface plasmon frequency $\omega_{sp} = \frac{\omega_p}{\sqrt{1+\epsilon_{dielectric}}}$. For the diamond-Ag system, $\omega_{sp} = 5.27 \times 10^{15}$ rad/s, corresponding to a wavelength of roughly 358 nm. At low frequencies, β lies closely beneath the light line, indicating that the SPPs are highly delocalized, with fields extending far away from the metal into the dielectric. At higher frequencies, β deviates greatly from the light line and the surface waves become very localized, with fields that are concentrated near the surface. Finally, there is a maximum wavevector as β approaches ω_{sp} due to damping in the metal [72].

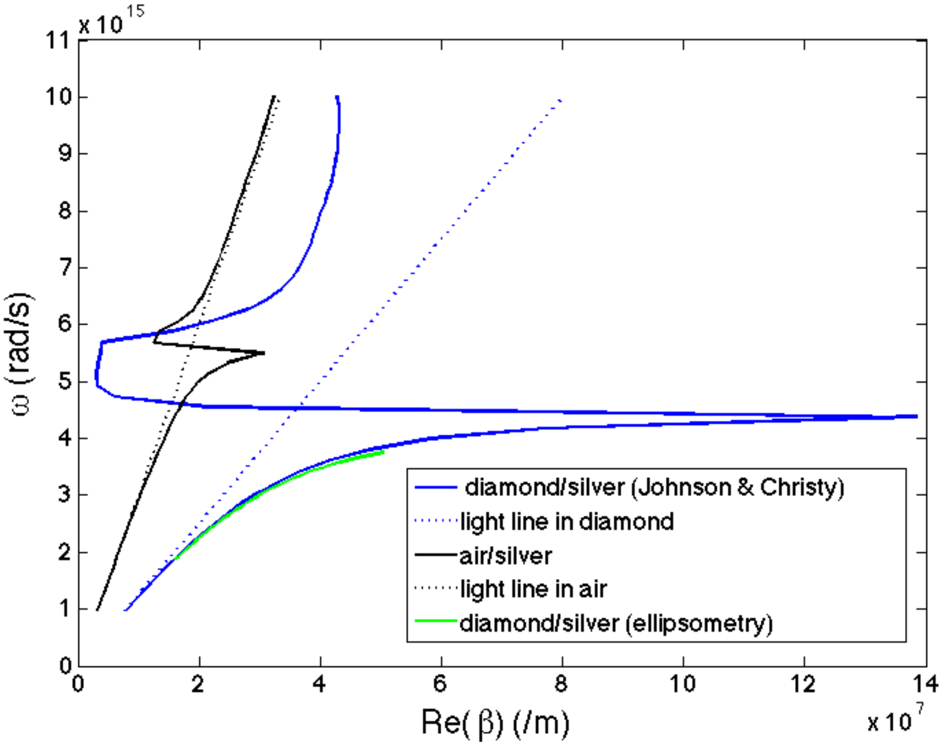

Figure 3-2: Dispersion relation for surface plasmon polaritons at the diamond-silver and air-silver interfaces. The dotted lines denote the light lines in diamond and air.

Meanwhile, both the propagation length L and decay length (L_z) in the dielectric (in direction perpendicular to the interface) can be calculated from β, using [72]

$$L = \frac{1}{2Im(\beta)} \tag{3.3}$$

$$L_z = \sqrt{\beta^2 - \epsilon_{dielectric}(\frac{\omega}{c})^2}. \tag{3.4}$$

These are plotted in Fig. 3-3. At 640 nm, the propagation length is around 3.2 μm (a bit shorter if the calculation was done with measured values; this is due to the discrepancy in the imaginary part of ϵ_{Ag}), while the decay length in the dielectric is around 60 nm. There is a direct correspondence between L and L_z, since the latter is an indication of energy confinement in the dielectric; tighter bound SPPs (with small L_z) would have shorter L. The data for the air/Ag interface are also shown, and it can be seen that there is a large difference in the values to much tighter confinement of the energy from the higher ϵ of diamond. These are important parameters to know when setting up the FDTD simulations (in the placement of the energy monitors and perfectly-matched-layers (PML) for example) to ensure that fields are not cut off before they have decayed completely.

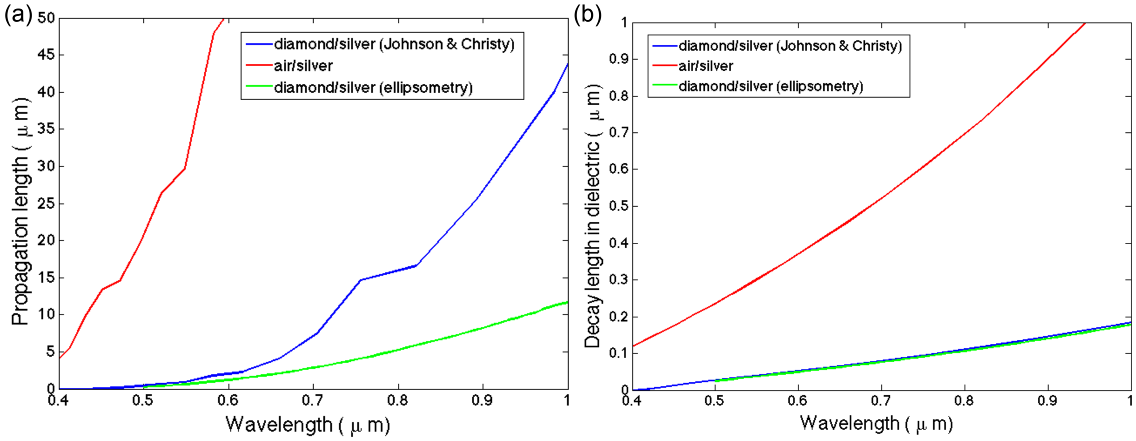

Figure 3-3: (a) Propagation length of the SPP as a function of wavelength. (b) Decay length in the dielectric as a function of wavelength.

3.2.2 Propagating modes in the diamond-silver aperture

We first solved for the propagating modes in a sub-wavelength diamond waveguide with infinite silver cladding (inset of Fig. 3-4). The guided modes of metal-clad dielectric waveguides have been previously studied [73, 76, 77] and can be found by solving Maxwell's equations in cylindrical coordinates. For simplicity, the material parameters of silver are assumed to follow a lossless Drude model. The resulting dispersion diagram, which plots the frequency as a function of the wavevector along the direction of propagation for the two lowest-order waveguide modes, is shown in Fig. 3-4. The solutions to several waveguide radii r have been calculated with r ranging from 10 nm to 80 nm. In each case, the fundamental HE11 mode is always supported near the surface plasmon frequency at 5.27×10^{15} rad/s. At $k_z = 0$, the cutoff frequency of the mode decreases with increasing radius (and is 3.084×10^{15} rad/s or 611 nm at $r = 40$ nm). At large k_z, the frequency of the mode approaches the surface plasmon frequency [77].

We also computed the real (β) and imaginary (α) parts of the propagation constants for various guided modes using the finite-element-method (FEM). Here, we used reported values for the dielectric function of silver in the literature and included losses in the metal. These are plotted as a function of waveguide radius at a fixed wavelength of 637 nm in Figs. 3-5 and 3-6. As the radius decreases, there is a transition from propagation to evanescent nature of the mode which can be seen in Fig. 3-6. For the fundamental HE11 mode, in which the mode profile is shown in the inset of Fig. 3-5, this transition/cutoff appears to occur at around 40 nm.

Based on these calculations, we can infer the confinement properties of guided modes in a silver-clad diamond waveguide (plasmonic aperture), which are considerably different from those of a dielectric waveguide. The confinement of optical field

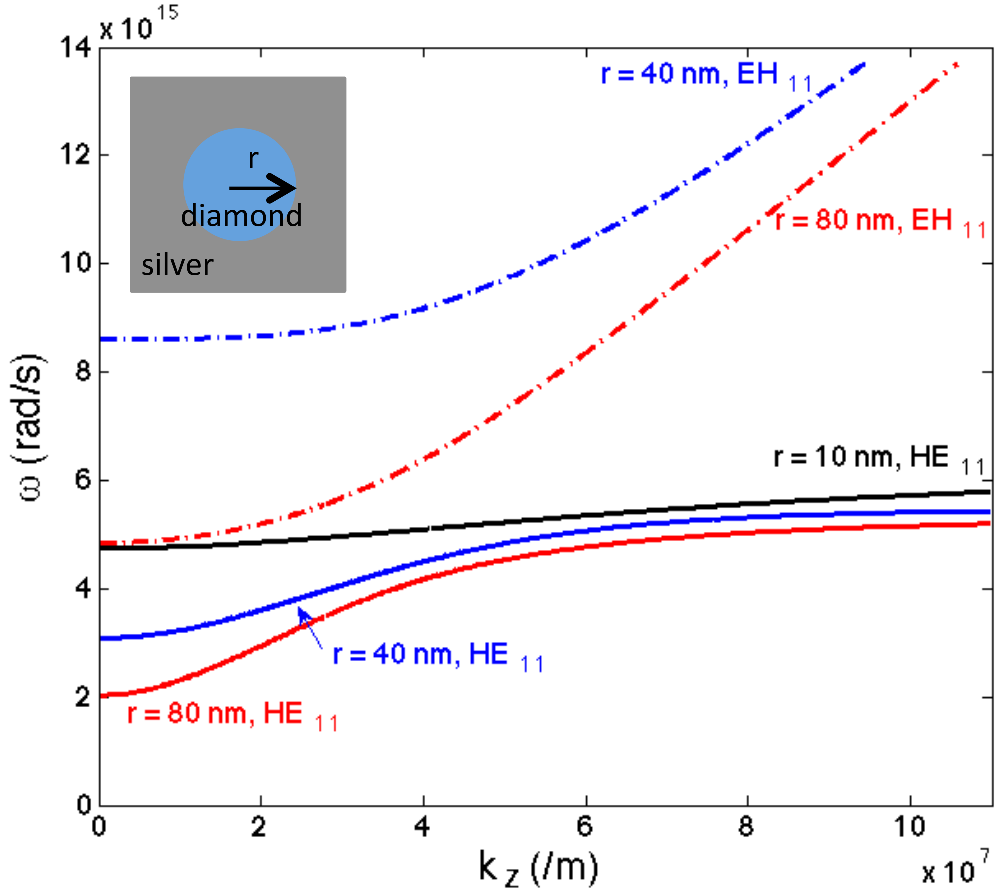

Figure 3-4: Dispersion diagram for the two lowest-order propagating modes (HE11 and EH11) in a silver-clad diamond waveguide with radius r (structure shown in inset). Here, z is the direction of propagation.

in a structure can be quantified by the effective mode area, A_{eff}:

$$A_{eff} = \frac{\int\int \mathrm{Re}\frac{d(\omega\epsilon)}{d\omega}|E|^2 dxdy}{\mathrm{Re}\frac{d(\omega\epsilon(x_0,y_0))}{d\omega}|E(x_0,y_0)|^2} \tag{3.5}$$

The mode area for the HE11 mode at 637 nm is shown in Fig. 3-7a. Unlike the delocalization of the optical mode that can be seen in the diamond waveguide with decreasing radius below the diffraction limit, A_{eff} decreases with decreasing radius in a plasmonic aperture, reaching a value as small as 0.04 $(\lambda/n)^2$ at a radius of 45 nm. The electric energy density for the plasmonic aperture is plotted in the inset of Fig. 3-7a and is maximum in the center of the core. The energy distribution is

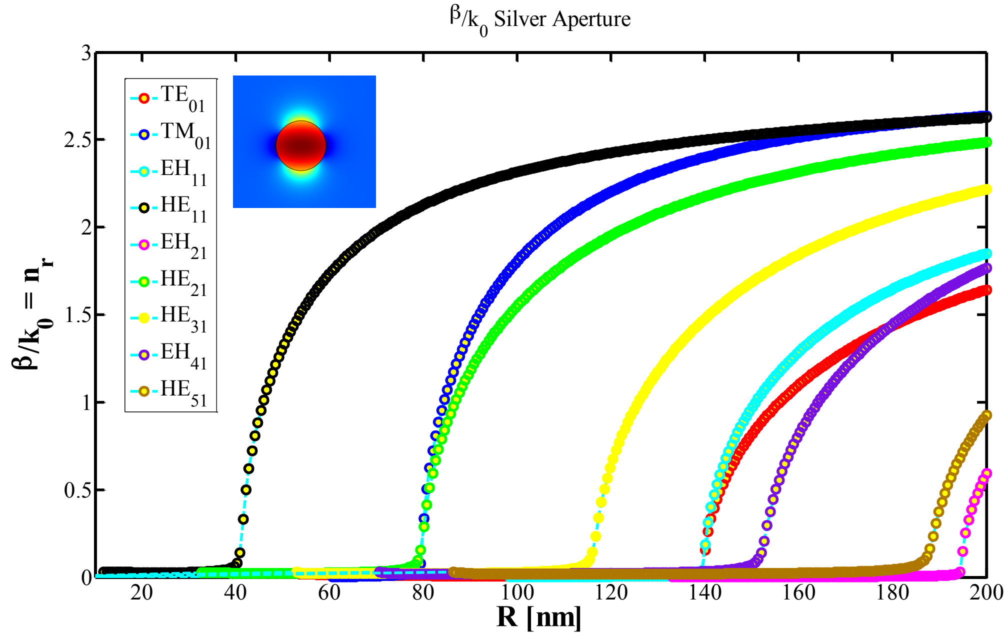

Figure 3-5: Real part of the propagation constant as a function of the diamond waveguide radius at a fixed wavelength (637 nm). Inset: electric field intensity distribution for the HE11 mode.

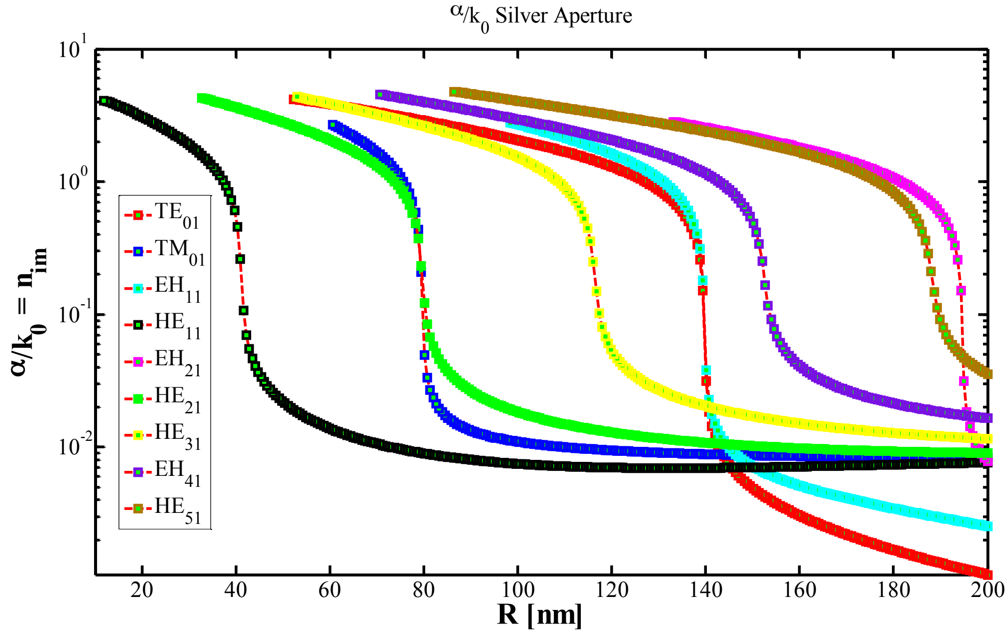

Figure 3-6: Imaginary part of the propagation constant as a function of the diamond waveguide radius at a fixed wavelength (637 nm).

fairly uniform within the core, which would facilitate coupling of a radially polarized dipole positioned almost anywhere within the waveguide. In addition, the effective mode index and propagation lengths are plotted as a function of aperture radius in Fig. 3-7b at a wavelength of 637 nm.

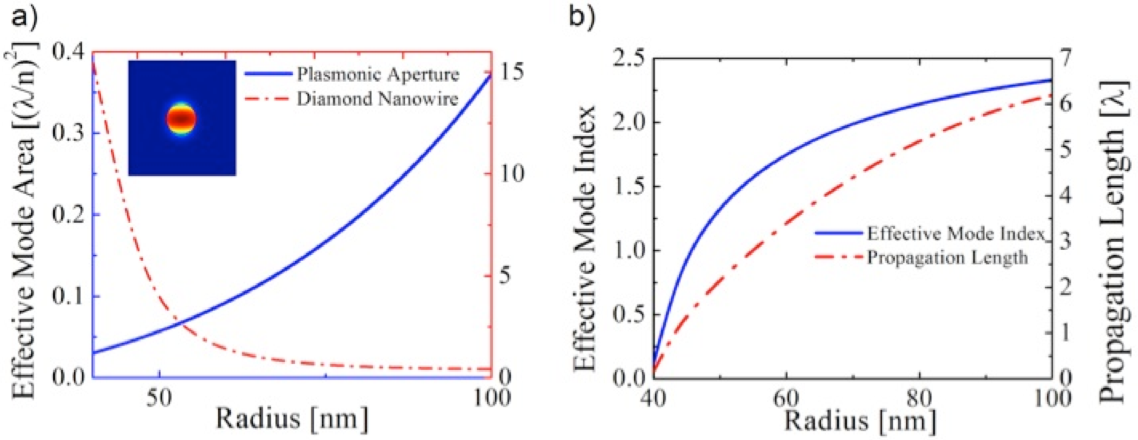

Figure 3-7: (a) Mode area for the HE11 mode of a plasmonic aperture and diamond nanowire at 637 nm as a function of radius. The energy distribution within the aperture at 637 nm is shown in the inset. (b) Effective mode index and propagation length for the plasmonic aperture as a function of wavelength.

A resonator can be formed by truncating the ends of the diamond-silver waveguide. Reflections between the facets of the aperture form broad resonances that can be tailored by changing the radius and height of the post [6]. We have designed diamond-silver apertures for coupling to the NV center emission, which will be discussed in the next section.

3.2.3 Designs for practical implementation

We consider the geometry shown in Fig. 3-8, consisting of cylindrical diamond nanoposts fabricated on a bulk diamond crystal that are embedded in a thick Ag film. The posts have radius r∼50nm and height h∼180nm. These structures support modes with mode volumes as small as $0.07(\lambda/n)^3$ and can provide good spatial overlap between the highly localized optical fields and enclosed dipole due to nearly uniform field distributions in the transverse direction. This results in the enhancement of the spontaneous emission (SE) rate of the dipole. In this design, NV emission is excited and collected through the bulk crystal. This design places the device layer away (by about the thickness of the Ag film) from the atmosphere and was chosen to mitigate issues with the rapid degradation of silver due to oxidation in ambient conditions.

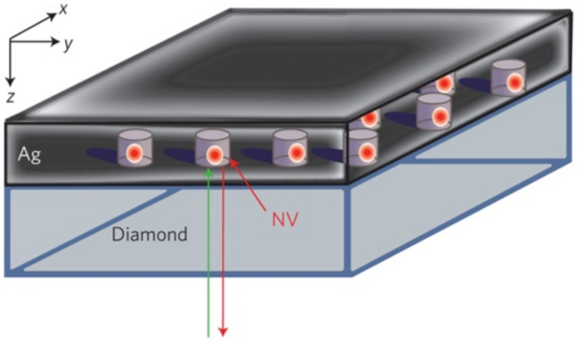

Figure 3-8: Schematic of the diamond-plasmonic system. The idealized structure for coupling to the NV emission consists of a diamond nanopost (with height∼180 nm and diameter∼ 100 nm) embedded in a 500-nm thick layer of silver (Ag). NV fluorescence is excited and collected through the bulk part of the diamond sample (green and red arrows, respectively).

The SE rate enhancements for our structures were calculated with a 3D FDTD solver using a classical approach [6] by comparing the total power emitted from a dipole when it is placed inside the aperture to the total power emitted in a homogeneous medium. In this case, the simulations were performed with measured parameters from Johnson and Christy (1972) [74] and take into account material losses in the silver. The theoretical SE rate enhancement spectrum, plotted in Fig. 3-9(d) for aperture radii of 50 nm, 55 nm, and 65 nm, exhibits a broad resonance that red-shifts with increasing radius and can therefore be tailored to overlap with the NV emission while keeping the height of the structure constant [6]. Based on our simulations, SE rate enhancements on the order of ∼30 can be expected for a radially polarized NV center placed at the maximum field intensity in an optimized structure.

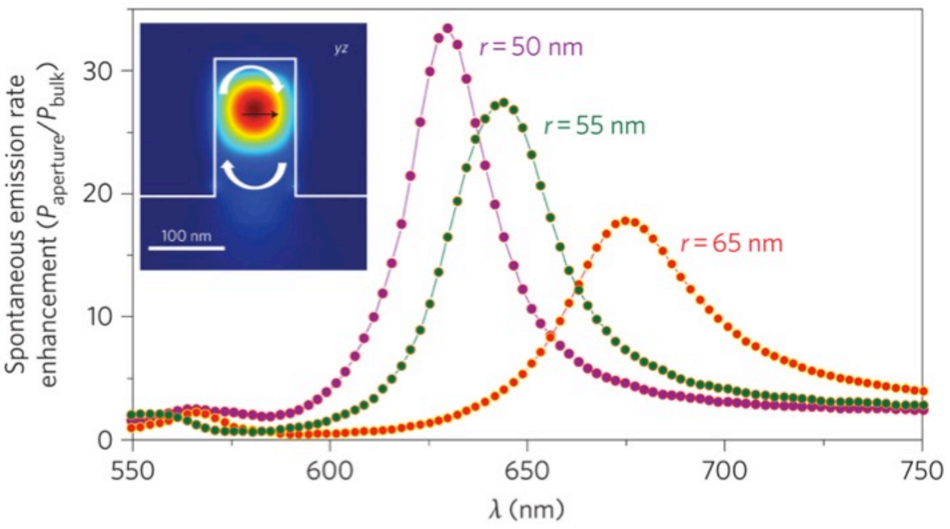

Figure 3-9: Simulated spontaneous emission enhancement as a function of wavelength for nanoposts with different radii, calculated by placing the dipole at the field maximum. Inset: Cross-sectional view of the structure along either the YZ plane, plotted with the longitudinal mode profile. The dipole is shown to be radially polarized and positioned in the center of the structure, where field density is maximized. As in a Fabry-Perot resonator, light reflects off the diamond-metal interfaces (curved arrows) and becomes tightly confined in the aperture.

3.3 Device fabrication and characterization

The hybrid diamond-metal device was realized using a combination of blanket ion implantation and top-down nanofabrication techniques [2, 4, 7, 78]. Two ultrapure bulk diamond crystals (type IIa, Element 6) were used for this experiment. The samples were implanted with nitrogen ions (at an energy of 14 keV and a dose of $1.25\times10^{12}/\text{cm}^2$ for the 20-nm implant, and at 75 keV and $1.5\times10^{11}/\text{cm}^2$ for the 90-nm implant) and subsequently annealed under high vacuum ($< 10^{-6}$ Torr) at 750 ^{o}C (20 nm) and 800^{o}C (90 nm) for 2 hours to generate a dense layer of NV centers. Arrays of diamond nanoposts of radii from 50 nm to 70 nm and height$\sim$180 nm were then fabricated using electron beam lithography followed by a 1-minute oxygen dry etch. Prior to the initial characterization, the samples were placed in hydrofluoric acid and the nitric, perchloric, and sulphuric acid bath to remove the residual mask as well as any contaminants from processing.

An SEM image of an array of nanoposts taken before silver deposition is shown in Fig. 3-10a. Optical characterization indicated that many of the nanoposts within an array emit NV fluorescence under excitation (Fig. 3-10b), with some (> 10%) showing anti-bunching below $g^{(2)} = 0.5$ (Fig. 3-10c). These characterizations were done in a home-built confocal microscope. For the autocorrelation and saturation measurements, a continuous-wave 532 nm green laser was used for excitation and focused onto the sample using an air objective (Olympus LUCPlanFLN 40x, N.A. 0.6), while both the incoming and collected signals were scanned by a steering mirror (Newport). Emitted light collected by the objective passed through a dichroic mirror and was then spectrally and spatially filtered using bandpass filters (650–800 nm) and a single mode fiber (2 × 2 coupler, Thorlabs) before being sent to avalanche photodiodes (Perkin Elmer) for photodetection and measurement of photon statistics. Spectral data were acquired using a grating spectrometer (Jobin Yvon iHR550, 76 mm x 76 mm monochromator with 150 g/mm gratings).

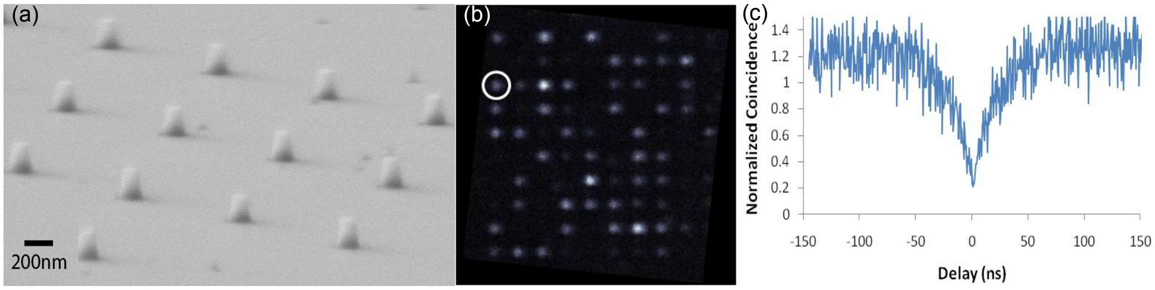

Figure 3-10: (a) Scanning electron microscope image of a representative array of diamond posts. (b) Confocal microscope scan of an array of r$\sim$ 65 nm posts before Ag deposition. The spacing between adjacent posts is $2\mu m$. (c) $g^{(2)}$ of the circled post, showing pronounced anti-bunching.

3.4 Modification of spontaneous emission rate with diamond nanostructures

We also investigated the fluorescence lifetime of the bare diamond nanoposts, using time-resolved photoluminescence measurements using pulsed green excitations. The green pulses used to trigger the decaying fluorescence signals were generated by passing ultrafast (∼200 fs) pulses at ∼800 nm from a Ti-Sapphire laser (Coherent) through a photonic crystal fiber (Newport). The resulting supercontinuum white light was spectrally filtered using bandpass filters between 510 and 540 nm (Semrock). For lifetime measurements that require longer time periods between pulses, the 76 MHz repetition rate of the Ti-Sapphire output was reduced to ∼10.8 MHz using an electro-optic modulator (ConOptics) before passing through the photonic crystal fiber. All time-correlated measurements were performed using a time-correlated-single-photon-counting module (PicoHarp).

The ensemble averaged lifetime of the densely populated NV centers in an unstructured area on the 20-nm implant sample was measured to be 16.7±0.5 ns, while that for the 90-nm implant is 14.1±0.1 ns. These values are longer than those found in the bulk (around 13 ns) due to the proximity of the emitters to the surface. The quenching effect is even more pronounced in the bare posts, in which average values of 33.3±7.5 ns for r∼65 nm and 38.3±7.3 ns for r∼50 nm nanoposts containing single NV centers were measured for the 20-nm implant sample (Fig. 3-11a). For the 90-nm implant, similar effects could be seen (Fig. 3-11b), and there is a general trend of increasing lifetime with decreasing post radius. Additionally, the longest lifetime we measured in the bare nanoposts is over 50 ns, suggesting that such a system could be advantageous for experiments requiring prolonged excited states [79].

The prolonged lifetime is due to the reduced density of states for the radiative transition as a result of the nanostructuring [80] and corroborates FDTD simulations

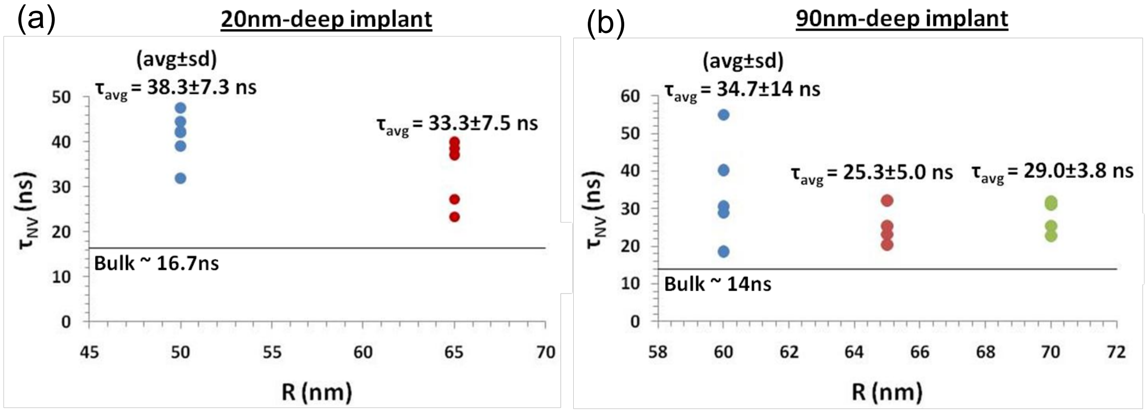

Figure 3-11: Plot of measured bare nanopost lifetimes as a function of radius for the (a) 20-nm implant and (b) 90-nm implant samples. The average and standard deviation are also shown for each post radius.

based on measured post dimensions (Fig. 3-12), in which the Purcell factor is below 1. Our calculations also indicate that the nanopost geometry leads to quenching of spontaneous emission for both the radial and axial components of the dipole, and the degree of suppression is greater in the radial case. Polarization-averaged results are shown in Fig. 3-12b.

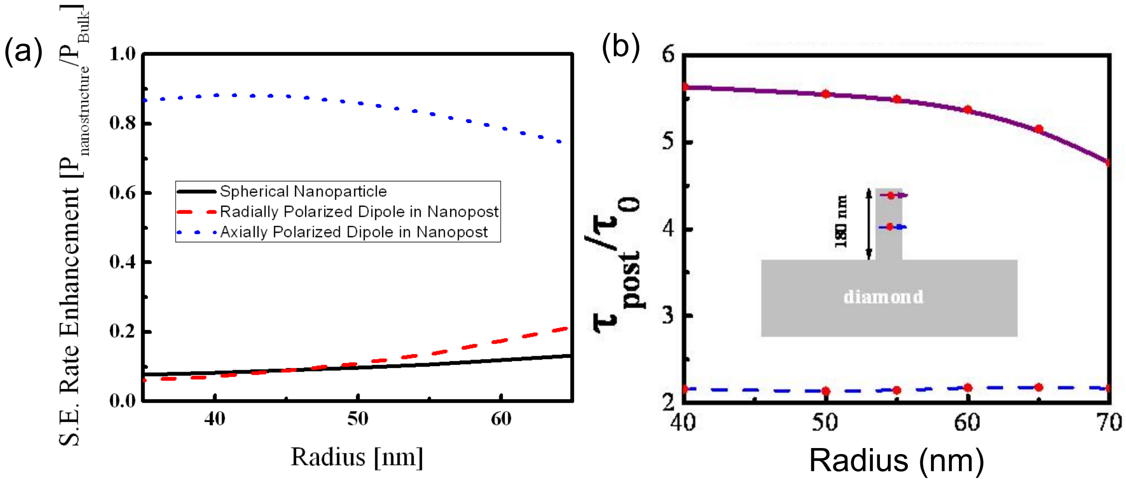

Figure 3-12: (a) Calculated Purcell factor from FDTD simulations for a radially and axially polarized emitter placed 20 nm from the top facet of the nanopost as a function of radius. This is also compared with results from a spherical nanoparticle. (b) Polarization-averaged ratio of the lifetime between the nanopost and bulk for two depths, 20 nm (purple) and 90 nm (blue).

3.5 Enhancing spontaneous emission of color centers with metallic nanocavities

A 500-nm thick Ag film was finally deposited on the nanoposts by electron beam evaporation (Denton). For the 90-nm implant sample, a 2-nm thick evaporated layer of Ti was added before the Ag deposition to provide better adhesion between the diamond surface and the metal. The samples were characterized under ambient conditions with the same confocal-microscope (N.A. = 0.6 and working distance = 4 mm) through the 500-μm thick bulk diamond material. A comparison between confocal scans taken on an array of r$\sim$65nm posts before (Fig. 3-13(a)) and after (Fig. 3-13(b)) Ag deposition under identical experimental conditions indicated enhancement of light emission by the nanoposts in the presence of Ag. The nature of photon emission was then further characterized by autocorrelation measurements to determine photon statistics and triggered fluorescence decay measurements to extract lifetime information.

For the 20-nm implant sample, we tested a total of 65 Ag-embedded nanoposts of radii 50nm and 65nm and measured each enclosed emitter's second order autocorrelation function, $g^{(2)}(t) = \langle I(t)I(t+\tau)\rangle / \langle I(t)\rangle^2$, as a function of time delay, τ, in a Hanbury Brown and Twiss experiment. Of these, five devices exhibited single photon character with $g^{(2)}(0) < 0.5$ (Fig. 3-13d, from the circled post in Fig. 3-13b). No background subtraction was performed in all data presented. In addition to the preservation of non-classical behaviour, we observed significant narrowing of the antibunching dips in comparison to those taken of nanoposts prior to Ag deposition at the same excitation power (Fig. 3-13c), which suggests an enhancement of the spontaneous emission rate due to the plasmonic cavity. However, this comparison does not take into account possible changes in the excitation rate of the NV center due to the presence of Ag and so quantitative comparison of the spontaneous emission rates would be later be performed via lifetime measurements. Another 13 devices showed

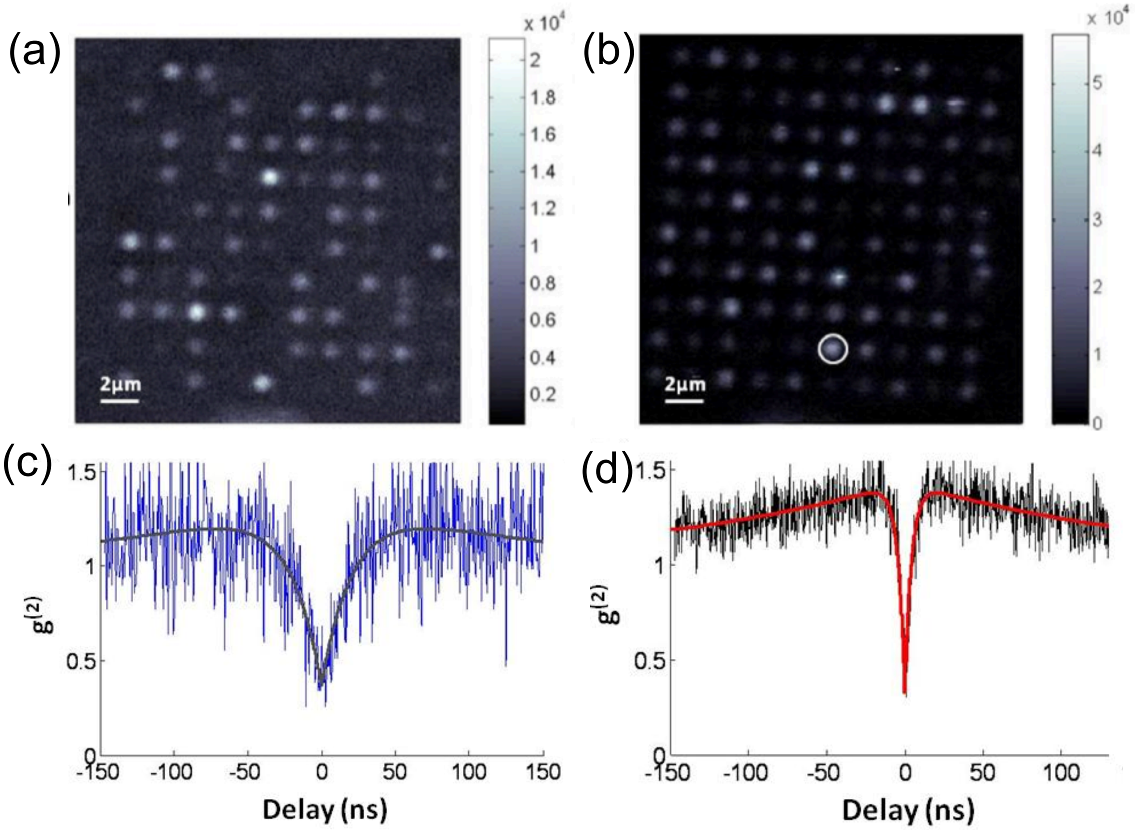

Figure 3-13: Confocal microscope scans of the same array of r$\sim$ 65 nm posts before (a) and after (b) Ag-deposition under identical pump power. The circled post represents a plasmon-enhanced device containing a single NV center. The spacing between adjacent posts is $2\mu m$. Autocorrelation function for a (c) representative bare nanopost and (d) Ag-embedded device (circled in (b)) reveal strong anti-bunching at zero time delay indicating the emission of non-classical light. Both were taken by excitation and collection through the bulk diamond crystal and no background subtraction was performed. The gray and red curves represent fits to the $g^{(2)}$ function.

some degree of anti-bunching with $0.5 < g^{(2)}(0) < 1$, although many of these had previously exhibited single photon emission in the absence of Ag. The reductions in $g^{(2)}$ contrast in these cases may be due to plasmon-enhanced background fluorescence from the Ag film. Indeed, this background luminescence was observed in spectrally resolved photoluminescence measurements performed on an “empty” aperture (without NV center). In order to improve the quality of our Ag films, we used a titanium (Ti) adhesion layer (of 2nm thickness) between diamond and Ag in the 90-nm implant sample.

A comparison of fluorescence decays measured for a representative device before and after Ag deposition is shown in Fig. 3-14a. The data were fitted to a multi-exponential mode for fast- and slow-decaying time constants. The fast ($<$ 2 ns) components are attributed to background fluorescence, while the slow time constant comes from NV photoluminescence. The fitted NV lifetimes are 37.17$\pm$0.7 ns for the bare post, 5.65$\pm$0.08 ns after it was embedded in Ag, and 16.7$\pm$0.08 ns in the bulk. The lifetimes of the NV centers implanted at 20 nm were shortened by maximum factors of 6.6 for r$\sim$65 nm posts and 4.8 for r$\sim$50 nm posts and were observed to be as short as 5.2 ns (Fig. 3-14b). For the 90-nm implant sample, lifetimes as short as 2.4 ns were measured, corresponding to roughly a 6-fold decrease over the bulk lifetime and over 10 in comparison to the bare nanopost lifetime.

The spontaneous emission rate enhancement is accompanied by an increase in the count rates which can be observed in saturation measurements. For direct comparison, we examined one set of measurements on the same 50-nm post before and after Ag deposition. In this case, we found that the bare and Ag-enhanced saturation intensities (and lifetimes) are 6.1$\pm$0.2 $\times 10^3$ cps (42.4$\pm$0.8 ns) and 4.4$\pm$0.2 $\times 10^4$ cps (9.26$\pm$0.1 ns), respectively. Therefore, the enhancements in spontaneous emission rate and fluorescence intensity are respectively 4.6 and 7.3. Since the lifetime reduction was accompanied by a comparable increase in the photon count rate, the observed plasmonic enhancement can be attributed to radiative processes. However, additional factors might be in play which led to a slight increase in the collection efficiency of the Ag-capped device, such as the out-coupling (scattering) of surface plasmon modes at the diamond/Ag interface due to the surface roughness of the metal. In comparison to single NV centers in the bulk measured using the same low N.A. setup, in which the saturation intensity is only about 23 kcps, the measured saturation intensities are roughly 2-3 times higher, with the best 20-nm implant diamond-plasmon device saturating at 1.01$\pm$0.02 $\times 10^5$ cps at a saturation power of 1.18$\pm$0.06 mW (Fig. 3-15a). In

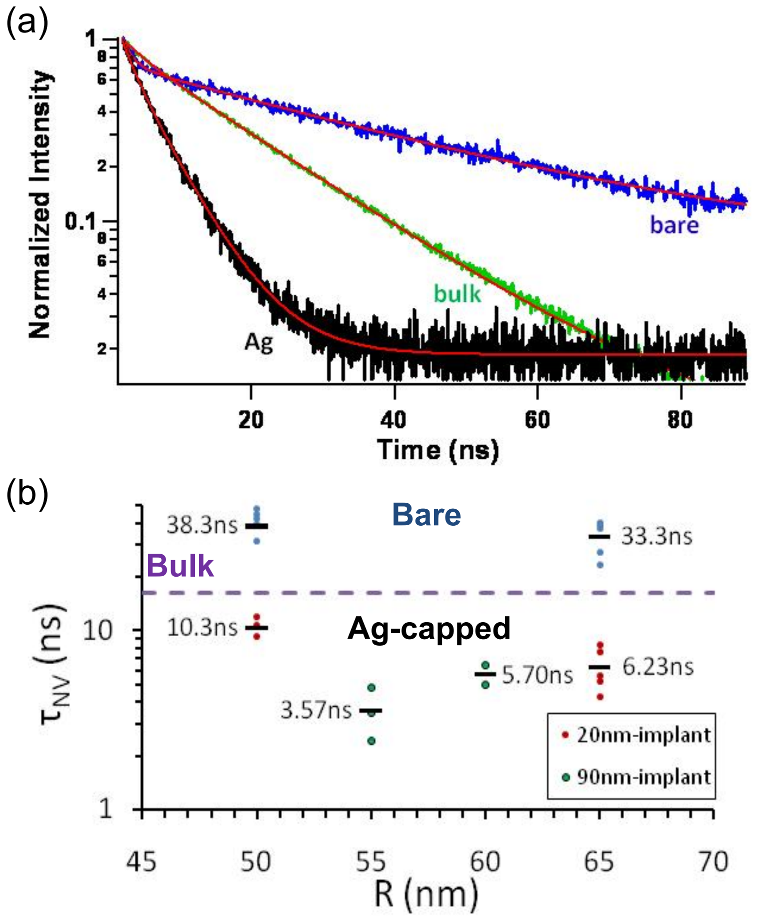

Figure 3-14: (a) Normalized fluorescence decays for the same r∼ 65 nm nanopost, containing a single NV center, before and after Ag-deposition and for an ensemble population of NV centers in the bulk region, along with fits to a multi-exponential model (shown in red). (b) Plot of NV center lifetimes for nanoposts of different radii (r) and implantation depths (z) before and after Ag deposition. The measured bulk lifetime for NV centers implanted at 20nm below the diamond surface is denoted with a dotted line.

general, saturation measurements were difficult to carry out in the shallow-implanted nanoposts, as photo-ionization of the NV centers could occur at high excitation powers ($P > 2$ mW), so that the saturation intensities could only be inferred from fitting to the saturation model.

Photoluminescence (PL) spectra taken of the Ag-embedded nanoposts consisted of the NV photoluminescence and the first and second order Raman signals of diamond (not shown). Resonance peaks could be observed after subtracting the background PL

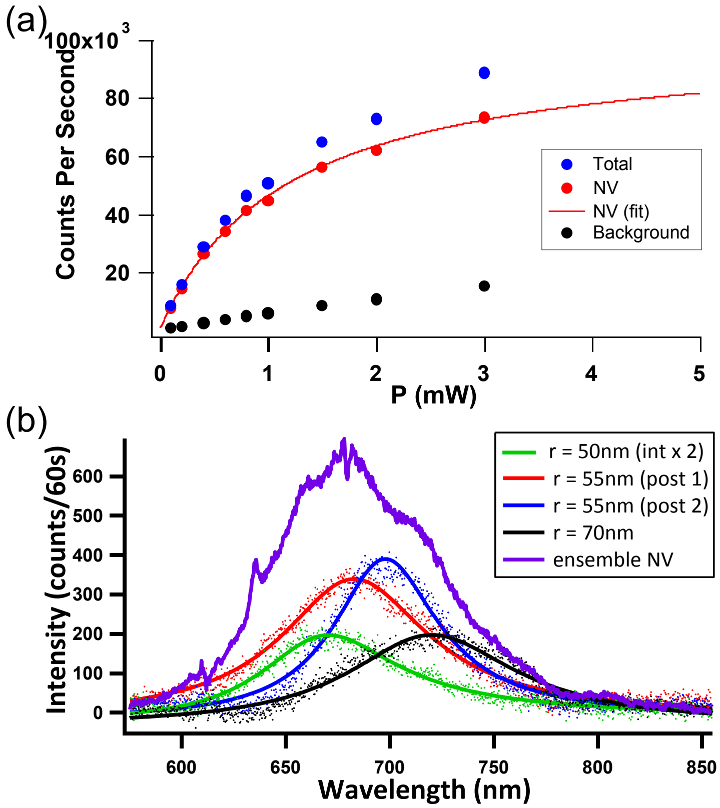

Figure 3-15: (a) Saturation curve for a Ag-embedded nanopost with an NV center implanted at 20 nm. The total count rates are represented by blue, while the background contributions (as measured from an empty post without any NV centers) are denoted black dots. Subtraction of the background from the total yields the NV emission (red dots), which can be fitted to the saturation model (solid line). The fitted saturation intensity and power are $1.01 \pm 0.02 \times 10^5$ cps and 1.18 ± 0.06 mW. (b) Background-subtracted spectra for four different devices in the 90nm-implant sample, along with a reference NV center spectrum taken from an ensemble of NV centers in a Ag-covered, unstructured region of the sample. Each solid line represents the fit to the raw data (dots). The r$\sim$ 50 nm nanopost was integrated for twice as long (120 s). The quality factors corresponding to the fits are roughly between 7 (black curve) and 11 (blue curve), while the resonance peaks range from 665.5 nm (r$\sim$ 50 nm post) and 718.9 nm (r$\sim$ 70 nm post).

(from an empty post) from the plasmon-enhanced NV center PL spectrum. For the 90-nm implanted nanoposts shown in Fig. 3-15b, the quality factors are $\sim$10, with central peak wavelengths red-shifting from 665.5 nm to 718.9 nm with increasing radius from 50 nm to 70 nm. The dispersion in resonances between similarly-sized posts (r$\sim$55nm) can be explained by the sensitivity of the resonance to nanoscale deviations in the dimensions of the devices. These deviations can include changes in the radius (for which the shift in resonant wavelength is roughly 4 nm per nm change in radius) and the side profile of the posts. These effects will be discussed in a later section this chapter.

The observed fluorescence was unequivocally assigned to NV center emission using room temperature, optically detected electron spin resonance (ESR) measurements [81]. These were performed using a confocal microscope with a 0.8 N.A. objective. Microwaves were applied using a semirigid coaxial cable which was shorted with a 25-μm diameter gold (Au) bonding wire loop. The Au wire was approached from the bottom side of the sample in close proximity of the Ag film (within a 30–40 μm distance). Bulk Ag has a skin-depth of 1.2 μm at 2.8 GHz and our 500-nm thick Ag film is therefore largely transparent to the applied RF field. Additionally, the reduced conductivity of the evaporated Ag film further enhances its transparency to the microwaves. A Rohde Schwarz SMB 100A microwave generator was used and the signal was amplified with a 30 dB gain in a Minicircuits ZHL-42W.

We observed a characteristic NV-ESR spectrum (Fig. 3-16) with a dip in fluorescence at an applied microwave frequency of 2.87 GHz with a fluorescence contrast of 18.3%. While the preservation of contrast compared to measurements on bulk NV centers suggests the viability of spin systems based on plasmon-enhanced NV emission, a critical property for both quantum information and magnetometry is spin coherence, which will have to be addressed in future experiments. However, spin coherence time can generally be extended substantially using dynamical decoupling techniques [82].

To illustrate the overall performance improvement, we have plotted the saturation intensity against the lifetime for a number of devices in the bare and Ag-capped cases at the two implantation depths. Fig. 3-17 shows a significant decrease in the lifetimes of the Ag-capped devices accompanied by an enhancement in photon emission.

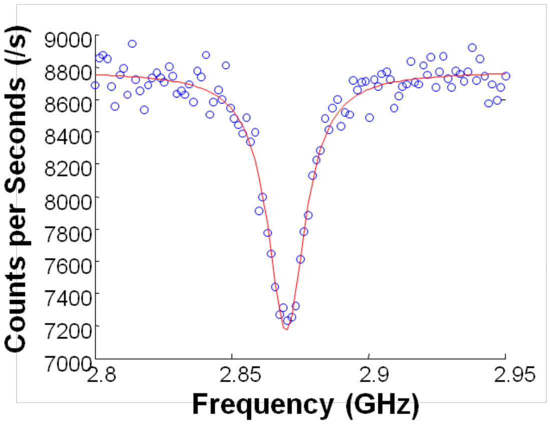

Figure 3-16: Optically detected magnetic resonance (ODMR) spectrum of a plasmon-enhanced NV center, measured by tuning the microwave source over the NV center splitting between the $m_s = 0$ and $m_s = \pm 1$ ground state levels without an external magnetic field. The spectrum reveals a characteristic dip at 2.87 GHz and a contrast of 18.3%.

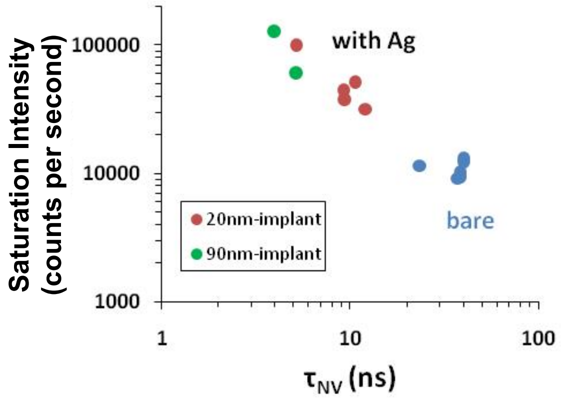

Figure 3-17: Performance plot of saturation intensity as a function of fluorescence lifetime for the bare and Ag-capped devices we tested for this study, showing that the plasmonic enhancement provided by the geometry has led to shorter lifetimes and correspondingly higher count rates.

3.6 Photon collection efficiency and anti-reflection coating

As shown in Fig. 3-17, the photon yield in our system is modest (with count rates between high 10^4 and low 10^5 cps). In addition to TIR at the diamond-air interface, photon losses in the system can be attributed to the coupling of emitted photons to surface plasmons which propagate laterally on the diamond-silver surface and could not be collected. Indeed, FDTD calculations show that only 4-5% of the emitted photons are captured by the collection optics, which suggests that further structure optimizations, such as the addition of gratings, might be necessary to increase the number of collected photons [6]. This will be explored in the next chapter.

For the current device, a straightforward approach to increase photon counts is to apply an anti-reflection coating, which reduces TIR by inducing a $\frac{\pi}{2}$ phase shift between the facet of the coating and the diamond surface that leads to destructive interference. We have designed an AR coating to eliminate the reflection at the diamond-air interface over the acceptance cone (25 degrees). For diamond, SiO_2 provides an ideal coating material. We modeled different coating thicknesses using FDTD, using a broadband point source below the diamond-air interface and averaging the transmission over the acceptance cone, and found an optimal thickness of around 130 nm. As shown in Fig. 3-18, $\sim$ 96% of light can be transmitted at the peak wavelength of the NV center emission, which is about 20% higher than the uncoated case ($\sim$77%).

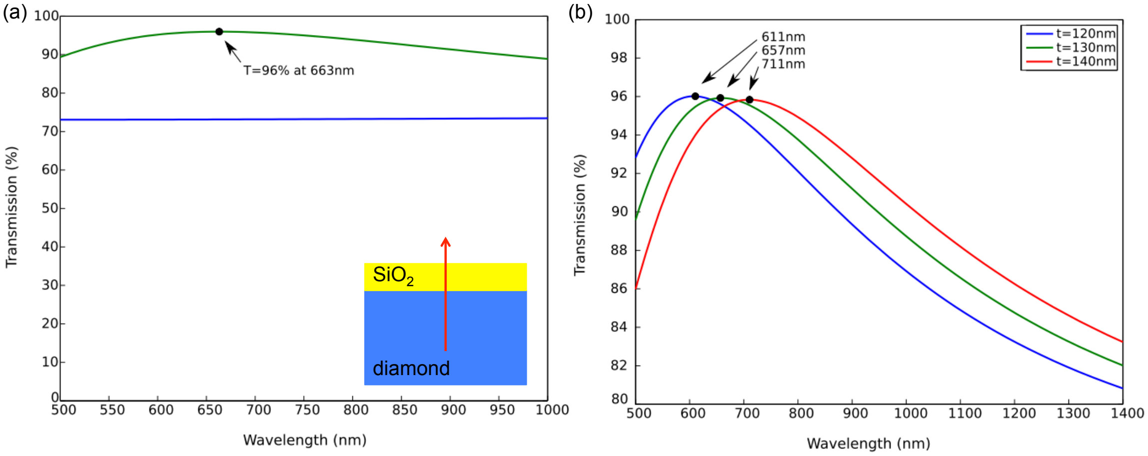

Figure 3-18: (a) Calculated transmission spectrum of a diamond-air interface with a 130-nm thick SiO_2 AR coating on diamond (green) and without any coating (blue). (b) Transmission spectra for different coating thicknesses.

We deposited 130 nm of SiO_2 on a diamond sample with silver-coated nanoposts by sputtering and measured the saturation intensities of the same NV center before and after SiO_2 deposition (Fig. 3-19). The saturation intensity and power are 138 kcps and 1.1 mW for the uncoated sample, and 151 kcps and 0.93 mW after applying the AR coating, representing about 10% and 18% improvements in collection and pump efficiencies, respectively. These data were taken on the same device under the identical characterization conditions. The discrepancy with analytical prediction might be attributed to difference between the deposited thicknesses on diamond and silicon wafer that we used to calibrate the deposition rate. Nonetheless, this is a proof-of-principle measurement that shows that AR coating is a viable approach to increase photon count rates in our devices and can be extended to other bulk geometries.

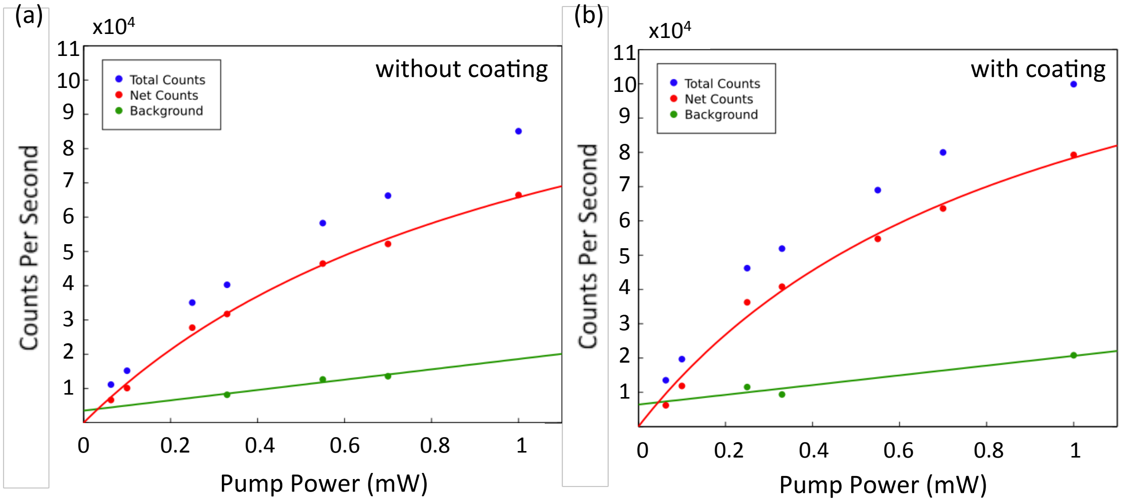

Figure 3-19: Saturation curves of the same (silver-coated nanopost) device (a) without and (b) with AR coating.

3.7 Discussion

We have demonstrated Purcell-enhanced emission for single NV centers in diamond-silver apertures. For our best 20-nm deep device, the Purcell enhancement is 6.4 and 3.2 when compared to average lifetimes in the bare nanopost and unstructured shallow implanted NV centers, respectively. For the best 90-nm deep device, the Purcell enhancement is around 6. The deviations of the observed Purcell enhancements from the predicted values (up to 30) can be attributed to geometric effects, suboptimal implantation depth and straggle, emitter spectrum, as well as ambiguity in the polarization angle of the dipole moment due to the [100] orientation of the diamond crystal plane [83].

As mentioned earlier, the resonance is sensitive to nanoscale deviations in the radius of the device. This can be seen in Fig. 3-9, in which the shift in resonant wavelength is approximately 4 nm per nm change in radius and the peak enhancement decreases with increasing radius due to reduced confinement of optical energy. Most of the devices tested in our experiments have radii in the larger end of the 50–70 nm range (due to better yield of emitter-coupled devices in larger posts) and therefore have lower Purcell enhancements. Moreover, the degree of SE enhancement is maximized when the dipole is placed at the field maximum of the aperture and drops off as its axial position changes. This is seen in Fig. 3-20, which plots the peak spontaneous emission enhancement as a function of the distance between the dipole and the top facet of the nanopost for a 305-nm tall device. Since the position of the field maximum changes with different post heights, and etch rates can vary slightly between fabrication runs, the axial position of the dipole can contribute to discrepancies between experimental and modeling data.

Finally, we investigated the effect of having slanted sidewalls in our nanoposts that resulted from our reactive ion etching process, by varying the sidewall angle (from 90 to 70 degrees) and calculating the spontaneous emission enhancement spectra for a dipole at a fixed axial position (Fig. 3-21). The resonant wavelengths red-shift with increasing taper, and the enhancement factor decreases due to reduction in the confinement of the electric field as the nanopost becomes wider (due to a larger effective post radius). For a 85° taper, which is fairly close to the geometry of the fabricated devices, the peak spontaneous emission enhancement is reduced by about 40% from the case of a straight sidewall and the resonant wavelength is shifted by

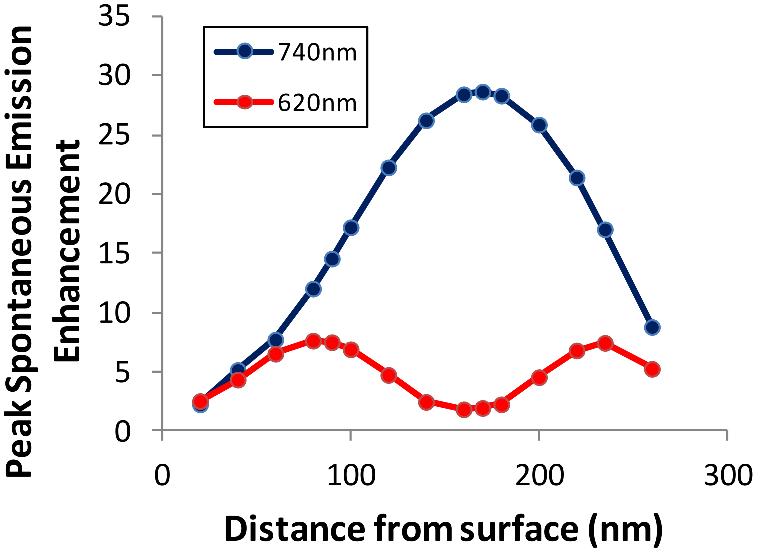

Figure 3-20: Peak spontaneous emission enhancement as a function of the dipole position below the top facet of the nanopost for the first (740 nm) and second (620 nm) order modes for the same post geometry.

about 40 nm. Tapering effect can therefore account for significant reduction of device performance. Due to the fact that the nanoposts were fabricated using a fast, 1 minute etch step, it is difficult to control the etch verticality by changing etching parameters. One way to generate straighter sidewalls might be to use angle etching techniques [71, 84] to compensate for the intrinsic non-verticality of the etch recipe.

Despite the current limitations, the method presented here provides controlled coupling in a quantum emitter-plasmonic resonator system, for a large number of devices in parallel, and has yielded Purcell-enhanced single photon emission of NV centers [7]. In comparison to existing bottom-up approaches that involve using either random (drop/spin-casting) or alignment-sensitive (pick-and-place by an AFM tip) techniques to position diamond nanocrystals, our geometry can be more straightforwardly implemented with only selection of the implantation energy and dosage. Such diamond-plasmon devices can therefore serve as a basis and proof of principle for more complex diamond-plasmon structures [6] that can potentially provide stable

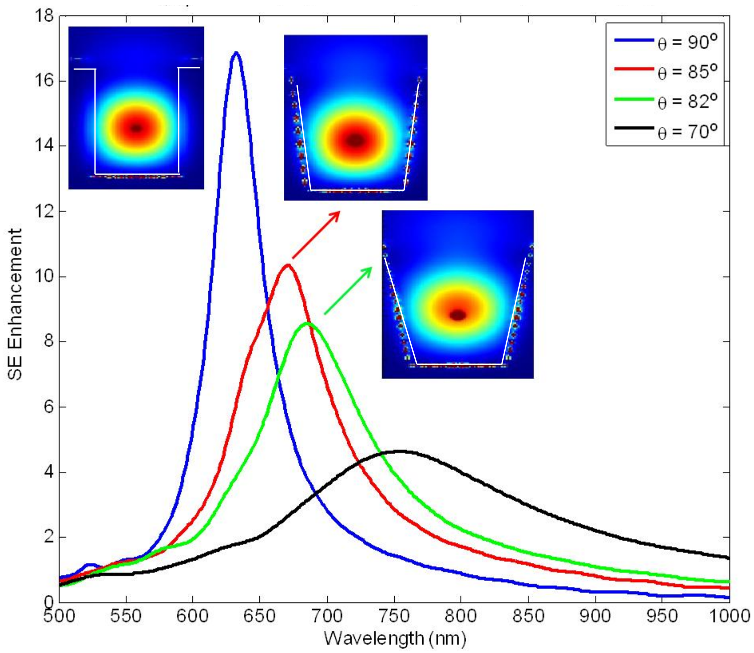

Figure 3-21: Simulated plot of spontaneous emission (SE) as a function of wavelength for different sidewall angles. In all the cases, the radius at the top (smaller) facet of the nanopost is the same and the dipole position is fixed. Insets: the electric field intensity profiles. These were taken before the dipole source has decayed completely, so there's still an intense spot in the location of the dipole.

and reliable systems for demonstrating enhanced zero-phonon line (ZPL) of the NV center, long-range coupling between qubits via surface plasmons [85], and improved optical readouts for single spin states. Finally, modified device designs [6] will allow for collimated emission resulting in larger collection efficiencies of emitted photons and potentially shaping of single photon beams on chip.

Chapter 4

Plasmonic gratings for enhancing single photon collection

In Chapter 3, we presented the “diamond-silver aperture,” consisting of a diamond nanopost covered in a silver (Ag) film, that couples single NV centers to metallic nano-cavities [6, 7]. This hybrid structure provides controlled coupling (via ion implantation and top-down nanofabrication) between the emitter and resonator and has yielded Purcell-enhanced NV emission that leads to a six-fold reduction in the radiative lifetime over bulk samples in experiment. While the fluorescence intensities from NV centers in the diamond-silver apertures have increased from those in the bulk due to faster radiative decay rates, less than 5% of the emitted photons are collected, due to losses to surface plasmons and total internal reflection at the diamond-air interface. This is shown in Fig. 4-1, a simulated plot of the different decay channels of the emission inside the aperture, including radiation modes, surface plasmons, and non-radiative channels. At around 640 nm, a significant portion of the photons, up to 50%, are coupled to the surface plasmons at diamond-silver interface. On the other hand, only around 25% of the photons are coupled to the radiation modes, with the rest being lost to non-radiative decay channels. Moreover, since excitation of the

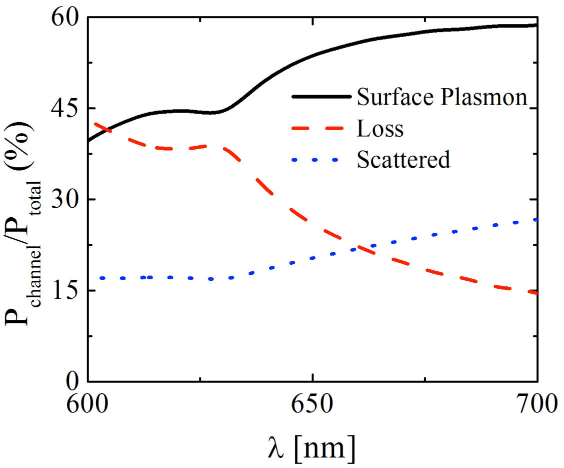

Figure 4-1: Coupling efficiency in to surface plasmons, non-radiative channels, and radiation modes.

NV center and light extraction occur through the bulk part of the diamond sample, total internal reflection (TIR) at the diamond-air interface sets a narrow (around 25 degrees) solid angle over which the NV center fluorescence can emerge from the diamond crystal. Therefore, it is desirable to engineer the directionality of the emission via periodic corrugations in the metal film which coherently scatter surface plasmons, thereby increasing the fraction of optical power going into the critical cone set by TIR [86,87]. In this chapter, we propose and experimentally demonstrate a platform to integrate these apertures with plasmonic gratings to improve the collection efficiency of the emitted single photons. We will also discuss designs that can be used to shape and collimate single photon beams on-chip.

Similar approaches [88–91] have been recently demonstrated with fluorescent molecules and quantum dots systems to provide more efficient extraction of emitted light and to manipulate the angular pattern of the radiation. For our diamond-silver nano-cavity, one possibility is to add concentric metallic rings around the diamond nanopost, such that the final structure (Fig. 4-2) consists of periodic groves in the silver film filled with a dielectric material around a central aperture (diamond). For the dielectric filler, we have selected glass (SiO_2) rather than the more obvious choice of diamond

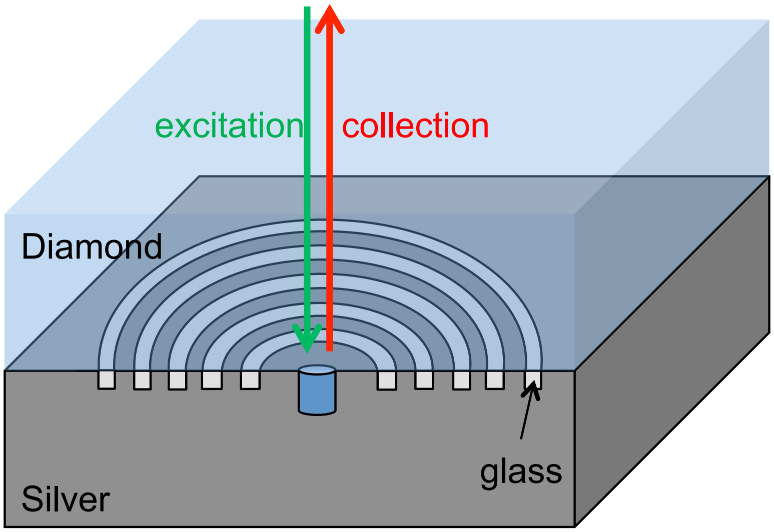

Figure 4-2: Schematic of the diamond-silver bullseye structure.

so that the gratings can be controlled independently from the diamond nanoposts. Additionally, since our sample fabrication involves using blanket ion implantation to generate a layer of NV centers, molding the grooves with SiO_2 can avoid contribution to the single photon emission by extraneous fluorescence from embedded emitters in the gratings.

4.1 Modeling

We performed three-dimensional finite-difference-time-domain (FDTD) simulations to calculate the Purcell factor, collection efficiency, and far field radiation pattern of the structures. The material parameters used for our simulations are as follows: the refractive index (n) of diamond and SiO_2 are 2.4 and 1.46, respectively. Both are assumed to be lossless over the wavelength range of interest. We performed spectroscopic ellipsometry on our deposited Ag films and determined their n and extinction coefficients (k). Our data are mostly consistent with values reported in literature (Palik and Johnson & Christy) and vary more smoothly with frequency (Fig. 3-1). This facilitates the proper construction of an analytic material model that is required for our FDTD simulation.

Ag has very small values of n (between 0.05 and 0.1 in our wavelength range of interest), which when placed next to materials with high dielectric constants such as diamond, can lead to spurious solutions due to the large index mismatch. Consequently, the simulations require very fine, sub-nm meshing, which greatly increase the computation time and make it impossible to model structures requiring a large simulation region (as in the case for grating). We found that by surrounding the diamond nanopost with a very thin ($<$ 10 nm) spacer layer of a lower dielectric constant, the solution is able to converge at a larger meshing (2 nm) and preserves the general trend of the resonator devices (Fig. 4-3a). Suitable materials include HfO_2 ($n = 1.91$), Al_2O_3 ($n = 1.67$), and SiO_2 ($n = 1.46$) and the results are plotted in Fig. 4-3b. As expected, the resonances red-shift with increasing n of the spacer material. Simulations for our grating devices were done by surrounding the center nanopost with a 10-nm thick spacer layer of Al_2O_3. This is a valid approach since our design method consists of treating the nanopost and grating as separate resonator elements, so that the center nanopost merely acts as a source and designed grating parameters should have a broadband response and operate independently of the post geometry.

In our design, the diamond aperture has radius r_d between 50 nm and 60 nm and height $h_d = 220$ nm, with a radially polarized dipole optimally placed in the field maximum of the cavity mode. As shown in Fig. 4-4a, the resonant wavelengths range from 640 nm to 680 nm, which overlap well with the zero phonon line (637 nm) and the peak emission (around 670 nm) of the NV center fluorescence, respectively. The grating design is similar to that described in [87], and consists of five grooves, each with the same width $w = 80$ nm and height $h_g = 100$ nm. The distance between the first groove and the center of the structure is $d_a = 360$ nm and the periodicity of the subsequent grooves is $d_b = 300$ nm. These parameters were selected to overlap the resonant response of the gratings with that of the center aperture, and it can be seen

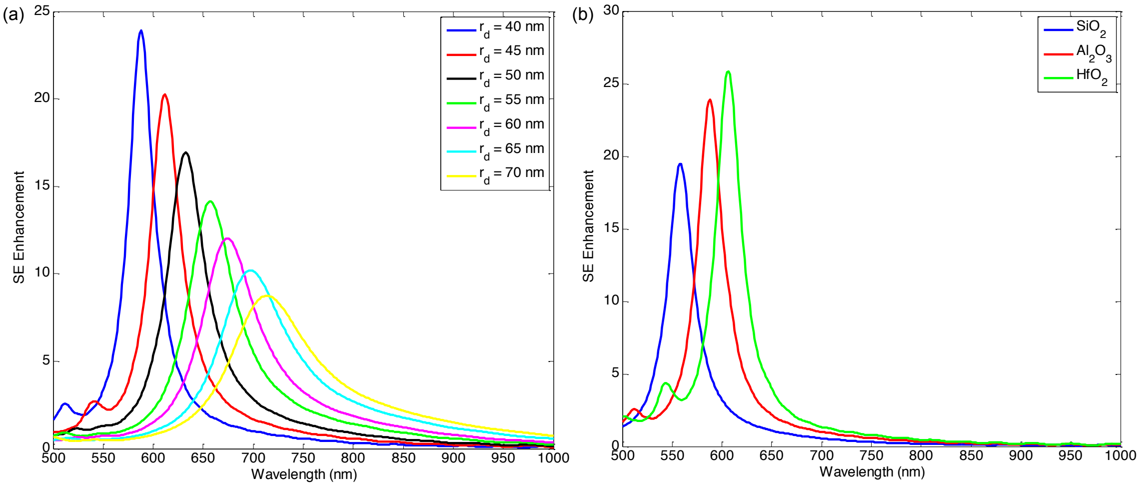

Figure 4-3: (a) Simulated spontaneous emission (SE) enhancement of an optimally placed dipole (placed at a depth of 80 nm) as a function of radius in a Ag-coated nanopost with height 220 nm. Here, a 10-nm thick spacer layer of Al_2O_3 is used. (b) SE enhancement as a function of radius in a Ag-coated nanopost (with radius 40 nm and height 220 nm) surrounded by 10 nm of each lower-index dielectric.

in Fig. 4-4a that for the same design, the addition of the grating induces only small shifts in the cavity resonance for the range of post radii we studied. The addition of the plasmonic corrugations increases the overall collection efficiency up to 16% over a broad range of wavelengths around the resonance, which represents a 5-fold improvement over the bare aperture case (around 3%). This is shown in Fig. 4-4b, and was calculated by projecting the electric fields obtained above the device into the far-field, applying the Fresnel's coefficients and Snell's law to take into account the diamond-air interface, and finally dividing the integrated power emitted into the 37-degree cone set by our collection objective over the total power emitted by the dipole. The improvement in collection efficiency is accompanied by modification of the far field profile of the radiation, in which emission is strongly concentrated at small angles (Fig. 4-4b).

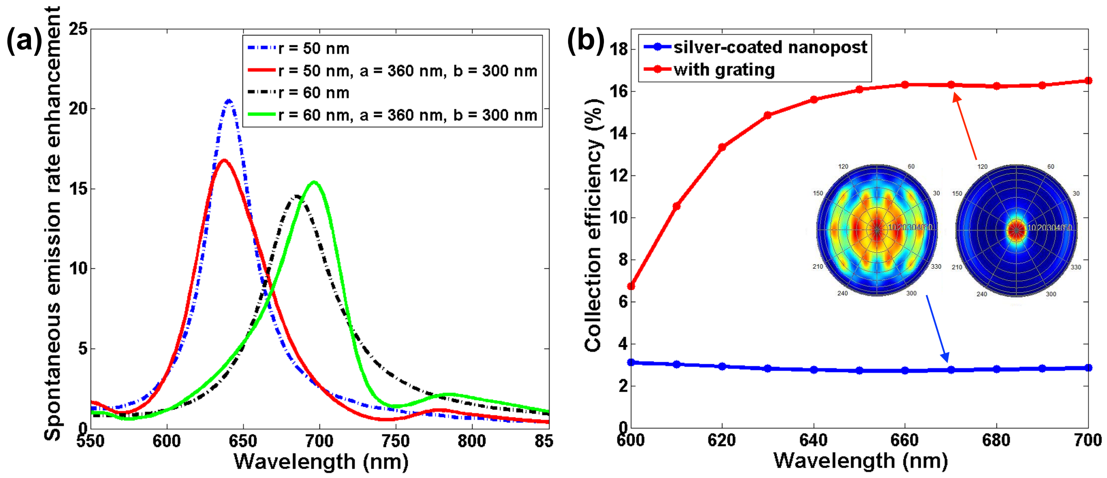

Figure 4-4: (a) Calculated spontaneous emission enhancements for the cases of silver-coated nanopost and the same-radii nanopost surrounded by grating. (b) Plot of collection efficiency by a 0.6 N.A. microscope objective as a function of wavelength for the grating (red) and non-grating (blue) cases. Inset left: simulated angular distributions for the power emitted from diamond-silver apertures surrounded by grating at a wavelength of 670 nm. Inset right: simulated angular distributions for the same-radius diamond-silver cavity at 670 nm.

4.2 Experiment

We fabricated arrays of diamond nanoposts of radii from 50 nm to 70 nm and height around 240 nm in a type IIa diamond that was implanted with a shallow layer of NV centers 90 nm below the surface, using electron beam lithography and reactive ion etching in an O_2 plasma. To realize the plasmonic corrugations, we defined rings of flowable oxide around the fabricated nanoposts in a second electron beam lithography step using a negative electron beam resist (hydrogen silsesquioxane). Scanning electron microscope images indicate that there is good overlap between the gratings and pre-existing structures (Fig. 4-5a). The images shown here are taken of a different set of samples than the ones we measured; this is to avoid introducing contamination (such as carbon deposition) to the devices during the imaging process that can lead to unwanted fluorescence. To further ensure the cleanliness and proper termination of the surface, we cleaned the diamond sample in a Piranha solution (3:1 H_2SO_4:H_2O_2)

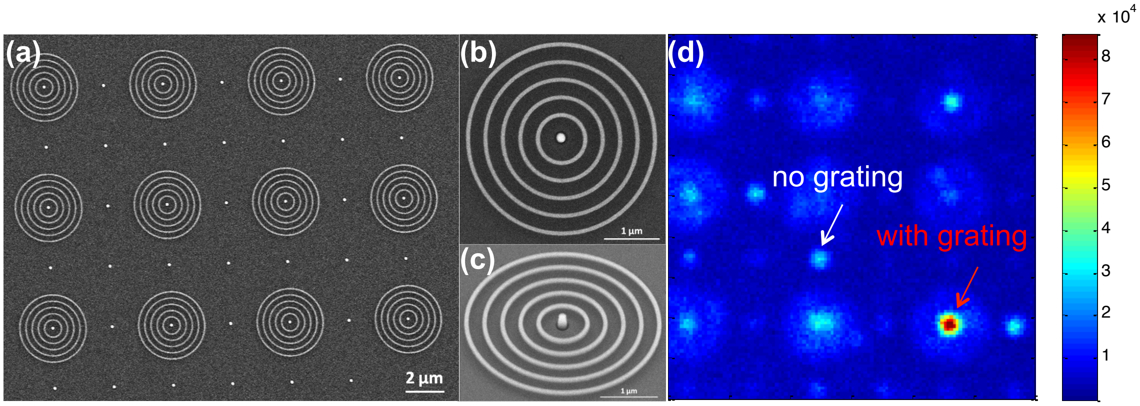

Figure 4-5: (a) Scanning electron microscope and (b) confocal scan images of arrays of diamond nanoposts in which alternating posts are surrounded by glass rings. The intensity scale corresponds to counts per second as collected by one of the APDs.

and annealed the sample at 465°C in an O_2 purged environment. The final structure was realized by capping device with sputtered Ag. After Ag deposition, the sample can be imaged on a standard optical microscope (with white light illumination through the diamond crystal onto the diamond-Ag surface) and the scattering from the grating generally has reddish colors (Fig. 4-6).

As mentioned earlier, we characterized the diamond-silver apertures by exciting the sample with a continuous wave pump laser at 532 nm and collecting the NV center emission (filtered by a bandpass filter from 650-800 nm) through the bulk diamond crystal in a confocal microscope with a 0.6 N.A. microscope objective. A scanning mirror is used to raster scan the beam across the sample, while a single mode fiber acts as a confocal pinhole and directs the collected light (after it passes through a 50/50 beamsplitter) onto two avalanche photodiodes (APDs) for detection. A confocal scan image of the sample (Fig. 4-5b) from one of the APD outputs shows that emission from posts surrounded by gratings are brighter than those without under the same pump power (around 1 mW). To confirm single photon character from individual NV centers in the structures, the photon arrival times at the APDs were recorded and plotted in a histogram of coincidence counts as a function of time delay. After normalization, we obtain the second order autocorrelated function, $g^{(2)}(\tau)$ (Fig. 4-8a).

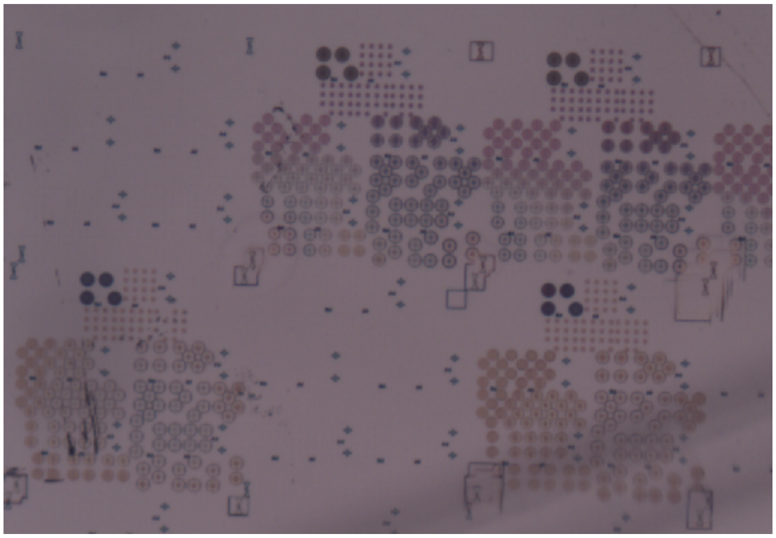

Figure 4-6: Optical image of several sets of grating devices.

For the two devices indicated with arrows in Fig 4-5b, $g^{(2)}(0) < 0.5$, demonstrating that they each contain a single emitter. These nanoposts have the same post radius of 55 nm, so that their resonator characteristics should be very similar, thus allowing us to compare the effect of the grating.

The fluorescence intensities, I, of the nano-posts were recorded under different pump powers (Fig. 4-8a). The background contribution to the fluorescence was inferred directly from $g^{(2)}$ taken at various excitation powers, using $g^{(2)}(0) = 1 - (\frac{S}{S+B})^2$, in which S is the NV fluorescence intensity and B is the background [46], and assuming that background varies linearly with pump to extrapolate the background values at specific pump powers. The details and raw data are provided in Fig. 4-7. We fitted the raw data to the model $g^{(2)}(\tau) = A(1 + c_2 e^{-|\tau - offset|\Gamma_2} + c_3 e^{-|\tau - offset|\Gamma_3})$ and obtained the values at zero delay, which along with the total count rates during the $g^{(2)}$ acquisition, give us the background values.

The background subtracted count rate corresponds to the true NV fluorescence intensity and is fitted to the saturation model, $I(P) = \frac{I_{sat}}{1+P/P_{sat}}$, where I_{sat} and P_{sat} are the saturation intensity and power, respectively. I_{sat} of the post with grating is 704±38 kcps while that for the bare plasmonic cavity is 237±17 kcps. The saturation

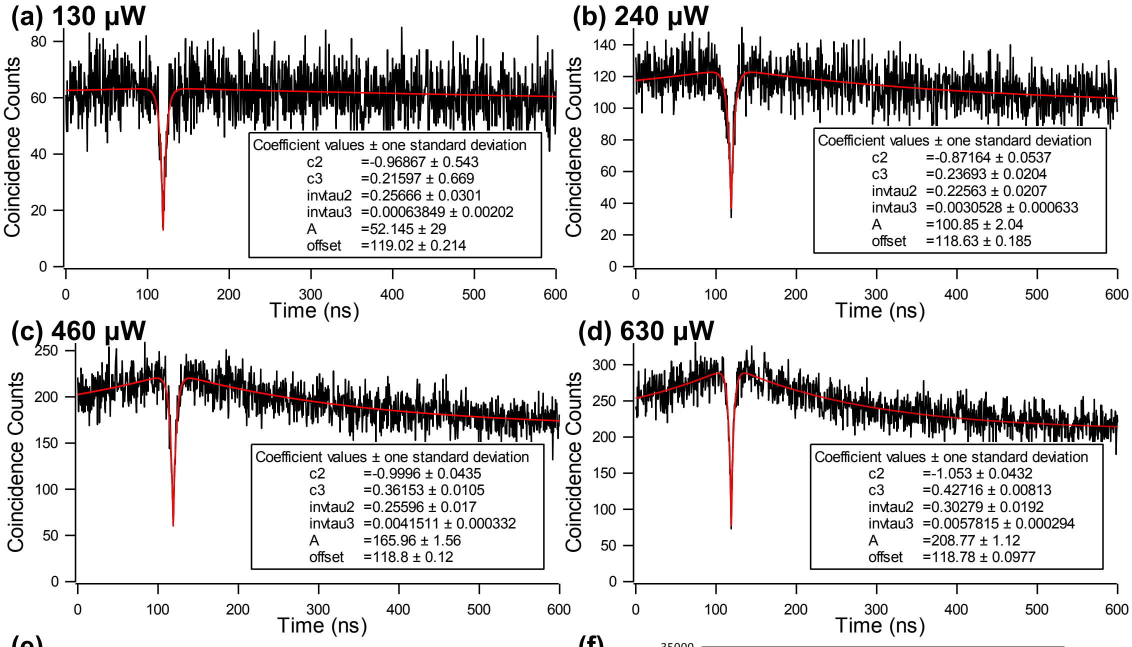

(e)

P (mW)	$g^{(2)}(0)$	$\sqrt{(1-g^{(2)}(0))}$ = S/(S+B)	B
0	-	-	170
0.13	0.25	0.87	4502
0.24	0.37	0.80	13012
0.46	0.36	0.80	21730
0.63	0.37	0.79	28201

(f)

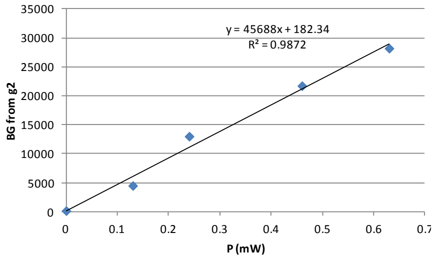

Figure 4-7: (a)-(d) Raw $g^{(2)}$ data on a grating device (shown in Fig. 4 in the main text) taken at different pump powers with fits (red). (e) Tabulated values for $g^{(2)}$ and background at different powers. *B* at zero power refers to the total dark counts from the APD. (d) Plot of background as a function of pump, with a linear fit.

power is comparable in both cases (P_{sat} around 4 mW).

Contributions to increased photon counts can be attributed to improvement in collection efficiency and/or Purcell enhancement arising from the cavity-emitter interaction. The latter can be inferred from measurement of the emitter lifetime, which was performed by recording the fluorescence intensity time trace of the nanopost under excitation by green pulses with at 76 MHz repetition rate (Fig. 4-8c). The time traces were fitted to an exponential decay model, and the resulting time constants are 3.2 ns and 2.5 ns for the non-grating and grating cases, respectively. The corresponding Purcell factors, which can be calculated from comparing the lifetime

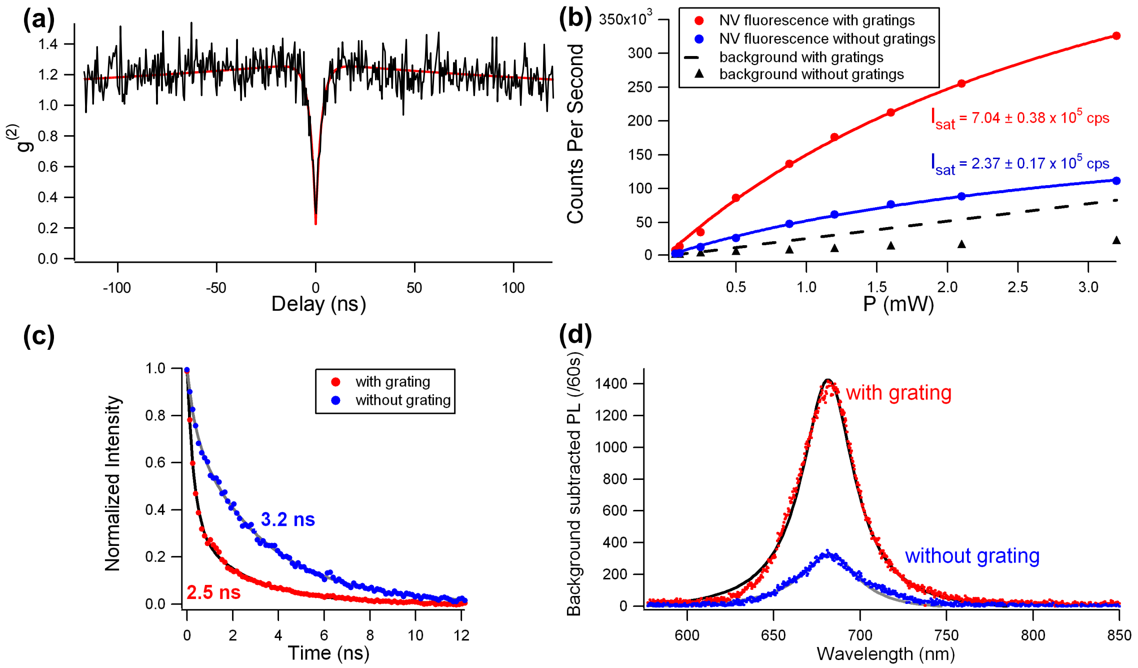

Figure 4-8: (a) Second order autocorrelation ($g^{(2)}$) plot of a diamond-silver nanopost with grating. (b) Comparison of saturation intensities, (c) fluorescence time traces, and (d) photoluminescence spectra of the grating and non-grating cases.

in cavity with that in the bulk (around 16 ns in 90-nm deep shallow-implanted NV centers), are roughly 6. That the grating case provides a shorter lifetime is likely due to the emitter being more optimally placed within the cavity. This can be seen by the photoluminescence spectra of the two devices after background subtraction (Fig. 4-8d), which shows overlapping resonances (λ_{res} around 670 nm) with similar quality factors (Q) when fitted to a lorentzian. Taking Purcell enhancements into account, the improvement in collection efficiency provided by the grating is around 2.3.

Finally, we consider the effect of the pinhole in our confocal microscope on the overall collection efficiency of the setup. While the footprint of our grating devices spans over 5 μm, the measured spot size on our confocal microscope has a full-width half-maximum of 610 nm. Therefore, some of the light scattered by the grating is not collected by our confocal system. To increase the area of collection, we replaced the single-mode fiber (SMF), which has a core size of around 4.5 μm, with a multi-mode fiber (MMF) with a core size of 62.5 μm. Since the role of the pinhole is to reduce the area and depth of collection, enlarging it would increase the area being probed in a way that is proportional to the increase in its size (the diameter of the core). However, we also sacrificed the filtering of unfocused light which led to an overall increase in background coming from the larger volume of diamond being probed. Nonetheless, as shown in Fig. 4-9a-b, the scan images taken with SMF and MMF show similar features, with increased collected count rates by several fold in the latter. To quantify this increase in a grating device with confirmed single photon character, we compared its saturation behaviors under the two collection channels (Fig. 4-9c). Due to the higher background, $g^{(2)}(0)$ is slightly above 0.5 in the MMF case (Fig. 4-10). After background subtraction, the saturation intensity is almost 4 times higher than that collected by a SMF (from 337 kcps to 1.35 Mcps), while P_{sat} is mostly unchanged between the two measurements. Photon count rates of the structures under multi-mode fiber collection are thus comparable to those obtained from nanowires ($\sim$ 500 kcps) [1] and solid-immersion lenses ($\sim$ 2 Mcps) [34].

In the case of a high background to signal ratio, time-resolved measurements can help separate emitter fluorescence and background, an example (in the form of a pulsed $g^{(2)}$ experiment) of which is given in the Appendix. Ultimately, the multi-mode fiber results suggest that the ideal scenario would be to have a pinhole with a variable size that is optimized to collect all scattered signal from the grating while still providing sufficient spatial filtering of the background.

4.3 Discussion

We have experimentally demonstrated the integration of plasmonic gratings to single NV centers in diamond-silver apertures. The observed improvement in collection

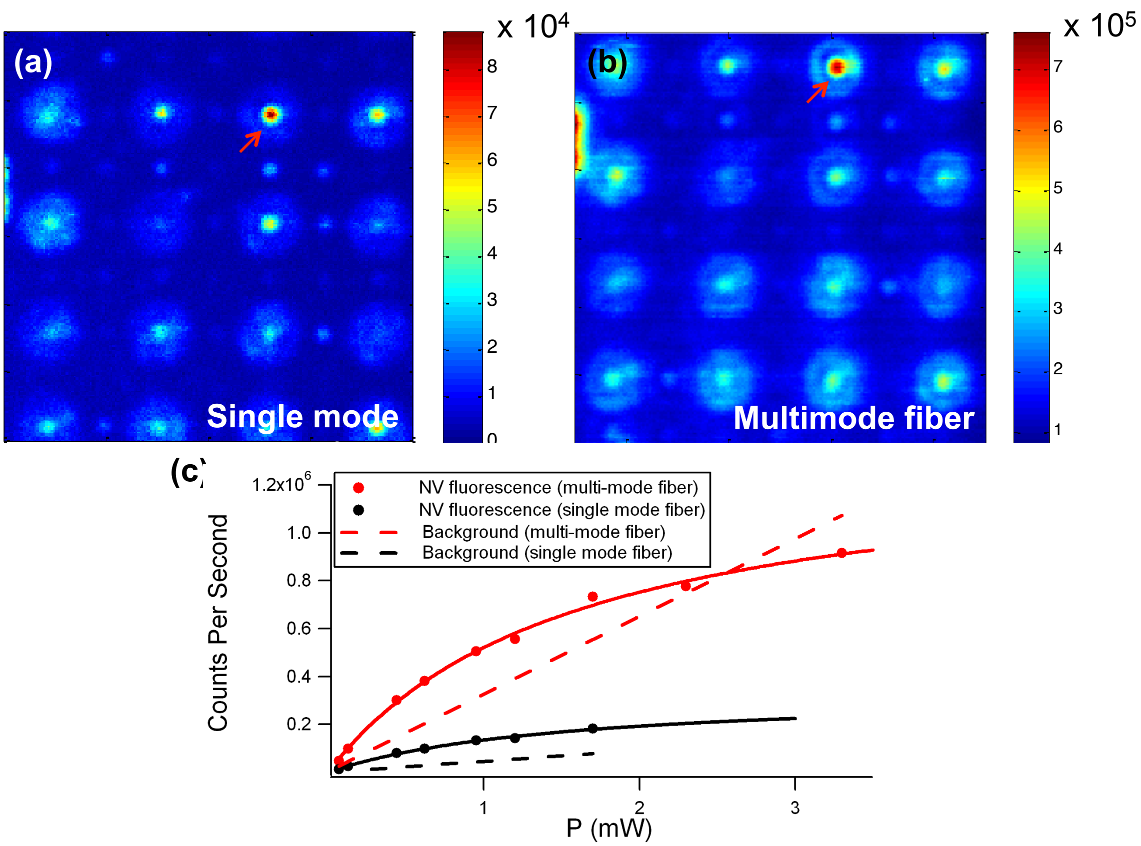

Figure 4-9: Confocal scans of the same area of the sample as imaged using a (a) single-mode and (b) multi-mode fiber at the same pump power. The intensity scale corresponds to counts per second (c) Saturation curves under collection by a single- and multi-mode fiber. The saturation powers are around 1.5 mW for both fits.

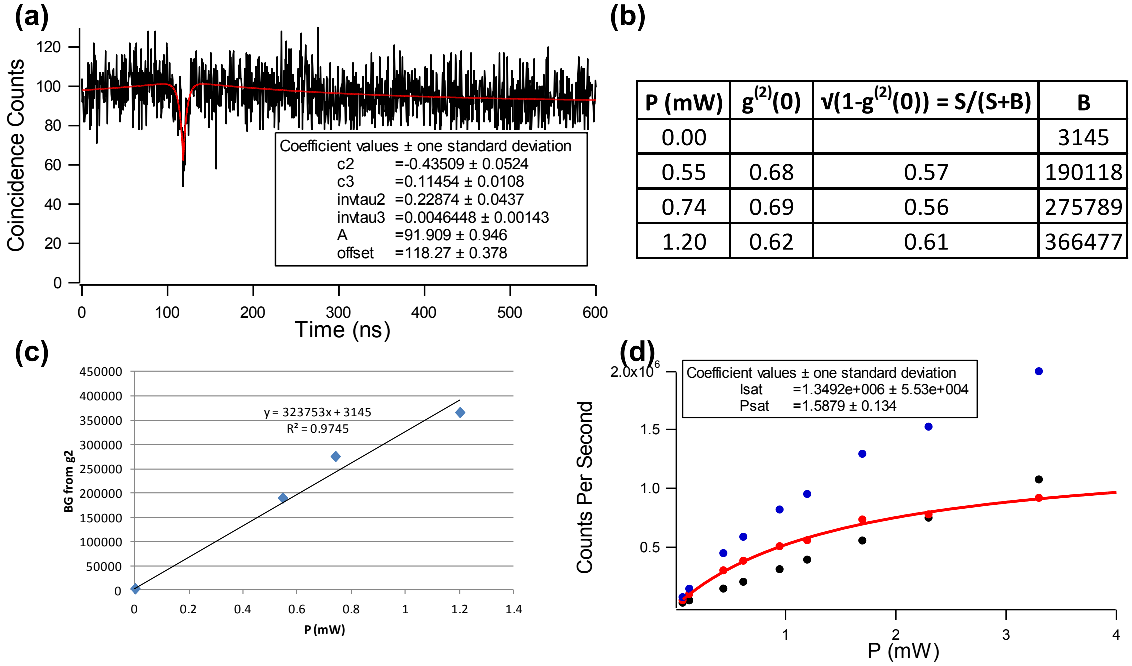

P (mW)	$g^{(2)}(0)$	$\sqrt{1-g^{(2)}(0)} = S/(S+B)$	B
0.00			3145
0.55	0.68	0.57	190118
0.74	0.69	0.56	275789
1.20	0.62	0.61	366477

Figure 4-10: (a) Raw $g^{(2)}$ data for the same grating device taken with a multi-mode fiber. (b) Table of $g^{(2)}(0)$ and background values. (c) Plot of background vs. pump. (d) Saturation curve in which blue represents the total count rate from the device; black is the interpolated background; red is the background-subtracted signal (NV fluorescence).

efficiency is modest (a factor of 2.3) and deviates from the predicted value of around 5. This could be attributed to deviation of the dipole position from the field maximum of the cavity, which affects the coupling of emission to surface plasmons. Additionally, the tapering effect mentioned in the previous chapter can further reduce this coupling due to changing of the angle of the scattering point between the diamond/silver interface and the nanopost sidewall.

Overall, the device yield is low, with only about 4 working grating devices (having saturation intensities from 337 to 704 kcps and $g^{(2)} < 0.5$) out of over 100 tested across many experimental attempts. Fig. 4-11 provides a summary of grating device performance (in terms of I_{sat} and τ_{NV}) and comparison to bare and Ag-coated nanoposts.

A limitation to the yield is the material issues with regard to Ag. In this work and

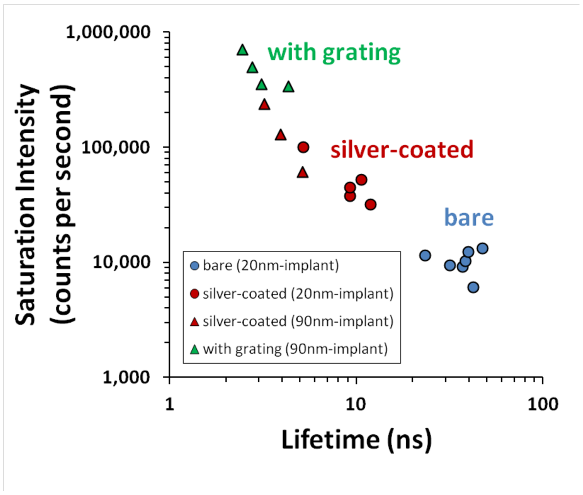

Figure 4-11: Summary for device performance for all plasmonic structures studied.

the previous experiments with Ag-coated nanoposts, it has been difficult to reliably deposit high-quality Ag films. Often, we observed a complete loss of single photon character (no dip in $g^{(2)}$) post-Ag deposition for posts that originally contained single NV centers. This might be due to imperfect adhesion between Ag and the nanostructured diamond surface, leading to formation of undesired plasmon resonances (air pockets) and oxidation of Ag at the device level. While the poor adhesion was ameliorated by either adding a sticking Ti layer or using a conformal deposition method such as sputtering, many fabrication runs were needed before we could obtain a working sample and we have yet to figure out a consistent approach. In general, a working sample can be measured for several weeks in air before oxidation effects become evident. We have capped the devices with a transparent material such as magnesium fluoride (MgF_2) or SiO_2 to slow down the degradation, and recently graphene has been shown to be an effective passivating material for Ag [92]. We have summarized the deposition parameters and some attempts to improve the quality of the films in the Appendix.

Another problem we noticed is the photo-ionization of emitters. While NV centers tend to be very photo-stable in bulk devices, those in diamond-silver structures appeared to be more prone photo-ionization (after which they become dark and cannot be revived) after continuous excitation over a few days of measurements. For this reason, we avoided using very high excitation powers to characterize the devices. Moreover, even though we can re-use the same sample over many fabrication runs, the number of NV-containing nanoposts has decreased over time, even when the structures have remained intact. These observations might be consistent with the ionization of emitters due to contact with the metal, in which the Schottky barrier formed between diamond and the deposited Ag is shallow enough [93,94] for charges to tunnel from diamond into the Ag matrix under photo-excitation. Another possibility is the diffusion of Ag atoms into the diamond substrate. To address these issues, we are currently investigating surface functionalization approaches and the addition of a thin passivating layer between diamond and Ag via atomic layer deposition. Moving forward, better understanding of the chemical and electronic interactions between diamond and Ag at the interface would be critical.

In our study of the grating devices, we did not confirm beaming of the single photon beam via techniques such as fourier plane imaging [91]. This is due to the fact that our objective provides a fairly narrow critical cone (about 36°), while the diamond-air interface acts as an additional filter allowing only an acceptance angle of 25°. This is further compounded by the widening of the beam due to refraction at the interface. All these lead to an overall poor angular contrast in the fourier plane of our optical system, so that it would be difficult to distinguish between the angular profiles of the grating and non-grating cases.

Finally, we optimized our device design and obtained a collection efficiency of up to 64% for a strongly collimated beam (Fig. 4-12). This revised design requires 15 layers of grooves with varying periodicities, and was generated using the optimization module on COMSOL to maximize the power emitted into a narrow angular cone ($\sim$10 degrees) normal to the sample plane in the far-field. An SEM image of a fabricated device (before Ag deposition) is shown in Fig. 4-13.

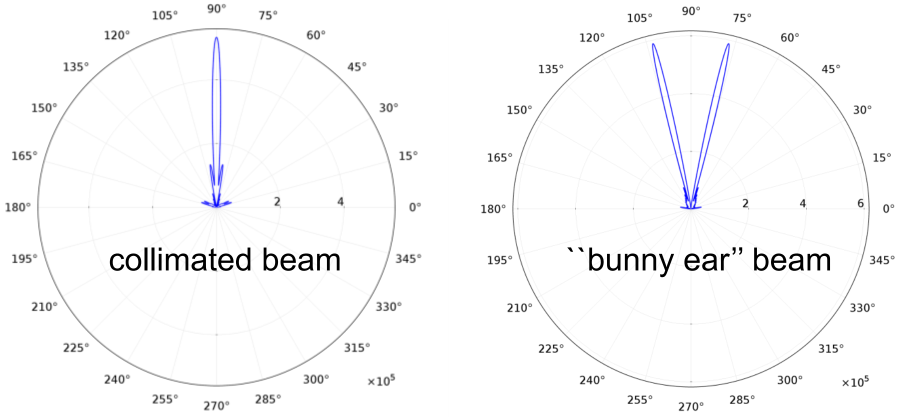

Figure 4-12: Simulated angular emission of optimized designs for a collimated and "bunny ear" shaped beam. The collection efficiencies are 64% and 46%, respectively.

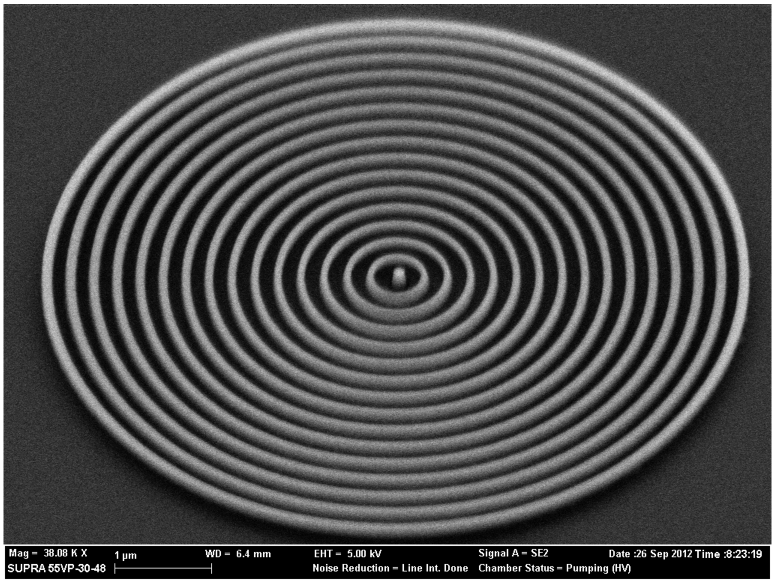

Figure 4-13: SEM image of a diamond nanopost surrounded by glass rings with optimized design parameters. Image taken at a tilted view.

By maximizing the power emitted into a narrow range of angles around a specific polar angle (at 15 degrees away from the axis, for example), we obtained "bunny ear" beam shapes with a collection efficiency of 46% (Fig. 4-12). Such a distinctive angular profile might facilitate the demonstration of beam shaping in fourier plane imaging on our moderate N.A. setup. For practical applications, the general geometry and design approach can be used to generate on-chip optical components such as collimators and beamsplitters that are integrated with single emitters.

Chapter 5

Visible photonics with thin film titanium dioxide (TiO_2)

5.1 Motivation

Optical waveguides and microresonators are ubiquitous components in optical telecommunication systems and provide a compact means for studying cavity quantum electrodynamics [59]. The integration of microresonators into classical and quantum networks relies on materials that support high quality optical components on a chip-scale [95,96]. In the growing field of quantum photonics, quantum emitters [16,97,98] operate primarily in the visible and near-IR wavelengths. While silicon is a well-established and scalable photonics platform, it is only transparent above 1.1 μm. Therefore, the development of a chip-scale, low-cost platform for the visible to near-IR is a critical step towards the realization of quantum communication networks, and can be beneficial to classical applications such as light generation and on-chip sensing. While gallium phosphide [99], silicon nitride [96, 100, 101], silicon dioxide [102], and diamond [2,56], are all promising materials, certain challenges remain, including intrinsic luminescence [100] in the case of nitride, difficulty of generating thin membranes with low optical loss [103] in diamond, poor refractive index contrast with the surrounding medium [102] in silica, and low tolerance for fabrication imperfections due to inherently small characteristic lengths in the visible.

Titanium dioxide (TiO_2) can be added to the family of viable integrated visible photonics platforms. It is a wide-bandgap semiconductor (with a bandgap energy between 3 – 3.5 eV, depending on the crystalline phase [104]) with a moderately high index for the visible wavelengths ($n \approx 2.4$) and a wide transparency window from the near UV to the IR. It is also naturally abundant and is compatible with a host of conventional growth techniques. In addition, TiO_2 has promising non-linear optical properties in both bulk crystals and polycrystalline thin films, with a Kerr nonlinearity of $8 \times 10^{19} \mathrm{m}^2/\mathrm{W}$ and low two-photon absorption above 800 nm [8].

While the optical properties of TiO_2 have been exploited in three-dimensional photonic crystals [105], gratings [106], and micron-sized waveguides [107], sub-micron planar waveguide and resonator structures had yet to be demonstrated. In this chapter, we present a scalable fabrication process for TiO_2 waveguides and microresaontors.

5.2 Optical properties of TiO_2 thin films

TiO_2 thin films were deposited on thermally-grown silicon dioxide using RF sputtering of a Ti target in an O_2/Ar environment [8]. Two particular types of films were investigated: amorphous, deposited at room temperature, and anatase, which required a deposition temperature of 350 °C. The growth conditions [8] were chosen such that the films would be stoichiometric and optical losses would be minimized.

The crystalline structure of the TiO_2 thin films were determined by Raman spectroscopy. Room temperature deposited films had no discernible peaks in the Raman spectra, indicating that they are amorphous, while films deposited at high temperature showed the characteristic peaks for the anatase phase of TiO_2. Meanwhile, optical constants of the deposited thin films were obtained by fitting ellipsometry results to the Sellmeier model. For the amorphous thin film, the material dispersion from the visible to the IR (Fig. 5-1) shows that the refractive index remains in the 2.3–2.4 range within a large wavelength window.

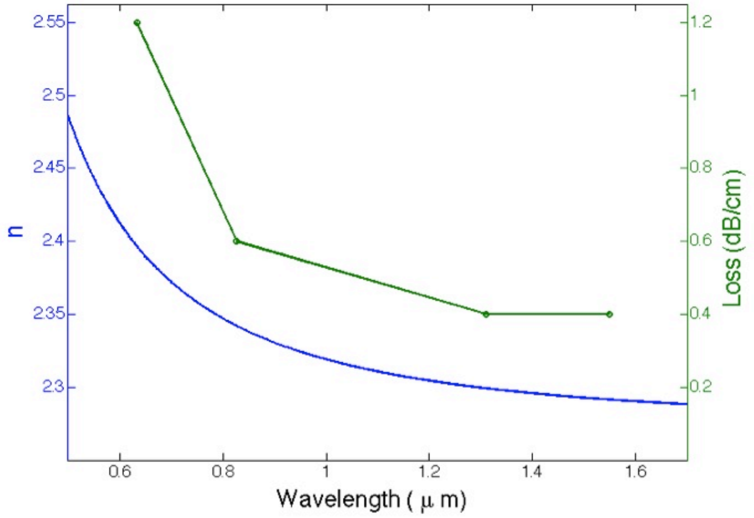

Figure 5-1: Refractive index of amorphous TiO2 film as a function of wavelength. Propagation loss in a 250-nm thick film.

The propagation losses of the films were measured using a variable angle prism coupling system [108], by scanning a fiber along the coupled planar waveguide mode normal to the surface of the film and sending the collected light scattered off the surface into a germanium detector. The data can then be fitted to an exponential curve. The measurements were performed at 633, 826, 1310, and 1550 nm and the loss values for a 250-nm thick amorphous film are shown in Fig. 5-1. The losses vary from 1.2 ± 0.02 dB/cm at 633 nm to 0.04 ± 0.01 dB/cm at 1550 nm. Losses in an anatase film of the same thickness are significantly larger (> 20 dB/cm in the visible to around 4.2 dB/cm in the IR), due to increased roughness in the crystalline film [8].

5.3 Photonic structures in TiO_2

5.3.1 Waveguides for broadband operation

We used electron beam lithography to define our strip waveguides. A 300-nm thick positive electron beam resist (ZEP) was spun on the film and exposed in a 100 keV electron beam lithography system. The sample was then developed in o-xylene. We then deposited a 50-nm-thick layer of chromium metal via e-beam evaporation and subsequently lifted off the remaining resist to leave a Cr etch mask on the TiO_2 film. The mask pattern was transferred into the TiO_2 film using electron cyclotron resonance (ECR) reactive ion etching (RIE) and a CF_4/H_2 gas mixture. The recipe has an etch rate of approximately 60 nm/min and the etch time was timed so that the etch depth was roughly equal to the TiO2 film thickness. We then removed the remaining Cr using Cr-etchant and deposited a 1.6-μm-thick Cytop fluoropolymer top-cladding layer. Finally, we cleaved the chips with a diamond scribe to prepare waveguide facets for launching light into the waveguides. The fabricated waveguides and their facets after cleaving can be seen in Fig. 5-2.

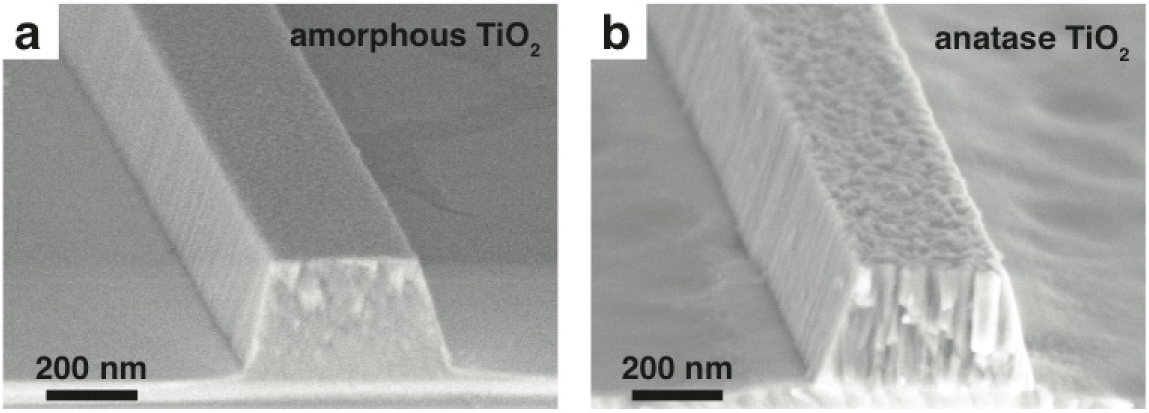

Figure 5-2: SEM images of 0.3-μm-wide (a) amorphous and (b) polycrystalline anatase TiO_2 waveguides fabricated on oxidized silicon wafers.

Light transmission in our TiO_2 waveguides were measured using the top-view camera method [109]. TE-polarized light from a 633-nm HeNe, 780-nm diode or 1550-

nm diode laser source is aligned and focused onto the input facet of the waveguide using an objective lens (633 and 780 nm) or lensed fiber (1550 nm) mounted on a piezoelectric-motor-controlled XYZ stage. The scattered light at 633 nm and 780 nm and 1550 nm was then detected using microscope-mounted CCD and InGaAs cameras, respectively. The camera images for a 200-nm wide and 250-nm tall waveguide are shown in Fig. 5-3a-c, in which we could clearly see light propagation through the waveguide on a mm-scale. By integrating the intensities on camera, we obtained the loss profile as a function of distance (Fig. 5-2d). The fitted propagation loss values are 30 dB/cm, 13 dB/cm, and 4 dB/cm at 633, 780, and 1550 nm, respectively.

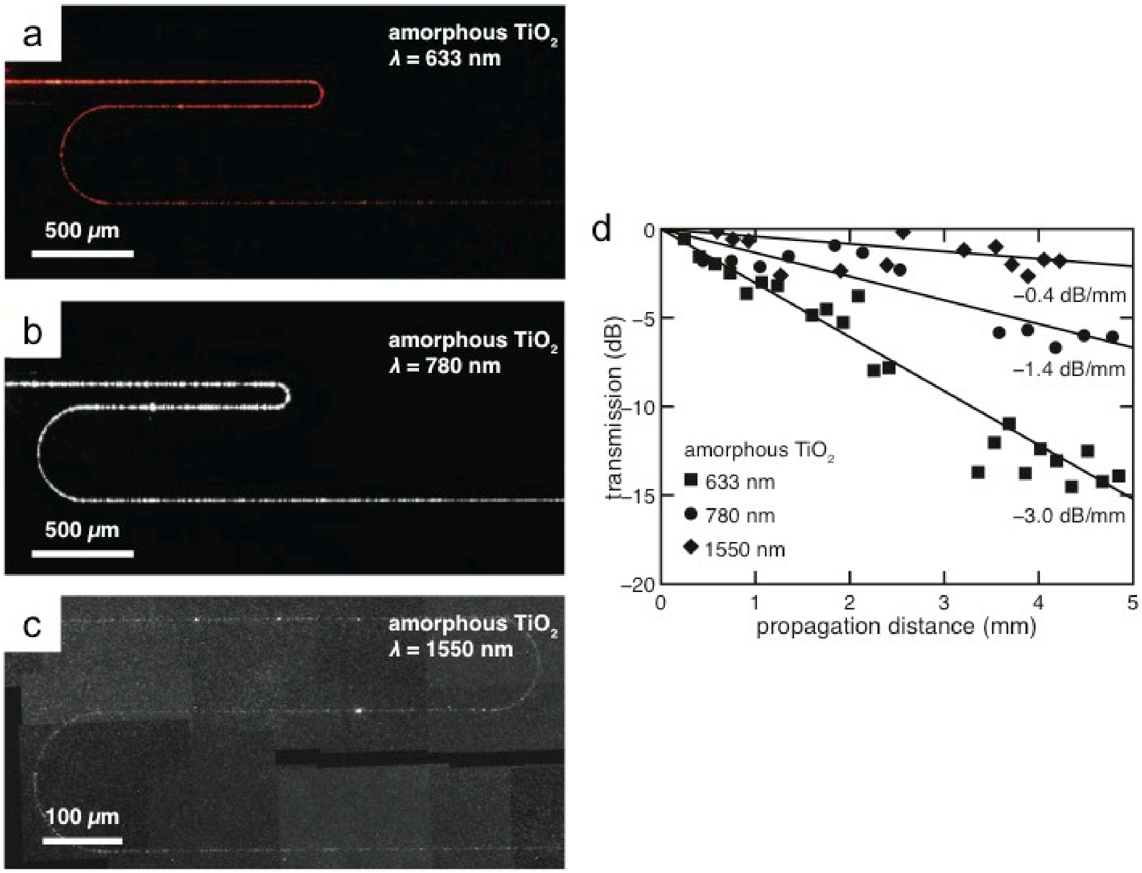

Figure 5-3: (a)-(c) Top-view CMOS (633 nm and 780 nm) and InGaAs (1550 nm) camera images showing light propagation at different wavelengths λ in 0.2-μm wide amorphous TiO$_2$ waveguides. (d) Propagation losses of measured using the top-view camera method. The input light is TE-polarized.

The observed propagation losses in our waveguides are much high than those in the thin films, which could be due to roughness in the sidewalls of the etched structures, scattering from core-cladding interfacial roughness, and e-beam write-field stitching errors. Nonetheless, our method is suitable for fabricating low-loss TiO_2 waveguides over the μm- and mm-range, that can operate over a wide wavelength range from the visible to IR.

5.3.2 Integrated racetrack resonators

We also investigated the fabrication of micro-resonator structures in TiO_2 thin films. For this experiment, amorphous TiO_2 thin films of thickness 170 nm have been deposited on oxidized silicon substrates using RF sputtering of a Ti target in an O_2/Ar environment [8]. Prism coupling experiments [8] indicated that the deposited films have propagation losses as low as 2 dB/cm. These losses suggest that the material-limited Q for optical cavities is around 5×10^5. We used racetrack resonators since they allow for controllable coupling to a waveguide via the coupling length. The fabricated parameters were designed to minimize bending losses (by making bending radii $R = 30\ \mu m$). Additionally, the waveguide-resonator separation g and coupling length L were chosen to ensure efficient transfer of light signal between the cavity and waveguide. To optimize the coupling, we set $g = 130$ nm, waveguide width $w = 250$ nm, height $h = 170$ nm. To better match our experimental conditions, a sidewall slant of 75 degrees is assumed. The coupling length is related to the phase velocity mismatch between the odd and even eigenmodes of the coupled structure and can be calculated by $L_c = \frac{\lambda}{2(n_e - n_o)}$, where ne and no are the effective indices of the even (n_e) and odd (n_o) eigenmodes [3]. For the range of wavelengths between 630 nm and 640 nm, $L = 15 \mu m$ provides near critical coupling (roughly 99% of power transfer) for transverse electric (TE) polarized light.

We realized the designed structures using the aforementioned top-down fabrication techniques. To provide better coupling on- and off-chip, polymer pads (SU-8 2002,

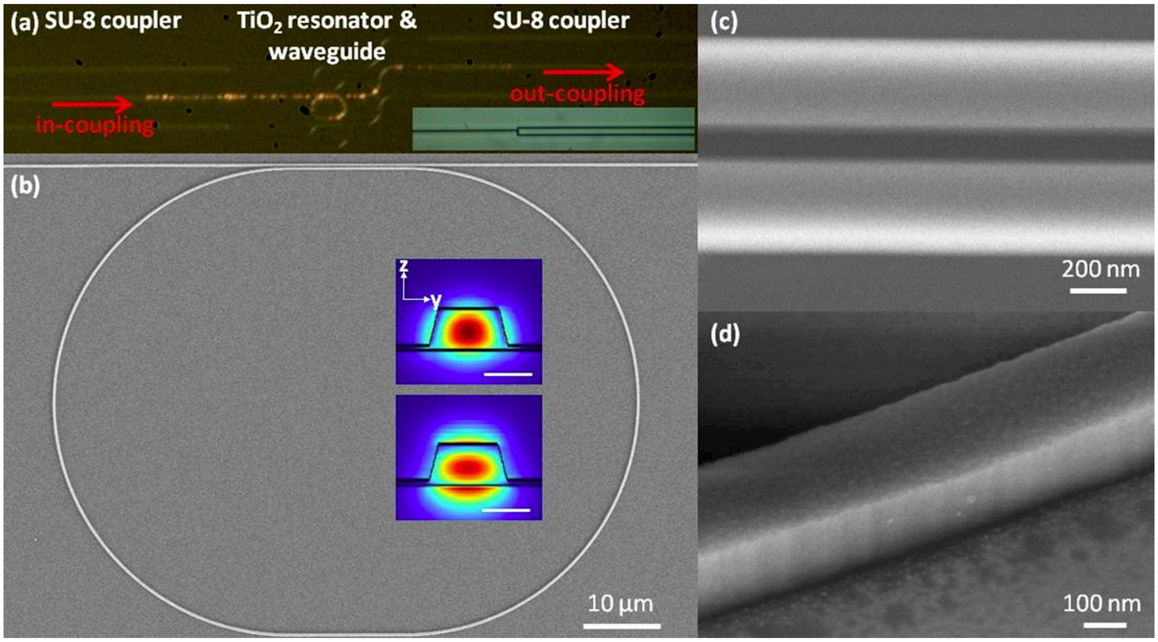

Figure 5-4: (a) Optical image of a set of TiO_2 waveguide-racetrack devices integrated with polymer pads. Inset: overlapping region between the TiO_2 waveguide and polymer pad. SEM images of (b) a TiO_2 waveguide-resonator, (c) its coupling region, and (d) etch profile taken at a 45 degree tilt. Insets: cross sections of the fabricated waveguide/resonator with simulated electric field profiles of the TE (top) and TM (bottom) modes. Propagation is in the x direction. Scalebar = 200 nm.

with cross-sections 3 μm × 3 μm) were written using a second-step electron beam lithography [110]. These pads overlap with the ends of the TiO_2 waveguides and extend to the edges of the chip (Fig. 5-4a). The edges of the polymer waveguides were then cleaved to facilitate in- and out-coupling of light. The input and output facets are offset from one another to avoid direct scattering of un-coupled light into the collection fiber. The devices have surfaces with a roughness of around 10 nm and gaps of approximately 130 nm in the coupling regions (Fig. 5-4b-d).

We simulated the mode profiles of the fabricated devices (insets of Fig. 5-4b) using the finite element method (FEM). From Fig. 5-4, the waveguides have an etch depth of 150 nm and a width of 250 nm on their top facets. These dimensions support one fundamental mode in each of the TE and transverse-magnetic (TM) polarizations with respective effective indices of 1.80 and 1.61 at a wavelength of 630 nm. The pedestal layer, which resulted from non-uniformity in our etching process, is roughly 20 nm-thick and can be beneficial to coupling in waveguide-resonator systems [96]. In our structure, this layer improves coupling into the TM-polarized modes, so that the simulated coupling efficiencies are around 90% for both TE- and TM-polarized light (Fig. 5-5).

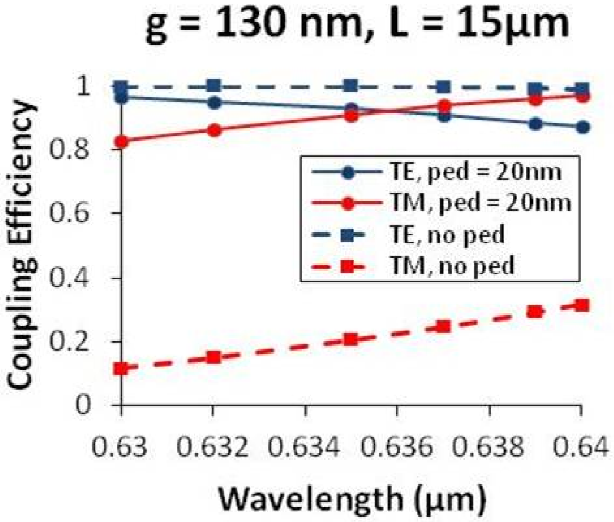

Figure 5-5: Calculated coupling efficiencies of the TE- and TM-polarized modes in the waveguide-resonator system with and without a 20-nm pedestal layer. Here, the efficiencies are inferred from the transmission factor $T = \sin^2(\frac{\pi L(n_e - n_o)}{\lambda})$ [3], where n_e and n_o are obtained using FEM.

The resonators were characterized by transmission measurements using a tunable red laser with a scanning range of 634.4 – 639.6 nm. The output of the laser was coupled to a single mode, tapered lensed fiber that was rotated such that the input signal into the sample was polarized along either the TE or TM direction. Light with a spot size of 0.8 μm in diameter was focused onto the facet of the polymer pad by the tapered lensed fiber and transmitted into the waveguide-resonator device. The output was coupled through a polymer pad on the opposite end of the chip and collected by another tapered lensed fiber that was connected to a high speed silicon detector. For this experiment, the coupling loss from the fiber to the TiO_2 waveguide is roughly 14.5 dB at each end. This loss can be reduced by polishing the facets and optimizing the geometry of the TiO_2 waveguide to reduce light reflections that arise from the refractive index mismatch.

The resonator transmission spectra are shown in Fig. 5-6. All spectra shown here have not been normalized. The transmission spectra have periodically-spaced dips corresponding to whispering-gallery modes (WGM) with either the TE (Fig. 5-6a) or TM (Fig. 5-6b) polarization. The small dips observed in Fig. 5-6b are due to imperfect polarization filtering of TE-polarized signals. The loaded quality factors ($Q_{loaded} = \frac{\lambda}{\Delta\lambda}$, where λ is the cavity resonance wavelength and $\Delta\lambda$ is the linewidth of the the resonance) were extracted by fitting the transmission dips to the Fano model [111]. The model is necessary due to interference between the transmitted signals and partially reflecting elements in the waveguides, leading to asymmetries in the cavity lineshapes [111]. The fits yielded linewidths as narrow as 0.028 nm and 0.11 nm for the TE and TM polarizations (respectively) near $\lambda = 635$ nm, corresponding to respective Q values of 2.2×10^4 and 5.6×10^3. The observed transmission drops are as large as 96%, indicating that the resonators are nearly critically coupled.

The transmission properties of a waveguide-coupled racetrack resonator have been well-described elsewhere [3,112]with the resonance condition given by $\phi_c + \phi_r = 2m\pi$, where ϕ_c and ϕ_r respectively represent the phase changes in the coupler and the rest of the resonator, and m is the integer mode index. Using $\phi_i = \frac{2\pi}{\lambda_m} n_i(\lambda_m) d_i$, in which $n_i(\lambda_m)$ is the wavelength-dependent index of the guided mode and d_i is the distance, the resonance condition becomes

$$n_r(\lambda_m)(2\pi R + L) + n_c(\lambda_m)L = \quad m\lambda_m \tag{5.1}$$

$$n(\lambda_m)(2\pi R + 2L) = \quad m\lambda_m \tag{5.2}$$

where we have assumed that $n \approx n_r \approx n_c$. Solutions for consecutive modes m and

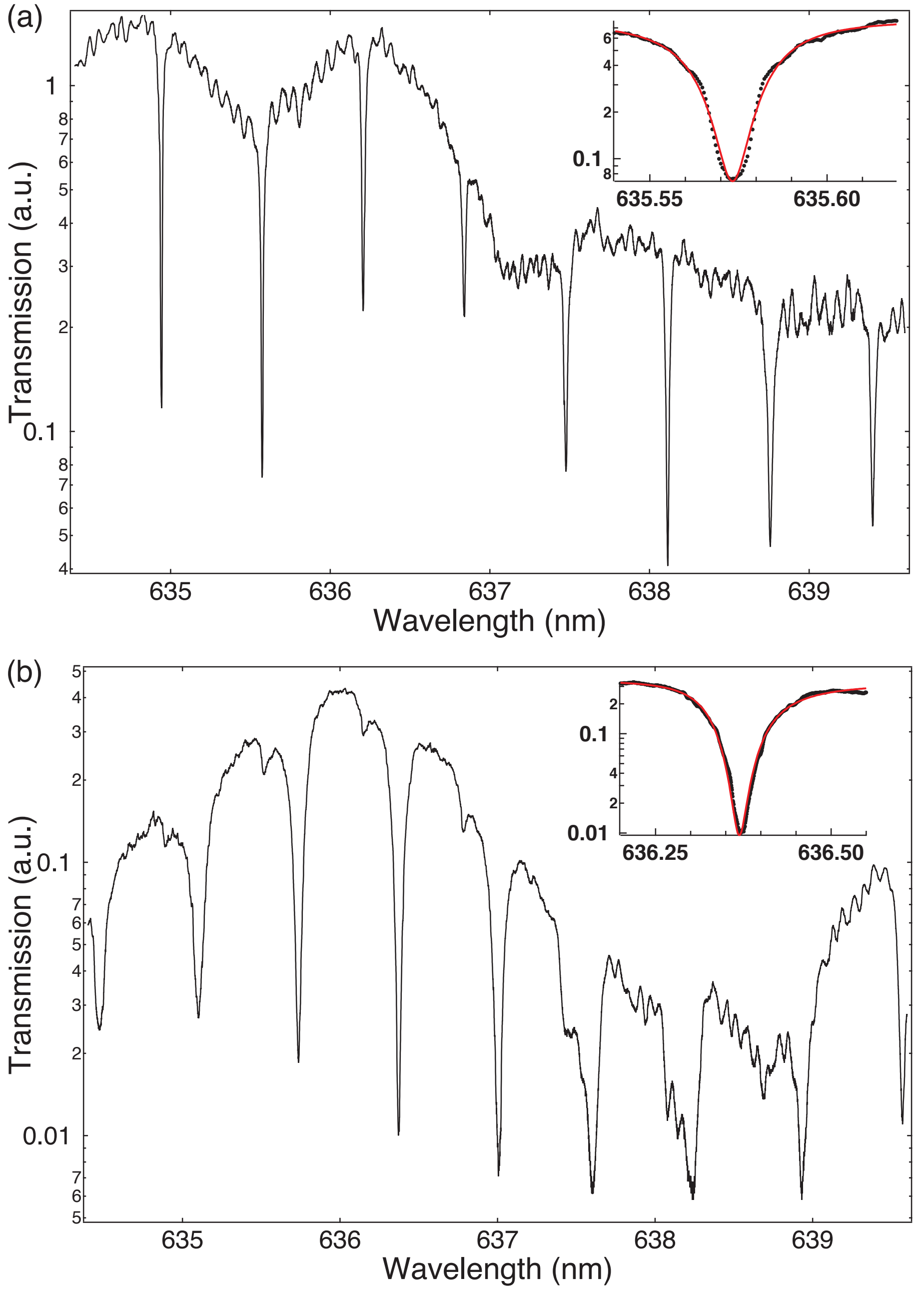

Figure 5-6: (a) TE-polarized transmission as a function of wavelength for a racetrack resonator with R = 30 μm and L = 15 μm. Inset: cavity mode at 635.57 nm, along with a fit to the Fano model (red). The fitted linewidth is 0.028 nm, corresponding to a Q of 22400. (b) TM-polarized transmission as a function of wavelength for the same resonator. Inset: cavity mode at 636.36 nm, with a fitted linewidth of 0.11nm and corresponding Q of 5629.

$m + 1$ are then related by [113]

$$\begin{aligned}
\frac{n(\lambda_{m+1})}{\lambda_{m+1}} - \frac{n(\lambda_m)}{\lambda_m} &= \frac{1}{2\pi R + 2L} \\
\lambda_m(n_0 + (\lambda_m - \lambda)\frac{\mathrm{d}n}{\mathrm{d}\lambda} + ...) - \lambda_{m+1}(n_0 + (\lambda_{m+1} - \lambda)\frac{\mathrm{d}n}{\mathrm{d}\lambda} + ...) &= \frac{\lambda_m \lambda_{m+1}}{2\pi R + 2L} \\
(\lambda_m - \lambda_{m+1})(n_0 - \frac{\mathrm{d}n}{\mathrm{d}\lambda}) &\approx \frac{\lambda_m^2}{2\pi R + 2L}
\end{aligned}$$

The quantity $n - \lambda\frac{\mathrm{d}n}{\mathrm{d}\lambda}$ is denoted as the group index n_g and takes into account dispersion in the system [113].

We used the Sellmeier coefficients obtained from spectroscopic ellipsometry measurements on our TiO_2 films to determine the wavelength-dependent index (n_{mat}). The first order effective index (n_{eff}) and group index (n_g) were then computed [113] and are shown in Fig. 5-7. In the visible wavelengths, n_g in TiO_2 waveguides can be significantly larger than n_{eff} (difference of approximately 57% for the TE mode and 70% for the TM mode). The greater difference observed in the TM polarization is due to larger waveguide dispersion, which can be estimated by calculation of the group index $n_{g,w}$ of the given waveguide without considering the wavelength-dependence in n_{mat}. The large discrepancy between n_g and n_{eff} can thus be attributed to both waveguide and material dispersions, although the contribution from the latter decreases with increasing wavelengths, as indicated by the diminishing difference between the group index with and without material dispersion (n_g and $n_{g,w}$, respectively). Dispersion must therefore be considered when designing optical components in TiO_2 and can be exploited to generate small FSRs without significantly increasing the device footprint. The calculated n_g values are in good agreement with the experimentally obtained number, in which an FSR of 0.64 nm (Fig. 5-6a) corresponds to a group index of 2.92 in the 635 nm to 640 nm range in the TE polarization.

Meanwhile, the coupling between the feeding waveguide and resonator depends on both the coupling length and phase velocity mismatch and so the effective indices

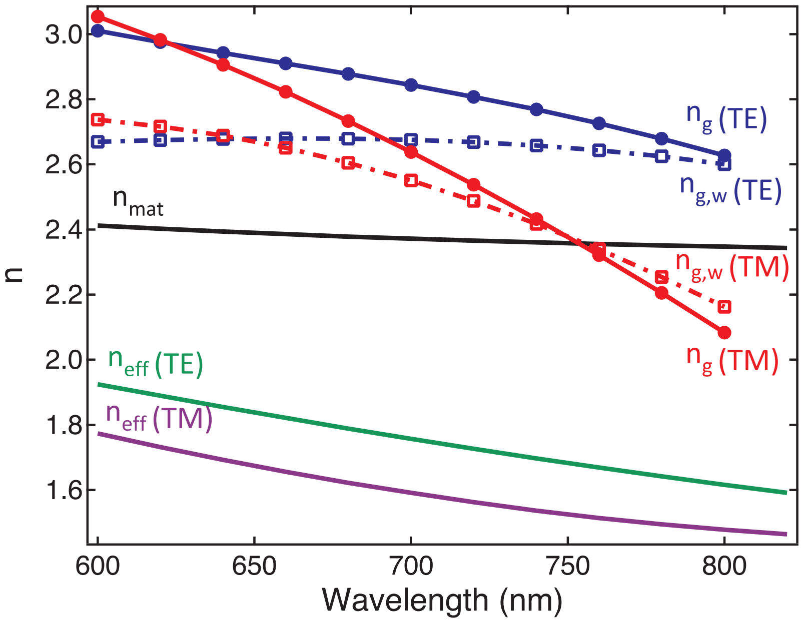

Figure 5-7: Calculated effective (n_{eff}) and group (n_g) indices as a function of wavelength for the TE and TM-polarized waveguide modes. Contributions to the difference between n_{eff} and n_g include dispersions in the material (n_{mat}) and waveguide, which can be inferred by calculating n_g using a fixed n_{mat} of 2.4 ($n_{g,w}$).

of the odd (n_o) and even (n_e) eigenmodes of the coupled structure need to be considered [3]. From [3], the transmission factor (T) is related to the index difference between the eigenmodes by

$$T = \sin^2(\frac{\pi L(n_e - n_o)}{\lambda}). \tag{5.3}$$

Using measured data across several resonator devices with different coupling lengths ($L = 10, 15\ \mu m$) and identical separation ($g = 100$nm), we estimate ($n_e - n_0$) to be 0.02 ± 0.004 for the TE mode and $0.017 \pm .0003$ for the TM mode. Since g in the ~100 nm range is challenging to control precisely in experiment, the extrapolated parameter provides a more reliable means to control the power transfer between the TiO$_2$ waveguide and resonator via the coupling length.

Finally, the propagation loss in a critically-coupled resonator can be estimated using $\alpha_r = \frac{\pi n_g}{\lambda Q_{loaded}}$ [114]. Based on a TE-polarized mode with a Q of 22400 and transmission drop of 92% (inset of Fig. 5-6a), the corresponding propagation loss is 28 dB/cm. This value is consistent with results we obtained from bare TiO_2 waveguides [8]. The deviation (by more than a factor of 10) from the planar loss value is most likely due to scattering losses from surface roughness introduced by the fabrication process, which might be reduced by using a top-cladding material. Another possibility is that the films have become lossier due to the fabrication steps we used, including heating up the film during resist baking, and subjecting it to a metal etchant. To elucidate the origin of the increase in loss, we would need to perform the same fabrication treatments (i.e. heat, wet etchant) to a bare, unstructured film and measure its planar loss to know the true material loss.

We have demonstrated planar resonators in TiO_2 thin films for visible light operation with efficient coupling to waveguides for delivering light on- and off-chip. The methods and devices shown here could help advance the TiO_2 material platform towards integration with active emitters for novel and integrated classical and nonclassical light sources and on-chip sensing.

5.4 Material challenges

Despite the excellent optical properties of TiO_2, several material challenges appear to hinder the performance and feasibility of certain optical devices. The optical loss of TiO_2 is very sensitive to growth conditions and require low temperature processing techniques to maintain film quality. For instance, the bake steps we used for the electron beam writing could have modified the film structure [115], contributing to the large difference between the losses in the planar waveguide and the channel waveguide and resonator. We also observed an increase in the optical loss over time for films in storage, as well as degradation in the Q of the micro-resonators if they have been exposed to air for days. A way to circumvent the degradation in material quality might be to cap the film and devices with a low index material. Moreover, TiO_2 thin films do not seem to be compatible with standard wet processing methods for releasing the device layer from a sacrificial substrate such as silicon or silicon dioxide (Appendix), which might pose a limitation on the fabrication of free-standing structures.

5.5 Interaction of TiO_2 with quantum emitters

5.5.1 Dielectric TiO_2 slot waveguides

Despite certain material limitations, the ability to make nano-scale devices in TiO_2 has opened up possibilities of using this material to probe and enhance light-matter interaction with quantum emitters in the visible, including fluorescent dye molecules, colloidal quantum dots, and color centers in diamond nanocrystals. In particular, we have investigated the use of slot waveguides as a broadband and low loss platform [116] to investigate quantum systems in nanocrystals. Dielectric slot waveguides consist of a sub-wavelength slot between two waveguides made of a material with a much higher dielectric constant, so that there is a discontinuity in the electric field distribution at the boundaries of the slot region, resulting in a high concentration of optical energy in the slot region [117]. The high field intensity can be used to enhance the interaction of an emitter inside the slot with the light field. Given the relative high index of TiO_2 among comparatively visibly transparent materials, it is a good candidate for implementing slot waveguides that operate in the visible wavelengths.

We have simulated the electric field profile and Purcell enhancement of TiO_2 dielectric slot waveguides with different dimensions and slot widths, assuming a TE-polarized dipole [116]). The results are shown in Fig. 5-8. The enhancement increases with increasing wavelength, and air slot widths as small as ~ 20 nm can provide an enhancement of around 18 at a wavelength of 620 nm.

In reality, it is difficult to fabricate small slot widths significantly below < 100 nm

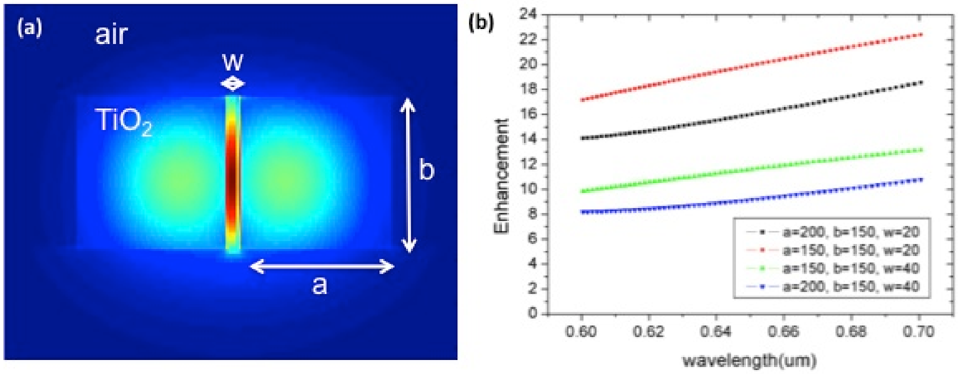

Figure 5-8: (a) Simulated energy distribution of a TiO$_2$ slot waveguide in air. (b) Simulated Purcell enhancement as a function of wavelength for different slot waveguide dimensions.

using our top-down nano-fabrication procedure. This is mostly due to the fact that during reactive ion etching, the etch gases cannot easily penetrate through the small exposed region, leading to a large disparity in the etch rates of the slot and open regions. This can be seen in Fig. 5-9, an SEM image of the etch profile of a TiO$_2$ slot waveguide, in which only a small dent in the slot region is observed while the rest of the waveguide is etched through. A deeper dent would require a much longer etch time, although at some point, the extent of the slot would be limited by the tapered profile of the etching.

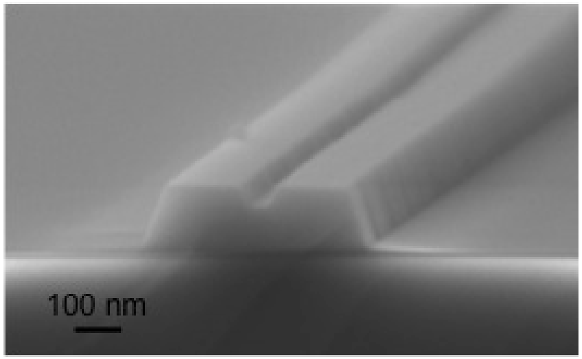

Figure 5-9: SEM image of a cleaved facet of a TiO$_2$ slot waveguide after reactive ion etching and mask removal.

To better define the slot region, we implemented an approach reported in [118] and combined top-down fabrication with conformal deposition of TiO$_2$ material using atomic layer deposition (ALD) post-etching. We defined waveguides with larger > 100 nm gaps, so that the slot region could be etched through and deposited TiO_2 material via ALD to close the gap. This results in pedestal slot waveguides (Fig. 5-10) with very small gaps at the bottom of the slot, which still supports strong enhancements of electric field.

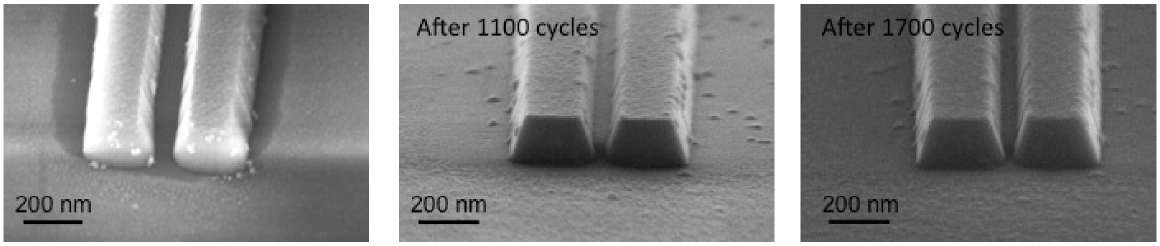

Figure 5-10: SEM images of TiO_2 slot waveguides fabricated by ALD deposition after reactive ion etching of wide slots. Left image: slot waveguide after reactive ion etching and mask removal. Right images: slot waveguide after a certain number of ALD cycles.

We worked on the integration of CdSe/ZnS quantum dots into the air slots of the fabricated waveguides. The dots are incorporated into the waveguides using a dip-coating procedure [119], in which the sample chip was submerged in a dot-containing solution and slowly extracted from the solution at a constant speed so that nanoparticles inside the solution are subjected to interfacial capillary force that places them onto defined patterns on the substrate. We have observed evidence of coupling of quantum dots and the slot waveguide structures, by SEM imaging and demonstration of guiding of red emission from the embedded dots to the ends of the waveguides (Fig. 5-11).

While dip-coating method works in placing dots inside the slots, there are also dots deposited on the surface of the waveguides, which make it difficult to identify the contribution to the fluorescence during optical characterization. Therefore, this technique would need to be fine-tuned before it can be used to study emitters on a single-particle level. Furthermore, the QD-TiO_2 system presents interesting charge dynamics which we will discuss next.

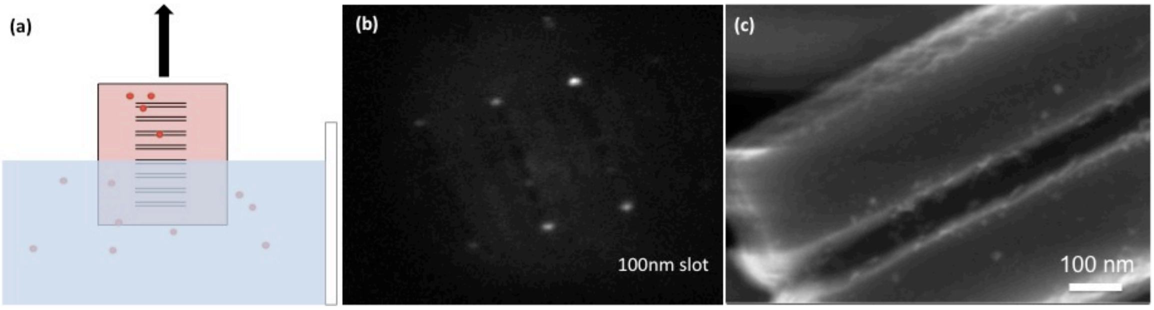

Figure 5-11: (a) Dip-coating procedure. (b) Wide field image of filtered photoluminescence from green excitation of the sample, showing emission from embedded QDs within the waveguides, as well as out-coupling of fluorescence at the ends of the waveguides. (c) SEM image of dots deposited throughout the waveguide, including inside the slot.

5.5.2 Observation and suppression of charge transfer between quantum dots and TiO_2

In this section, we study the interaction between colloidal quantum dots and TiO_2 thin films. Quantum dot-sensitized TiO_2 have become a promising photovoltaic material [120], and TiO_2 in particular is known to be strong electron-acceptor in solar cells [121]. However, for potential applications of using TiO_2 optical structures to modify the emission of quantum emitters, the ionization of the emitter can lead to quenching in the emission and is thus an undesirable effect. Therefore, it is of interest to examine the charge transfer interaction between quantum dots and TiO_2 on a single emitter level and implement an approach to suppress electron transfer.

In a semiconductor nanocrystal with a radius much smaller than the bulk exciton Bohr radius, quantum confinement on the electron and hole in all three dimensions leads to an effective band gap [122]. This band gap increases with decreasing nanocrystal size. While quantum dots are single photon sources with high quantum efficiency, they exhibit fluorescence intermittence, or blinking, in which the fluorescence intensity of the individual dots alternate between an on- and off-state. Blinking is generally attributed to the loss of an electron to trap states or other energy states. Therefore, blinking behavior is closely tied to charge dynamics of the nanocrystal.

Core-shell CdSe/ZnS quantum dots constitute one type of these semiconductor nanocrystals [122]. They can be assembled by colloidal synthesis and generally operate in the visible wavelengths. As the size of the CdSe/ZnS quantum dot decreases, the bandgap widens, but the shift is significantly greater for the conduction band than the valence band. For dots that are deposited on a TiO_2 substrate, the conduction band the dot becomes above that of TiO_2 after some critical radius, thus providing a pathway for electron injection into the host matrix. This generally occurs when the dots are around 10 nm in diameter, with peak emission wavelengths of ~ 620 nm.

We dropcast quantum dots (with peak emission wavelength around 620 nm) on glass and TiO_2 substrates and monitored fluorescence time traces of single dots on a confocal microscope, by exciting the dots with a CW laser at 532 nm at low ($\sim 10\mu$W) power. A representative set of traces is shown in Fig. 5-12. The results are similar to those reported in [121], in which the degree of blinking appears to be more severe on TiO_2 substrate. The time traces exhibit self-similarity over different time scales, but in each case, the off-state occurs much more often on TiO_2 substrates. This can be better illustrated by integrating the fluorescence intensity collected over small time bins (10 ms) and generating a histogram for photon counts/time bin. The histograms (Fig. 5-12) show two peaks, which represent the occurrences for the off-states (left peak) and on-states (right peak). While for the dot on SiO_2 the relative amplitudes of the two peaks are comparable, on TiO_2 the off-state peak is much larger than that for the on-state. This can be attributed to electron transfer from the dot to the TiO_2 substrate.

Electron transfer is a tunneling process and thus its rate k_{ET} has an exponential dependence on distance d: $k_{ET} \propto e^{-\beta d}$, where β is the coefficient set by the potential of tunneling barrier. One way to suppress electron transfer is to increase the distance between the dot and TiO_2, which can be done by coating the dots with SiO_2 [123]. SiO_2-coated dots (with a diameter of ~ 20 nm in total, so that the coating thickness is around 5 nm) were deposited on SiO_2 and TiO_2 substrates and the fluorescence time traces for single dots were monitored as before (Fig. 5-13). As can be seen in the representative set of traces, the blinking behavior become more comparable between the two substrates and the histograms clearly indicate that the on-state has a higher probability of occurrence.

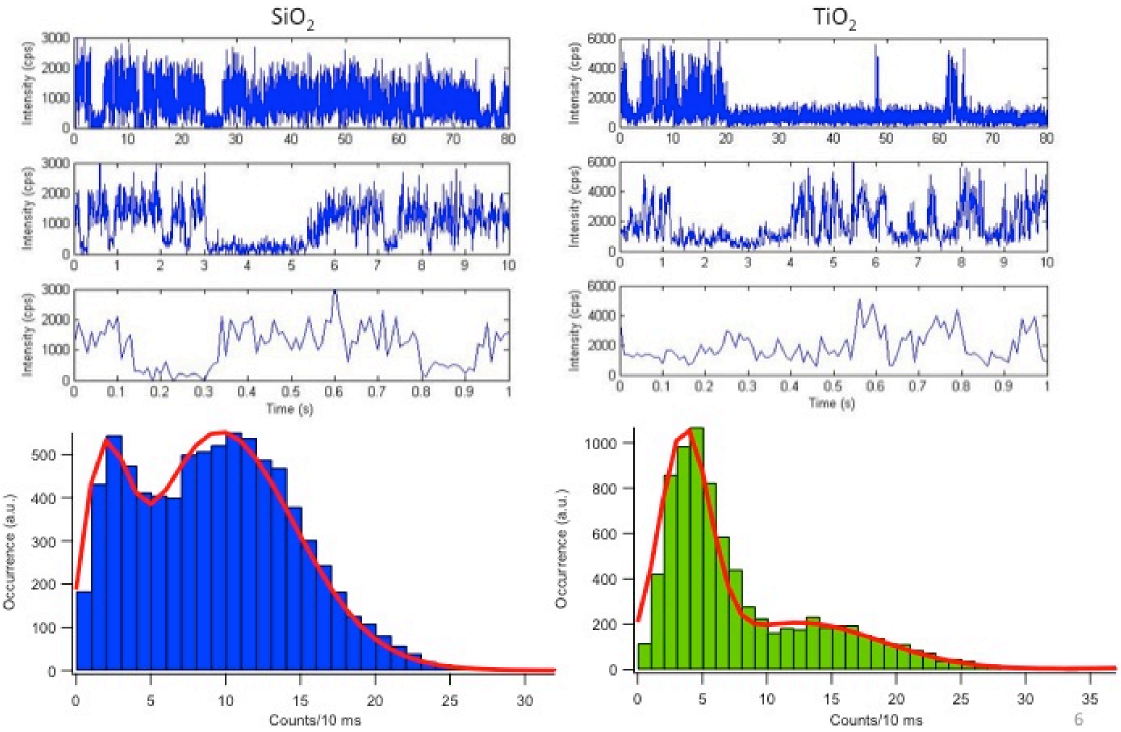

Figure 5-12: Fluorescence intensity time traces of CdSe/ZnS quantum dots on SiO_2 and TiO_2 substrates and the corresponding histograms for the fluorescence intensities collected over time bins of 10 ms.

Blinking behavior and the emitter lifetime are correlated, in which the lifetime of the emitter during an off-state is shorter due to the non-radiative decay pathway [121]. We measured the fluorescence lifetimes of the quantum dots on the two substrates, using pulsed excitation at around 530nm with a 10.9 MHz repetition rate. The fluorescence decay ($f(t)$) could be fitted to a tri-exponential model, which yielded time constants corresponding to background (bg) and the bright (on) and dark (off)

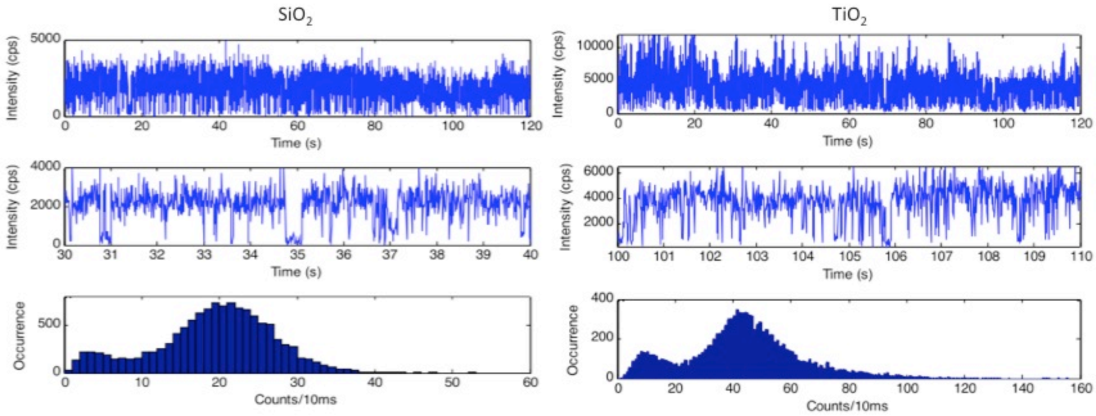

Figure 5-13: Fluorescence intensity time traces of SiO$_2$-coated CdSe/ZnS quantum dots on SiO$_2$ and TiO$_2$ substrates and the corresponding histograms for the fluorescence intensities collected over time bins of 10 ms.

states:

$$f(t) = f_0 + C_{bg}e^{-\frac{t}{\tau_{bg}}} + C_{bright}e^{-\frac{t}{\tau_{bright}}} + C_{dark}e^{-\frac{t}{\tau_{dark}}}. \tag{5.4}$$

We can use the parameters F_{bright} and F_{dark} to quantify the contribution to the fluorescence from radiative and non-radiative pathways, using:

$$F_{bright} = C_{bright}/(C_{bright} + C_{dark}) \tag{5.5}$$

and

$$F_{dark} = C_{dark}/(C_{bright} + C_{dark}). \tag{5.6}$$

A representative decay curve and the averaged lifetime values collected for > 5 dots in each scenario are given in Fig. 5-14. For bare dots, the TiO$_2$ substrate leads to a $\sim$ 30% shorter lifetimes due to the higher dielectric environment and higher occurrence of Auger recombination. Non-radiative channels clearly dominate the fluorescence decay for dots on TiO$_2$, as shown by the large F_{dark}. For SiO$_2$ coated dots, the on-state lifetimes are prolonged and dots on TiO$_2$ still have shorter lifetimes than on SiO$_2$ due to being in a higher dielectric environment, but the dark state contribution to the fluorescence is reduced (from a F_{dark} of 89% to 33%). SiO_2 passivation seem to have increased F_{bright} on both SiO_2 and TiO_2 substrates, but the extent of improvement is greater in the latter, suggesting that the non-radiative pathway due to tunneling into the TiO_2 matrix has been suppressed.

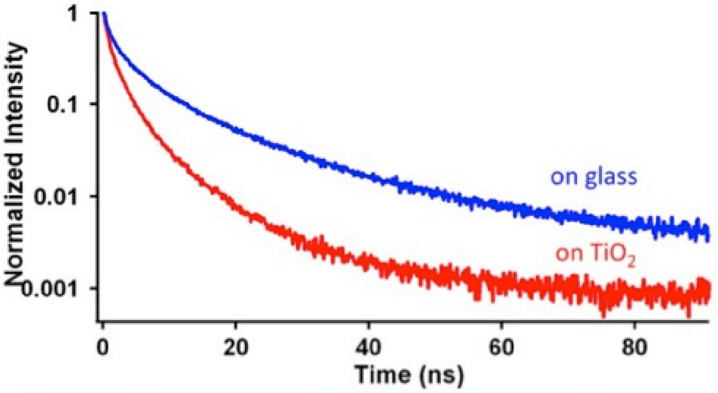

	τ_{bright} (ns)	τ_{dark} (ns)	F_{bright}	F_{dark}
glass	17.0±3.7	4.94±0.9	32%	68%
TiO_2	13.2±1.5	3.79±0.4	11%	89%

silica-dad	τ_{bright} (ns)	τ_{dark} (ns)	F_{bright}	F_{dark}
glass	29.9±3.2	8.09±2.2	82%	18%
TiO_2	18.7±2.2	4.44±0.9	67%	33%

Figure 5-14: Fluorescence decay traces for dots deposited on SiO_2 and TiO_2 substrates. Table of the average (± standard deviation) of the fitted lifetimes for > 5 dots tested in each case.

We have therefore demonstrated an approach to mitigate charge transfer from colloidal quantum dots to TiO_2 host matrix, which can be used for the integration of quantum dot material into TiO_2 optical devices to enhance emitter emission.

Chapter 6

Conclusion

This thesis has described the development of various photonic and plasmonic elements at visible wavelengths for integration with single photon sources. Here, we summarize the major results and discuss the outstanding challenges and future outlook of the various platforms.

6.1 Diamond photonics with NV centers

The diamond photonic devices discussed are aimed at either improving the photon collection and production efficiency. The diamond nanowire geometry provides an order-of-magnitude improvement in both pump and single photon collection efficiencies for single NV centers in comparison to bulk, with count rates $> 3 \times 10^5$ cps. Single NV-containing nanowires can be fabricated by top-down nanofabrication on both nitrogen-rich Ib diamond and combined with ion implantation techniques on ultrapure electronic grade IIa diamond. The top-down approach has provided very high yield of working devices per fabrication run. We have also shown that the device is compatible with low N.A. and nonconfocal systems, owing to the fact that the nanowire emits into a small angular cone, so the device can be potentially integrated directly with a fiber without the need of bulky optics. The nanowire geometry has already found an application in the realization of a sensitive scanning near-field and magnetic field sensor [31].

To modify the spontaneous emission rate of the NV center, the emitter can be made to interact with a cavity under the weak coupling regime. Due to the small fraction ($\sim 5\%$) of emission into the ZPL, for applications that require a large number of photons at the ZPL, a narrowband cavity such as a ring resonator or photonic crystal cavity would be suitable. Despite material and fabrication challenges, these devices can be realized with high quality in single crystal diamond that has been thinned down to optical thickness using reactive ion etching, suggesting the feasibility of this approach towards developing chip-scale diamond quantum photonic networks. Diamond planar resonators are also promising for reaching the strong coupling limit, although an ultra-high Q is likely necessary due to the low branching ratio into the ZPL.

We have designed and implemented diamond-silver apertures for enhancing the spontaneous emission of single NV centers. This platform is intended to provide a broadband alternative to narrowband cavities with higher tolerance for wavelength mismatch between the cavity and NV emission, so that no tuning mechanism is necessary. Additionally, the devices were compatible with previously established top-down nano fabrication and ion implantation techniques. Despite the ohmic losses in the metal leading to a low Q, the structure has ultra-small mode volumes which could result in a large Purcell factor. In experiment, we observed up to a six-fold decrease in the emission lifetime of NV centers in plasmonic apertures, with lifetimes as short as 2.4 ns. We have shown that shallow-implanted NV centers in diamond nanoposts provide a good system for controlling the NV center spontaneous emission rates, exhibiting a range of regimes from quenched emission with prolonged lifetimes in the bare case, to fast decay rates when interacting with the cavity after coating with silver. We further modified the geometry to coherently scatter surface plasmons and increased the collection efficiency of the system by over a factor of 2. The highest flux device has a count rate of around 7×10^5 cps and over 1 Mcps when collected with a multi-mode fiber. The challenge in this platform lies in material issues with silver, outlined at the end of Chapter 4, which leads to a low yield of working devices. While the devices demonstrated so far enhance mostly the phonon sideband of the NV center, for enhance of the ZPL, smaller apertures may be used.

In addition to a high photon flux, single photon emission from the presented devices can have a very low multi-photon probability, satisfying the main requirements of quantum cryptography. Other potential applications include providing improved and faster optical readout for NV center-based nanoscale magnetometry and quantum information schemes involving spin or photonic quits. In these cases, a long spin coherence time is needed, which remains to be measured in experiment.

Despite the large photon count rates ($10^5 - 10^6$ cps) and the ability to make multiple devices in parallel, for entanglement generation between distant NV centers, identical photons are needed, so the emission at ZPL needs to be stable and sufficiently narrow. Meanwhile, the NV centers used in our devices have been implanted and the emitters are in close proximity to the diamond surface, suggesting that they might be more susceptible to surface charge effects that can contribute to spectral diffusion at low temperature. Indeed, low temperature measurements need to be performed to measure the linewidth of the ZPL in our nano-structured devices. Towards this end, we have begun performing measurements of diamond-silver apertures below 5 K to investigate any possible changes in the plasmonic behavior at low temperature as well as observe the ZPL (Fig. 6-1). As expected, the ZPL of the devices significantly narrowed and became a lot more prominent. By comparing the lifetimes of the devices at room and cryogenic temperatures, we found that the spontaneous emission enhancements were mostly unchanged, indicating that the optical losses in the silver were not affected by the temperature change. Infrastructure for measuring

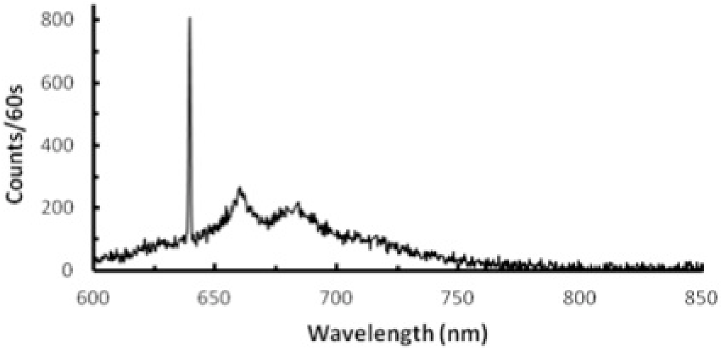

Figure 6-1: Photoluminescence spectrum of a silver-capped nanopost containing a single NV at 4.6 K.

the linewidth of the ZPL via resonant excitation techniques is currently being set up.

An exciting direction for diamond photonics might be the downconversion of single photons from the visible to the infrared, by using either optical cavities or plasmonic grating structures to enhance the optical nonlinearities in diamond. This would allow for long distance transmission of the signal via optical fibers. Finally, while the presented work have focused on the NV center, the structures can scaled to interact with other promising color centers closer to the NIR region.

6.2 TiO_2 photonics

We have presented a top-down fabrication approach to generate chip-scale waveguides and resonators in TiO_2 thin films. In particular, the fabricated waveguides can operate from the visible to the IR with moderately low propagation losses (from 30 dB/cm in the visible to 4 dB/cm in the IR). We also demonstrated racetrack resonators critically-coupled a waveguide with Q as high as $\sim$ 22000 in the visible wavelengths. A promising structure to probe and manipulate light-matter interactions with an emitter is the dielectric slot waveguide, which we fabricated using a combination of top-down and bottom-up fabrication methods. While we also demonstrated integration of colloidal quantum dots to slot waveguides, optical performances of these devices have not been evaluated. Finally, we studied the charge transfer process between colloidal quantum dots and the host TiO_2 thin film on a single emitter level, which has been used to generate photocurrents in photovoltaic devices but is deleterious to certain photonic applications that require enhanced light generation from the quantum dot-TiO_2 material. We suppressed the charge transfer by adding a silica coating to the quantum dots, so that quantum dot emission is no longer quenched on TiO_2 substrates.

TiO_2 is currently being investigated as a material for nonlinear optics. In particular, spectral broadening in the IR and NIR has been observed in anatase waveguides [124]. As a broadband photonics platform for classical and quantum communications, further improvements in the fabrication might be needed to decrease optical losses.

Appendix A

Fabrication procedure for diamond nanoposts and silver apertures

While we have described the procedure for fabricating our diamond devices in the previous chapters, here we consolidate the recipes and provide details of the processes.

A.1 Ion implantation and annealing

The devices were fabricated on electron grade IIa diamonds with low nitrogen concentration (< 5 ppb) from Element 6. To prepare the samples for ion implantation, we first performed a stress-reliving etch to remove the top $\sim 2\mu m$ from the surface (etching parameters: 10 min with 30 sccm of O_2, at 700W ICP power, 100 W bias power and a chamber pressure of 10 mtorr). We cleaned the surface of the NV centers with a 1:1:1 mix of sulfuric: nitric: perchloric acids prior and after the etch. The diamond samples were adhered to 4-in silicon wafers using carbon tape and sent to Core Systems for implantation of nitrogen ions (^{15}N). The implantation conditions were selected based on SRIM calculations and a table of values is given below. The dosages are chosen to ensure a dense layer of NV centers so that there would be a high yield of single center devices after the etching of nanoposts (cross section $\sim 0.007\mu m^2$). Furthermore, the creation of NV centers depends on both the concentration of nitrogen ions as well as the number of generated vacancies, which increases with increasing energy. Therefore, the creation efficiency also increases with ion energy until it levels off at energies greater than 1 MeV. We have accordingly chosen the dosages based on the efficiency curve provided in [125]. After implantation, the samples were annealed in vacuum ($\sim 9 \times 10^{-7}$ T) at 800°C for two hours. The samples were cleaned with the tri-acid recipe both before and after annealing.

Table A.1: Implantation parameters

Depth (nm)	Energy (keV)	Dosage (cm^{-2})
20	14	1.25×10^{12}
90	75	1.5×10^{11}

A.2 Electron beam lithography and reactive ion etching

The samples were written using 2 layers of the negative electron beam resist XR 6% (Dow Corning) on either a 100 keV or 125 keV electron beam writer (Elionix). Prior to resist spinning, the samples were baked on a 180°C hotplate and then treated to a weak O_2 plasma for 1 minute (20 sccm at 80 W with a chamber pressure of ~ 300 mTorr). The first layer of resist was spun at 3000 rpm for 40 s, and the sample was subsequently baked at 120° C for 5 minutes. The second layer of resist was applied at the same spin speed, and the final bake steps are 5 minutes at 180° C followed by another 5 minutes at 120° C.

The patterns were written with a write field of 150×150 μm^2 with a resolution of 60000 dots per line. The currents used are 100 pA (for the 100 keV system) and 500 pA (for the 125 keV) system. The suitable dosages are around 3000 $\mu C/cm^2$. We normally vary the dosages by about 20% around the optimal dosage to fabricate nanoposts of different sizes.

The samples were developed in 25% TMAH for 17 s, followed by rinsing in DI water for 5 minutes with constant, gentle agitation and change of medium.

We then used RIE (Unaxis shuttle-line) to transfer the mask pattern onto the diamond sample. To generate posts that are $\sim$ 200-nm tall, a short etch of 65 s can be applied, with 30 sccm of O_2, 700 W ICP power, 100 W bias power, and a pressure of 10 mtorr.

The mask can be removed in HF and generally a quick, 1 minute HF (49%) etch is enough to remove the mask. The samples were then cleaned again in a tri-acid recipe before characterization

A.3 Silver deposition

We investigated several methods of silver deposition, including electron beam evaporation (on both Sharon and Denton) and DC sputtering (AJA). Prior to silver deposition, the sample was thoroughly cleaned with acid treatment. For electron beam evaporation, we found that direct evaporation of silver onto the substrate resulted in poor adhesion, in which the entire silver film could be easily peeled off. We thus evaporated a thin (1-2 nm) layer of titanium as an adhesion layer before deposition silver. The deposition pressure is in the high 10^7 T, and the evaporation rate is set to 2 A/s. 500 nm of silver was evaporated and the chamber was allowed to cool for around 10 minutes before it was vented. This is to minimize quick oxidation of silver after it comes into contact with the atmosphere. We also attempted to vary evaporation conditions by using our own silver pellets and slowing down the evaporation rate to $<$ 1 A/s. However, this did not seem to have improved the silver quality. Annealing of the thick silver film in a rapid thermal processor also did not improve the optical quality of the film. The samples were annealed for 3 minutes at 200-300

°C with forming gas, but in each attempt, the films roughened and a white tint was formed on the surface.

We also attempted DC sputtering of the silver films, which seemed to have yielded the best results so far. The chamber was pumped down to the low 10^6 T range before film deposition. The silver film was deposited at a pressure of 4 mT, with an Ar flow rate of 15 sccm, and an applied DC power of 100 W (with current 239 mA and voltage 391 V). To deposit a 500-nm thick film, the deposition time was 36 min.

A.4 Alignment procedure for second electron beam lithography step

The second electron beam lithography step to write the gratings over the nanopost patterns was performed on the 125 keV beam writer, which provided better imaging of the sample due to the high voltage and current. We found that for good overlap between the gratings and existing pattern, it was necessary to place alignment markers within the same write field so that the procedure is unaffected by stitching errors inherent in the ebeam writing process. The CAD patterns for the first and second ebeam write steps are shown in Fig. A-1. In the left pattern, arrays of nanoposts along with markers indicating their radii can be seen. The alignment markers are around 5 μm by 2 μm, and are placed on opposite corners of the write field.

To define the gratings, we spun one layer of XR at 3000 rpm. The sample was first baked at 180°C for 5 minutes and then at 120°C for another 5 minutes. The write current for the writing was 1 nA, and we fed locations of the markers in each array to the ebeam writer by imaging through the XR layer. The rotation tolerance was set to < 0.05 mrad. After ebeam writing, the sample was developed in 25% TMAH for 17 s as before. Since cleaning the samples with tri-acid would remove the gratings (due to mechanical agitation), to ensure cleanliness of the surface prior to silver deposition,

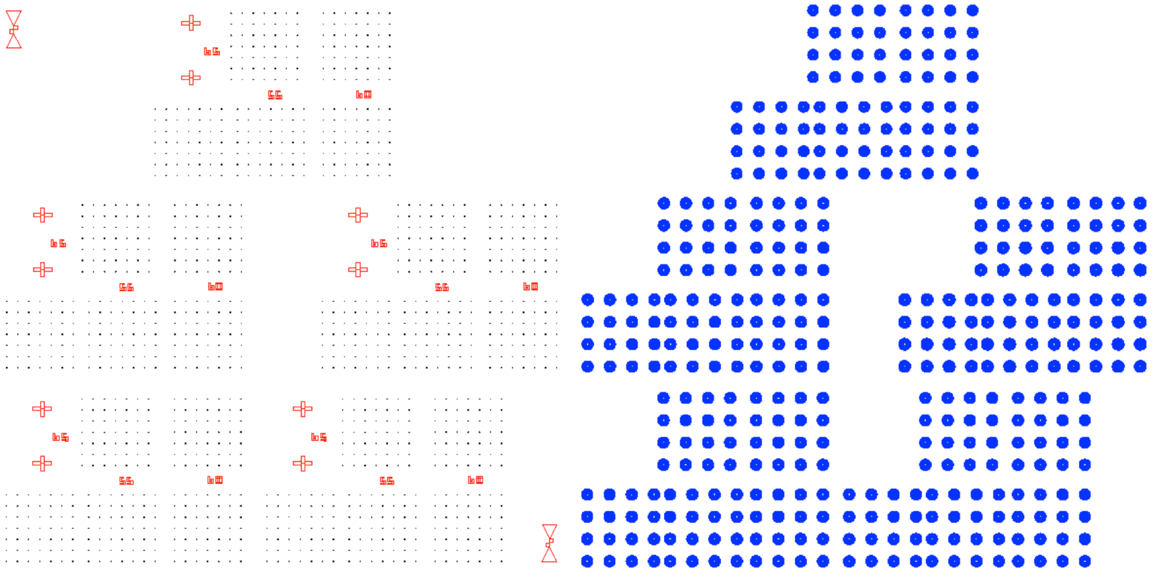

Figure A-1: CAD patterns for the first (left) and second (right) electron beam lithography steps.

we cleaned the sample in Piranha (3:1 H2SO4:H2O2) at 80° C, followed by annealing in the RTP at 465°C in an O_2 purged environment.

Appendix B

Optical characterization of single photon sources

Most of the optical characterization shown here was performed on a home-built confocal microscope with a 0.6 N.A. objective. Here, we provide a schematic of the setup and some details of the characterization.

The schematic of the microscope is shown in Fig. B-1a. The excitation source (i.e. 532 nm CW and pulsed laser) delivered via a single mode fiber in the green wavelengths is coupled into the setup through a collimator (FiberPort, Thorlabs) and reflected from a dichroic beamsplitter (Semrock, Di02-R532). It is focused onto the sample using air objective (Olympus LUCPlanFLN 40x, N.A. 0.6). The objective has a long working distance of around 4 mm and has a coverslip correction collar, which are advantageous for focusing the light through a thick layer of diamond. The fluorescence is collected by the same objective and passes through the dichroic splitter. Both the incoming and collected signals were scanned by a fast steering mirror (Newport). The signal is then spectrally filtered using a 630 nm notch filter, a 650 nm long pass filter (removed for experiments in which the 637 nm line needs to be collected), and a 800 nm short pass filter. The collimated light is then focused onto a single mode fiber

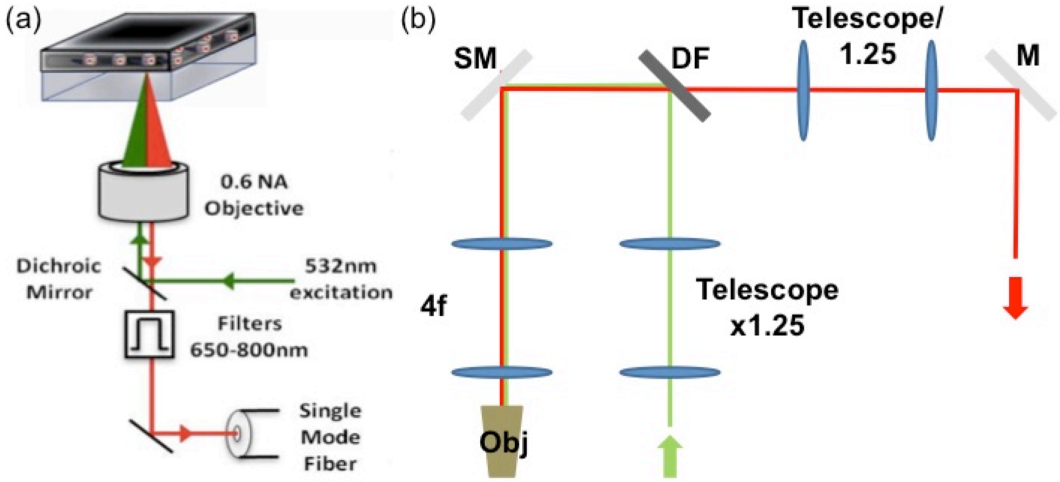

Figure B-1: (a) Schematic of the confocal microscope. (b) Schematic of the imaging lenses in the setup. Here, M = mirror, DF = dichroic beamsplitter, SM = scanning mirror.

(one of the inputs of a 2x2 coupler for 630 nm, Thorlabs) using another Fiberport. There is a small amount of reflected signal at the other input end, and these photons are not collected in our experiment. The fiber splits the signal so that both outputs can be sent to avalanche photodiodes (APD, Perkin Elmer) for photodetection and measurement of photon statistics. In general, due to the broad emission of the NV center, the splitting of photon signal is not even, with one arm having roughly 50% more counts. Moreover, we found that covering the fiber with black plastic has helped the reduction of background counts from stray light in the room. Due to the mismatches in the clear apertures of the objective and fiber collimators, it was necessary to modify the sizes of the collimated beam throughout the setup to provide optimal collection. Therefore, we have implemented several telescopes (Fig. B-1b), consisting of lenses with different focal distances, to adjust the beam size. 4F imaging was implemented elsewhere on the setup to provide good mapping of sample and image planes.

Photon statistics were measured by sending the APD outputs to a time-correlated single photon counting module (TCSPCM, PicoHarp). In general, the integration bin widths were set to 512 ps for faster acquisition, although for devices with shorter lifetimes and most lifetime measurements, bin widths of 128 ps (around the timing resolution of the APD) were used. Spectral data were acquired by sending the fiber coupled signal to a grating spectrometer (Jobin Yvon iHR550). A lens is used to focus the signal through the slit of the spectrometer entrance. For the measurements shown here, the slit has been narrowed to 1 mm. A 76 mm x 76 mm monochromator with 150 g/mm gratings and a TE-cooled CCD camera was used for detection.

As mentioned in the main text, green pulses for time-resolved measurements were generated by passing ultrafast (∼200 fs) pulses at ∼800 nm from a Ti-Sapphire laser (Coherent) through a photonic crystal fiber (Newport). The resulting supercontinuum white light is spectrally filtered using bandpass filters between 510 and 540nm (Semrock) and coupled into a single mode fiber for the green wavelengths. Under good alignment conditions, over 1 mW of averaged green power can be collected in the fiber at the fundamental repetition rate of 76 MHz. The repetition rate can be reduced by using an electro-optic modulator (EOM, ConOptics) and good extinction of pulses can be achieved with careful alignment of the beam with the polarization axis of the EOM. For lifetime measurements, it is necessary to provide a sync signal to the TCSPCM. This is done by adding a beamsplitter in the path of the green pulses prior to fiber collection and focusing the signal onto a fast photodetector (Thorlabs), which in turn sends the sync signal to one of the inputs on the TCSPCM.

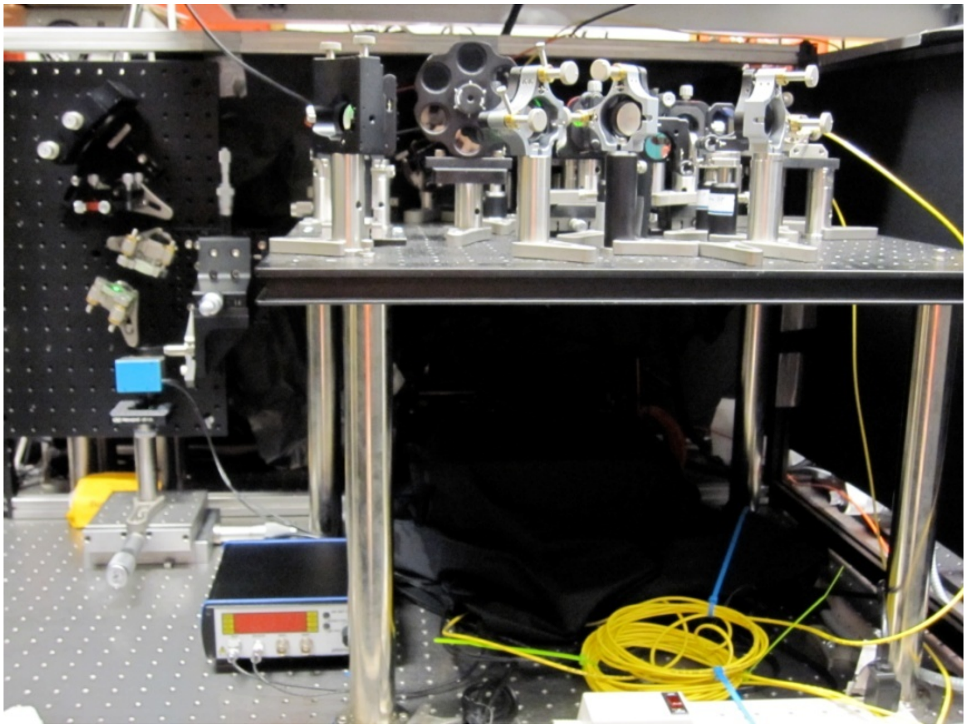

Figure B-2: Photo of the confocal microscope.

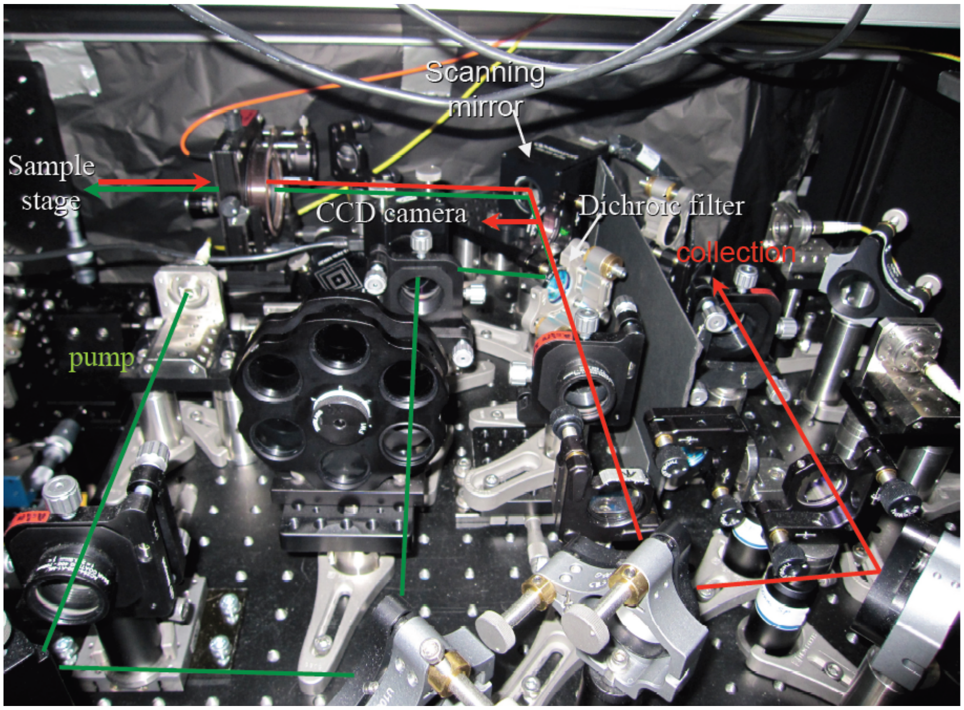

Figure B-3: Optics on the breadboard.

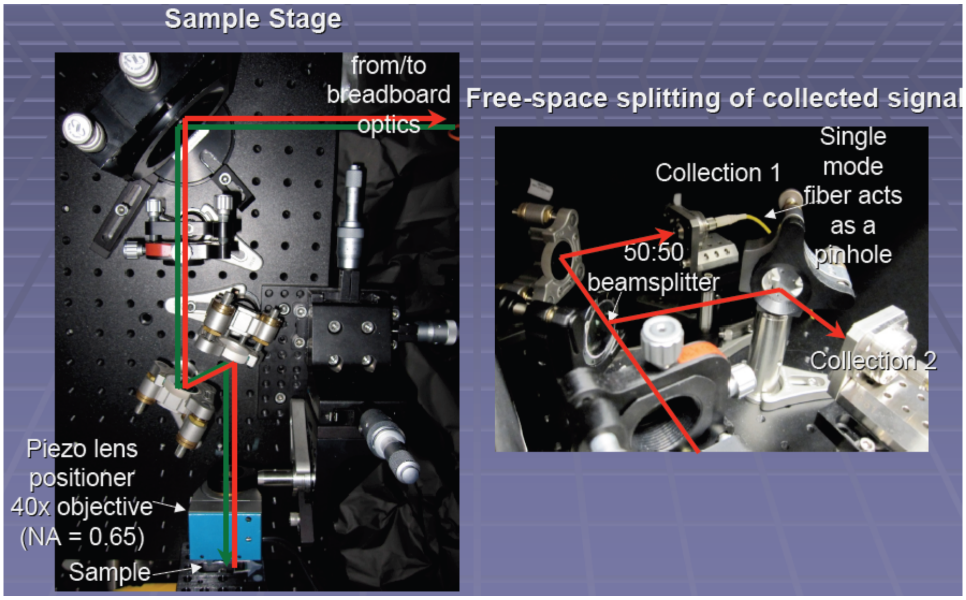

Sample Stage

Free-space splitting of collected signal

Figure B-4: Sample stage and free-space to fiber coupling optics.

Appendix C

Time-resolved $g^{(2)}$ measurements

In this section, we use time-resolved measurements to separate NV contribution from the background. This technique can help identify single emitter-containing devices in the presence of high background, as is the case for some diamond-silver devices. We first consider Fig. C-1, which shows that the fluorescence decay time trace of a single NV center can be fitted to a tri-exponential model, which yields two faster time constants around 0.3 ns and 1.4 ns, and a slower time constant around 2–3 ns. A decay curve taken of the background can be fitted to a bi-exponential, which gave comparable time constants to the fast decaying components in the first case. The slow time constant can thus be attributed to the NV center, while the faster decays arise from the background.

Fig. C-2 shows a histogram of coincidence counts for a diamond-silver aperture

	Time Constants (ns)				
	$\tau_{3,1}$	$\tau_{3,2}$	$\tau_{3,3}$	$\tau_{2,1}$	$\tau_{2,2}$
NV 1	3.45	1.53	0.31	0.34	3.22
NV 2	3.28	1.2	0.28	0.3	2.46
NV 3	2.84	1.4	0.27	0.28	2.77
BG				0.35	1.58

Figure C-1: Time constants $\tau_{m,n}$ for exponential fits to the fluorescence decay traces taken of several single NV centers in diamond-silver apertures and the background. m refers to total number of time constants assumed for the fit.

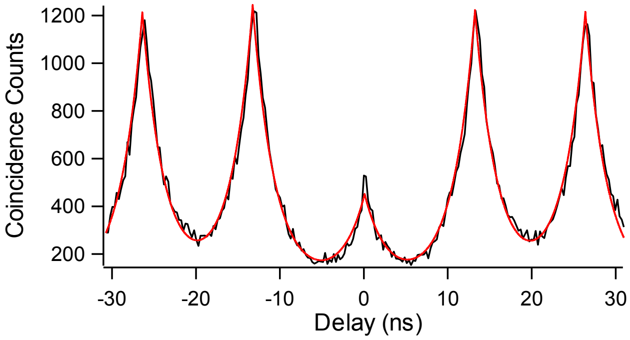

Figure C-2: Histogram of coincidence counts for a diamond-silver aperture under pulsed excitation, along with fit to a single exponential.

under pulsed excitation, with considerable signal at zero delay. This can be fitted to the model $g^{(2)}(\tau) = c_{bg} + \sum_{k=-N}^{N} c_k e^{-\frac{(t-k\tau_{rep})}{\tau_{NV}}}$, where τ_{NV} is the lifetime of the NV center, τ_{rep} is the time interval between successive pulses, and N is the number of peaks on each side of the central peak. This fit yields NV lifetime $\tau_{NV} = 2.62$ ns, the coefficient at zero delay $c_0 = 367$, and the coefficients for $k \neq 0$, $c_k \sim 1130$. It can be seen that the data deviates from the fit at around zero delay.

By taking into account the fast decaying background and using a bi-exponential fit, in which $g^{(2)}(\tau) = c_{bg} + \sum_{k=-N}^{N} c_k e^{-\frac{(t-k\tau_{rep})}{\tau_{NV}}} + \sum_{k=-N}^{N} b_k e^{-\frac{(t-k\tau_{rep})}{\tau_{bg}}}$, we obtain a much better agreement between the fit and data (Fig. C-3). The fit parameters are $\tau_{NV} = 2.62$ ns, $c_0 \sim 0$, $c_k \sim 1000$, background lifetime $\tau_{bg} = 1.51 ns$, and the coefficient for the background at zero delay, $b_0 = 393$. The NV lifetime value is consistent between the two fits, while the background time constant corroborates with our previous lifetime data. The bi-exponential fit shows that at zero delay, contribution to the signal comes from the background only. This suggests that there is only one emitter in the device.

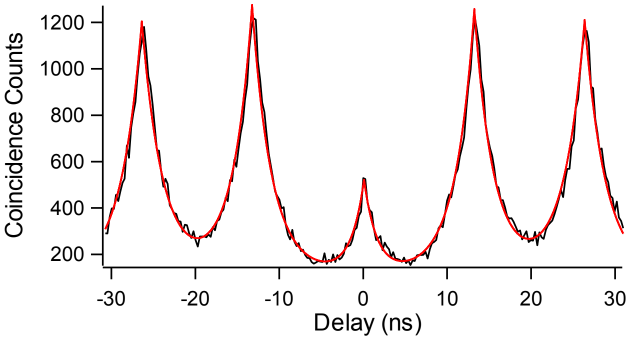

Figure C-3: Histogram of coincidence counts for the same diamond-silver aperture under pulsed excitation, along with fit to a bi-exponential.

Appendix D

Fabrication procedure for TiO_2 devices

D.1 General fabrication procedure

We use standard top-down fabrication methods to make devices in amorphous and anatase TiO_2 thin films. The pattern is written in a positive electron beam resist (ZEP) using a 100 keV electron beam lithography system (Elionix). Prior to ebeam writing, the samples are first cleaned using standard solvent cleaning processes (sonication for 5 mins in acetone, and then another 5 mins in IPA). The sample is then baked for 10 mins on a 180°C hotplate and subsequently treated to an O_2 plasma (20 sccm, 80 W) for 2 mins. The ZEP is spun at 6000 rpm for 40 s, and baked at 180° for 3 mins.

The patterns are written with a 300×300 μm^2 write field, with a beam current of 100 pA and dosages around 400 $\mu C/cm^2$. The resist is developed in o-xylene for 30 s and then rinsed in IPA for another 30 s. We then deposit a 50-nm thick chromium film using electron beam evaporation (Sharon) at low pressure (in the 10^{-7} T range) and slow rate (0.5 A/s). The mask is then lift off in remover PG, under gentle agitation and constant change in medium. In cases where the lift off process is slow, a very short sonication (10 s) step may be applied.

The metal pattern is transferred into the TiO_2 film using reactive ion etching (Nexx), using gas flow rates of 16 sccm CF_4 and 4 sccm H_2, microwave power of 300 W, RF power of 150 W, and at a pressure of 5 mTorr. The etch rate of the films is approximately 60 nm/min and the recipe leaves of 75° taper in the sidewalls of the structures. After etching, the etch mask is removed using Cr etchant (3 mins), and thoroughly rinsed in DI water.

D.2 Attempts to fabricate photonic crystal nanocavities

We investigated the fabrication of photonic crystal nanobeam cavities on TiO_2 thin films deposed on silicon. To realize smoother features, we avoided the chromium liftoff procedure by using 2 layers of ZEP resist (spun at slower spin rates of 2500 rpm). This is necessary due to the low selectivity of the polymer mask in the etch recipe. The polymer mask can be removed by Piranha clean after etching (Fig. D-1).

To release the nanobeam cavity, we used a 1:4 KOH:H2O solution to etch the exposed Si at 65 °C. While KOH etches silicon selectively along the 100 crystal plane, we found the wet etching to be wildly inconsistent, resulting in erosion in the nanobeams in some cases where the etch temperature is etched too high (Fig. D-2). To date, we have not found a good recipe for releasing TiO_2 structures from silicon or SiO_2 substrates.

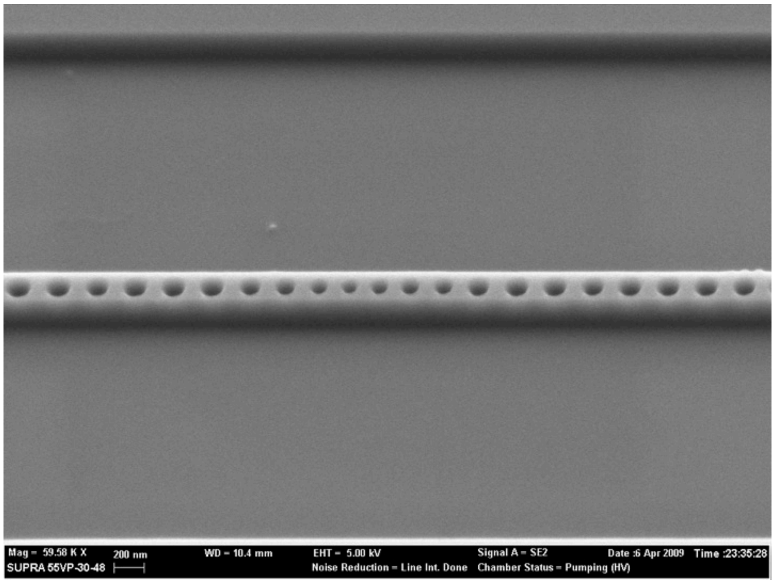

Figure D-1: SEM image of etched TiO_2 photonic crystal cavity before release of sacrificial silicon layer.

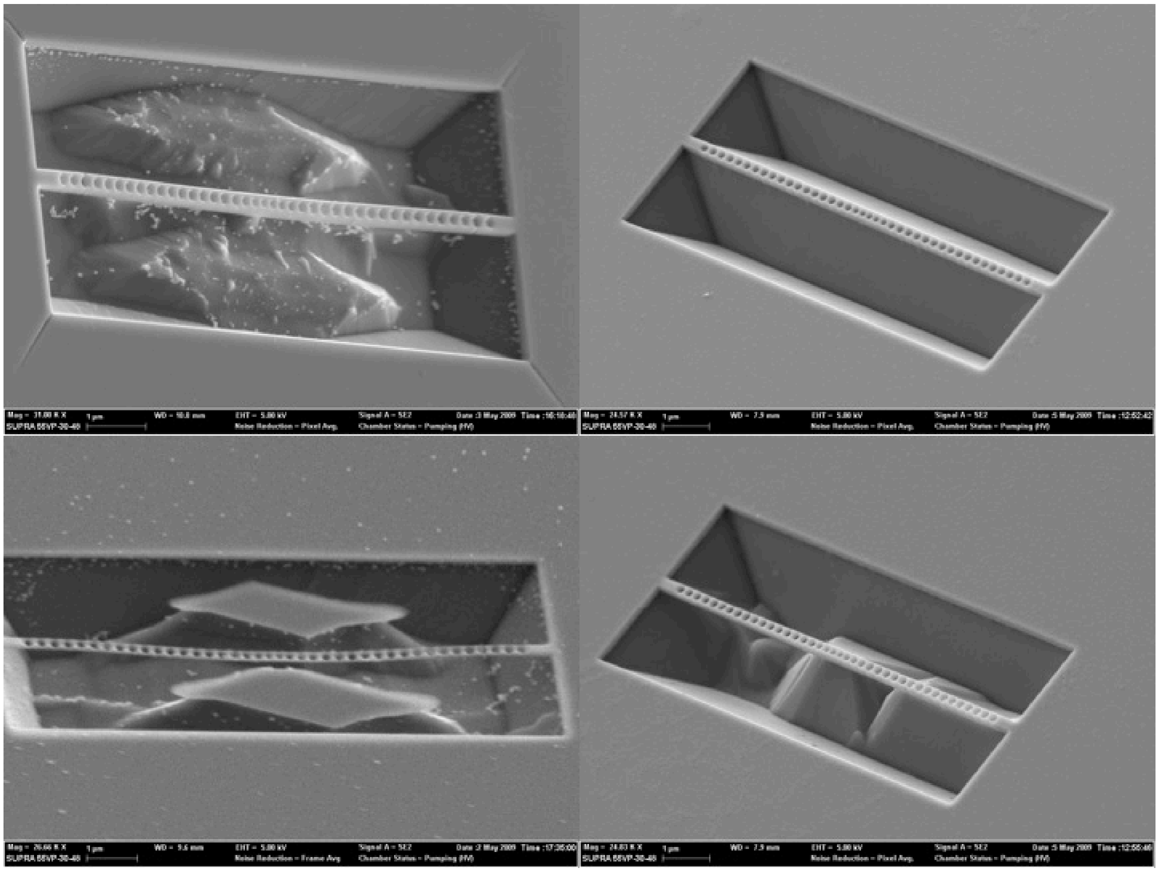

Figure D-2: SEM image of nanobeam cavities after wet-etching by KOH.

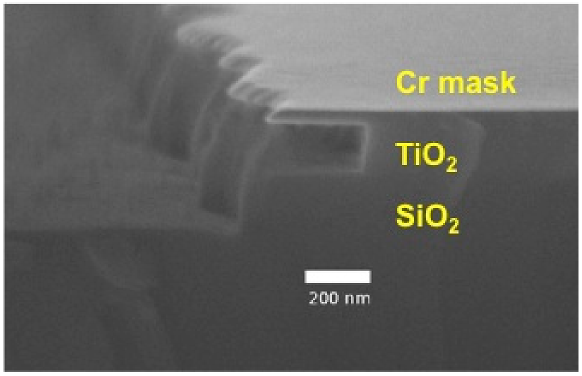

Figure D-3: SEM image of the etch profile of a $CF_4/O_2/Ar$ recipe.

D.3 Alternative etch recipes

While the CF_4/H_2 etch recipe provides generally good anisotropy and smoothness, there are a few limitations, including incompatibility with various etch masks and low selectivity in comparison to the underlying substrate (SiO_2). Moreover, the etch conditions can be inconsistent, depending on the condition of the etcher. We have therefore investigated several alternative (and unoptimized) recipes which are outlined below:

- A $CF_4/O_2/Ar$ (Nexx) etch chemistry provides fast etch rates (~ 154 nm/min), with a selectivity to SiO_2 of ~ 1.1. However, we observed undercutting of the TiO_2 layer and occasionally deposition of material around the etched edges (Fig. D-3)

- A $BCl_3/Cl_2/Ar$ (Unaxis) etch chemistry can potentially have excellent selectivities to both SiO_2 and silicon (< 1). However, the etch rates appeared to be much slower than CF_4-based recipes (~ 22 nm/min) and the sidewalls have a severe taper (Fig. D-4).

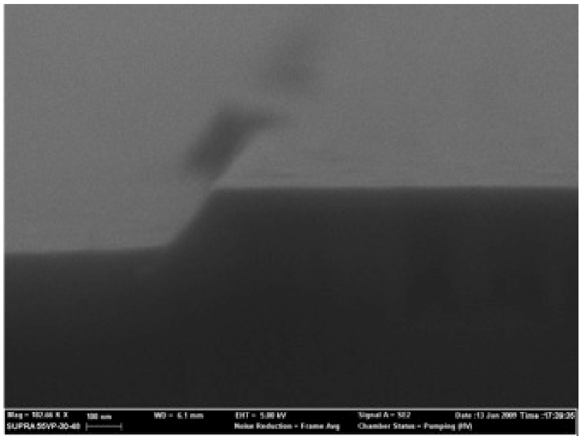

Figure D-4: SEM image of the etch profile of a $BCl_3/Cl_2/Ar$ recipe.

Bibliography

[1] T.M. Babinec, B.J.M. Hausmann, M. Khan, Y. Zhang, J. Maze, P.R. Hemmer, and M. Loncar. A diamond nanowire single photon source. *Nature Nanotech.*, 5:195–199, 2010.

[2] B. Hausmann, M. Khan, Y. Zhang, T. Babinec, K. Martinick, M. McCutcheon, P. Hemmer, and M. Loncar. Fabrication of diamond nanowires for quantum information processing applications. *Diam. Relat. Mater.*, pages 621–629, 2010.

[3] M.K. Chin, C. Youtsey, W. Zhao, T. Pierson, Z. Ren, S.L. Wu, L. Wang, Y.G. Zhao, and S.T. Ho. Gaas microcavity channel-dropping filter based on a race-track resonator. *IEEE Photonic. Tech. L.*, pages 1620–1622, 1999.

[4] B.J.M. Hausmann, T.M. Babinec, J.T. Choy, J.S. Hodges, S. Hong, I. Bulu, A. Yacoby, M.D. Lukin, and M. Loncar. Single color centers implanted in diamond nanostructures. *New J. Phys.*, page 045004, 2011.

[5] T. M. Babinec, J. T. Choy, K. J. M. Smith, M. Khan, and M. Loncar. Design and focused ion beam fabrication of single crystal diamond nanobeam cavities. *J. Vac. Sci. Technol. B*, 29 (1):010601, 2011.

[6] I. Bulu, T. Babinec, B. Hausmann, J.T. Choy, and M Loncar. Plasmonic resonators for enhanced diamond nv- center single photon sources. *Opt. Express*, pages 5268–5276, 2011.

[7] J. T. Choy, B. J. M. Hausmann, T. M. Babinec, I. Bulu, M. Khan, P. Maletinsky, A. Yacoby, and M. Loncar. Enhanced single photon emission from a diamond-silver aperture. *Nature Photon.*, 5:738, 2011. Submitted.

[8] J.D. Bradley, C.C. Evans, J.T. Choy, O. Reshef, P.B. Deotare, F. Parsy, K.C. Phillips, M. Loncar, and E. Mazur. Submicrometer-wide amorphous and polycrystalline anatase tio2 waveguides for microphotonic devices. *Opt. Express*, pages 23821–23831, 2012.

[9] J.T. Choy, J.D.B. Bradley, P.B. Deotare, I.B. Burgess, C.C. Evans, E. Mazur, and M. Lončar. Integrated tio2 resonators for visible photonics. *Opt. Lett.*, 37(4):539–541, Feb 2012.

[10] R.S. Balmer, I. Friel, S.M. Woollard, C.J.H. Wort, G.A. Scarsbrook, S.E. Coe, H. El-Hajj, A. Kaiser, A. Denisenko, E. Kohn, and J. Isberg. Unlocking diamond's potential as an electronic material. *Phil. Trans. R. Soc. A*, 366:251 – 265, 2008.

[11] J. Isberg, J. Hammersberg, E. Johansson, T. Wikstrom, D.J. Twitchen, A.J. Whitehead, S.E. Coe, and G.A. Scarsbrook. High carrier mobility in single-crystal plasma-deposited diamond. *Diamond and Related Materials*, 9(9 - 10):1726 – 1729, 2000.

[12] S.E Coe and R.S Sussmann. Optical, thermal and mechanical properties of cvd diamond. *Diamond and Related Materials*, 9(9 - 10):1726 – 1729, 2000.

[13] J.-P.M. Feve, K.E. Shortoff, M.J. Bohn, and J.K. Brasseur. High average power diamond raman laser. *Opt. Express*, 19(2):913–922, Jan 2011.

[14] A.M. Zaitsev. *Optical properties of diamond: a data handbook*. Springer-Verlag, 2001.

[15] I. Aharonovich, S. Castelletto, D.A. Simpson, C.-H. Su, A.D. Greentree, and S. Prawer. Diamond-based single-photon emitters. *Rep. Prog. Phys.*, 74:076501, 2011.

[16] C. Kurtsiefer, S. Meyer, P. Zarda, and H. Weinfurter. Stable solid-state source of single photons. *Phys. Rev. Lett.*, pages 290–293, 2000.

[17] E. Neu, D. Steinmetz, J. Riedrich-Mller, S. Gsell, M. Fischer, M. Schreck, and C. Becher. Single photon emission from silicon-vacancy colour centres in chemical vapour deposition nano-diamonds on iridium. *New Journal of Physics*, 13(2):025012, 2011.

[18] T. Gaebel, I. Popa, A. Gruber, M. Domhan, F. Jelezko, and J. Wrachtrup. Stable single-photon source in the near infrared. *New Journal of Physics*, 6(1):98, 2004.

[19] I. Aharonovich, S. Castelletto, D.A. Simpson, A. Stacey, J. McCallum, A.D. Greentree, and S. Prawer. Two-level ultrabright single photon emission from diamond nanocrystals. *Nano Letters*, 9(9):3191–3195, 2009. PMID: 19670845.

[20] G.D. Fuchs, V.V. Dobrovitski, D.M. Toyli, F.J. Heremans, and D.D. Awschalom. Gigahertz dynamics of a strongly driven single quantum spin. *Science*, 326(5959):1520–1522, 2009.

[21] A. Jarmola, V.M. Acosta, K. Jensen, S. Chemerisov, and D. Budker. Temperature- and magnetic-field-dependent longitudinal spin relaxation in nitrogen-vacancy ensembles in diamond. *Phys. Rev. Lett.*, 108:197601, May 2012.

[22] F. Jelezko and J. Wrachtrup. Single defect centres in diamond: A review. *physica status solidi (a)*, 203(13):3207–3225, 2006.

[23] A. Beveratos, R. Brouri, T. Gacoin, A. Villing, J.-P Poizat, and P. Grangier. Single photon quantum cryptography. *Phys. Rev. Lett.*, page 187901, 2002.

[24] L. Childress, M. V. Gurudev Dutt, J. M. Taylor, A. S. Zibrov, F. Jelezko, J. Wrachtrup, P. R. Hemmer, and M. D. Lukin. Coherent dynamics of coupled electron and nuclear spin qubits in diamond. *Science*, 314(5797):281–285, 2006.

[25] M. V. Gurudev Dutt, L. Childress, L. Jiang, E. Togan, J. Maze, F. Jelezko, A. S. Zibrov, P. R. Hemmer, and M. D. Lukin. Quantum register based on individual electronic and nuclear spin qubits in diamond. *Science*, 316(5829):1312–1316, 2007.

[26] P. C. Maurer, G. Kucsko, C. Latta, L. Jiang, N. Y. Yao, S. D. Bennett, F. Pastawski, D. Hunger, N. Chisholm, M. Markham, D. J. Twitchen, J. I. Cirac, and M. D. Lukin. Room-temperature quantum bit memory exceeding one second. *Science*, 336(6086):1283–1286, 2012.

[27] Y. Kubo, F. R. Ong, P. Bertet, D. Vion, V. Jacques, D. Zheng, A. Dréau, J.-F. Roch, A. Auffeves, F. Jelezko, J. Wrachtrup, M. F. Barthe, P. Bergonzo, and D. Esteve. Strong coupling of a spin ensemble to a superconducting resonator. *Phys. Rev. Lett.*, 105:140502, Sep 2010.

[28] O. Arcizet, V. Jacques, A. Siria, P. Poncharal, P. Vincent, and S. Seidelin. A single nitrogen-vacancy defect coupled to a nanomechanical oscillator. *Nature Physics*, 7:879–883, 2011.

[29] J. R. Maze, P. L. Stanwix, J. S. Hodges, S. Hong, J. M. Taylor, P. Cappellaro, L. Jiang, M. V. Gurudev Dutt, E. Togan, A. S. Zibrov, A. Yacoby, R. L. Walsworth, and M. D. Lukin. Nanoscale magnetic sensing with an individual electronic spin in diamond. *Nature*, 455:644, 2008.

[30] G. Balasubramanian, I. Y. Chan, R. Kolesov, M. Al-Hmoud, J. Tisler, C. Shin, C. Kim, A. Wojcik, P. R. Hemmer, A. Krueger, T. Hanke, A. Leitenstorfer, R. Bratschitsch, F. Jelezko, and J. Wrachtrup. Nanoscale imaging magnetometry with diamond spins under ambient conditions. *Nature*, 455(7213):648–651, October 2008.

[31] P. Maletinsky, S. Hong, M.S. Grinolds, B.J.M. Hausmann, M.D.Lukin, R.-L. Walsworth, M. Loncar, and A. Yacoby. A robust, scanning quantum system for nanoscale sensing and imaging. *Nature Nanotech.*, 7:320, 2012. Submitted.

[32] J.P. Hadden, J.P. Harrison, A.C. Stanley-Clarke, L. Marseglia, Y-L.D. Ho, B.R. Patton, J.L. O'Brien, and J.G. Rarity. Monolithic diamond optics for single photon detection. *App. Phys. Lett.*, page 241901, 2010.

[33] P. Siyushev, F. Kaiser, V. Jacques, I. Gerhardt, S. Bischof, H. Fedder, J. Dodson, M. Markham, D. Twitchen, F. Jelezko, and J. Wrachtrup. Nmr and quantum information processing. *App. Phys. Lett.*, page 241902, 2010.

[34] T. Schroder, F. Gadeke, M.J. Banholzer, and O. Benson. Ultrabright and efficient single-photon generation based on nitrogen-vacancy centres in nanodiamonds on a solid immersion lens. *New J. Phys.*, page 055017, 2011.

[35] D. E. Chang, A. S. Srensen, E. A. Demler, and M. D. Lukin. A single-photon transistor using nanoscale surface plasmons. *Nat. Phys.*, 3:807–812, 2007.

[36] K. M. Birnbaum, R. Miller A. Boca, A. D. Boozer, T. E. Northup, and H. J. Kimble. Photon blockade in an optical cavity with one trapped atom. *Nature*, 436:87, 2005.

[37] B. B. Blinov, D. L. Moehring, L.-M. Duan, and C. Monroe. Observation of entanglement between a single trapped atom and a single photon. *Nature*, 428:153, 2004.

[38] P. Neumann, N. Mizuochi, F. Rempp, P. Hemmer, H. Watanabe, S. Yamasaki, V. Jacques, T. Gaebel, F. Jelezko, and J. Wrachtrup. Multipartite entanglement among single spins in diamond. *Science*, 320:1326, 2008.

[39] E. Togan, Y. Chu, A. S. Trifonov, L. Jiang, J. Maze, L. Childress, M. V. G. Dutt, A. S. Srensen, P. R. Hemmer, A. S. Zibrov, and M. D. Lukin. Quantum entanglement between an optical photon and a solid-state spin qubit. *Nature*, 466:730–734, 2010.

[40] P. Neumann, R. Kolesov, B. Naydenov, J. Beck, F. Rempp, M. Steiner, V. Jacques, G. Balasubramanian, M. L. Markham, D. J. Twitchen, S. Pezzagna, J. Meijer, J. Twamley, F. Jelezko, and J. Wrachtrup. Quantum register based on coupled electron spins in a room-temperature solid. *Nature Phys.*, 6:249, 2010.

[41] Martial Ducloy and Daniel Bloch. *Quantum Optics of Confined Systems.* Kluwer Academic Publishers, 1996.

[42] J. McKeever, A. Boca, A. D. Boozer, R. Miller, J. R. Buck, A. Kuzmich, and H. J. Kimble. Deterministic generation of single photons from one atom trapped in a cavity. *Science*, 303:1992, 2004.

[43] L. Novotny and B. Hecht. *Principles of Nano-Optics.* Cambridge University Press, 2007.

[44] B. J. M. Hausmann, J. T. Choy, T. M. Babinec, B. J. Shields, I. Bulu, M. D. Lukin, and Marko Lonar. Diamond nanophotonics and applications in quantum science and technology. *physica status solidi (a)*, 209(9):1619–1630, 2012.

[45] V. M. Acosta, C. Santori, A. Faraon, Z. Huang, K.-M. C. Fu, A. Stacey, D. A. Simpson, K. Ganesan, S. Tomljenovic-Hanic, A. D. Greentree, S. Prawer, and R. G. Beausoleil. Dynamic stabilization of the optical resonances of single nitrogen-vacancy centers in diamond. *Phys. Rev. Lett.*, 108:206401, May 2012.

[46] A. Beveratos, R. Brouri, T. Gacoin, J.-P Poizat, and P. Grangier. Nonclassical radiation from diamond nanocrystals. *Phys. Rev. A*, page 061802(R), 2001.

[47] D. Englund, B. Shields, K. Rivoire, F. Hatami, J. Vuckovic, H. Park, and M.D. Lukin. Deterministic coupling of a single nitrogen vacancy center to a photonic crystal cavity. *Nano Lett.*, pages 3922–3926, 2010.

[48] T. van der Sar, J. Hagemeier, W. Pfaff, E.C. Heeres, S.M. Thon, H. Kim, P.M. Petroff, T.H. Oosterkamp, D. Bouwmeester, and R. Hanson. Deterministic nano-assembly of a coupled quantum emitter - photonic crystal cavity system. *App. Phys. Lett.*, page 193103, 2011.

[49] J. Wolters, N. Sadzak, A. W. Schell, T. Schroeder, and O. Benson. Ultrafast spectral diffusion measurement on nitrogen vacancy centers in nanodiamonds using correlation interferometry. *arXiv:1206.0852v1*, 2012. arXiv:1206.0852v1.

[50] P. Olivero, S. Rubanov, P. Reichart, B. C. Gibson, S. T. Huntington, J. Rabeau, A. D. Greentree, J. Salzman, D. Moore, D. N. Jamieson, and S. Prawer. Ion-beam-assisted lift-off technique for three-dimensional micromachining of free-standing single-crystal diamond. *Adv. Mater.*, 17:2427–2430, 2005.

[51] I. Aharonovich, J. C. Lee, A. P. Magyar, B. B. Buckley, C. G. Yale, D. D. Awschalom, and E. L. Hu. Homoepitaxial growth of single crystal diamond membranes for quantum information processing. *Adv. Matter.*, 24 (10):OP54, 2012.

[52] A. P. Magyar, J. C. Lee, A. M. Limarga, I. Aharonovich, F. Rol, D. R. Clarke, M. Huang, and E. L. Hu. Fabrication of thin, luminescent, single-crystal diamond membranes. *Appl. Phys. Lett.*, 99:081913, 2011.

[53] T. Schrder, F. Gdeke, M. J. Banholzer, and O. Benson. Ultrabright and efficient single-photon generation based on nitrogen-vacancy centres in nanodiamonds on a solid immersion lens. *New J. Phys.*, 13:055017, 2011.

[54] I. Bayn, B. Meyler, A. Lahav, J. Salzman, R. Kalish, B. A. Fairchild, S. Prawer, M. Barth, O. Benson, T. Wolf, P. Siyushev, F. Jelezko, and J. Wrachtrup. Processing of photonic crystal nanocavity for quantum information in diamond. *Diam. Relat. Mater.*, 20 (7):937, 2011.

[55] J. Riedrich-Moeller, L. Kipfstuhl, C. Hepp, E. Neu, C. Pauly, F. Muecklich, A. Baur andM. Wandt, S. Wolff, M. Fischer, S. Gsell, M. Schreck, and C. Becher. One- and two-dimensional photonic crystal microcavities in single crystal diamond. *Nature Nanotech.*, 7:69, 2012.

[56] A. Faraon, P.E. Barclay, C. Santori, K.-M.C. Fu, and R.G. Beausoleil. Resonant enhancement of the zero-phonon emission from a colour centre in a diamond cavity. *Nature Photon.*, pages 301–305, 2011.

[57] B.M. Hausmann, B.J. Shields, Q. Quan, P. Maletinsky, M.W. McCutcheon, J. Choy, T.M. Babinec, A. Kubanek, A. Yacoby, M.D. Lukin, and M. Loncar. Integrated diamond networks for quantum nanophotonics. *Nano Lett.*, page 1578, 2012.

[58] Andrei Faraon, Charles Santori, Zhihong Huang, Victor M. Acosta, and Raymond G. Beausoleil. Coupling of nitrogen-vacancy centers to photonic crystal cavities in monocrystalline diamond. *Phys. Rev. Lett.*, 109:033604, Jul 2012.

[59] K. Vahala. Optical microcavities. *Nature*, pages 839 – 846, 2003.

[60] Qimin Quan, Parag B Deotare, and Marko Loncar. Photonic crystal nanobeam cavity strongly coupled to the feeding waveguide. *Applied Physics Letters*, 96(20):203102–203102, 2010.

[61] A Faraon, I Fushman, D Englund, N Stoltz, P Petroff, and J Vucković. Dipole induced transparency in waveguide coupled photonic crystal cavities. *Optics express*, 16(16):12154, 2008.

[62] Igal Bayn and Joseph Salzman. Ultra high-q photonic crystal nanocavity design: The effect of a low-ϵ slab material. *Opt. Express*, 16(7):4972–4980, Mar 2008.

[63] S. Tomljenovic-Hanic, M. J. Steel, C. Martijn de Sterke, and J. Salzman. Diamond based photonic crystal microcavities. *Opt. Express*, 14(8):3556–3562, Apr 2006.

[64] Qimin Quan and Marko Loncar. Deterministic design of wavelength scale, ultra-high q photonic crystal nanobeam cavities. *Opt. Express*, 19(19):18529–18542, Sep 2011.

[65] Ph Lalanne and J.-P. Hugonin. Bloch-wave engineering for high-q, small-v microcavities. *Quantum Electronics, IEEE Journal of*, 39(11):1430–1438, 2003.

[66] Ph. Lalanne, S. Mias, and J. Hugonin. Two physical mechanisms for boosting the quality factor to cavity volume ratio of photonic crystal microcavities. *Opt. Express*, 12(3):458–467, Feb 2004.

[67] C. Sauvan, G. Lecamp, P. Lalanne, and J. Hugonin. Modal-reflectivity enhancement by geometry tuning in photonic crystal microcavities. *Opt. Express*, 13(1):245–255, Jan 2005.

[68] Murray W. McCutcheon and Marko Loncar. Design of a silicon nitride photonic crystal nanocavity with a quality factor of one million for coupling to a diamond nanocrystal. *Opt. Express*, 16(23):19136–19145, Nov 2008.

[69] Igal Bayn, Boris Meyler, Joseph Salzman, and Rafi Kalish. Triangular nanobeam photonic cavities in single-crystal diamond. *New Journal of Physics*, 13(2):025018, 2011.

[70] B. J. M. Hausmann, I. B. Bulu, P. B. Deotare, M. McCutcheon, V. Venkataraman, M. L. Markham, D. J. Twitchen, and M. Lonar. Integrated high-quality factor optical resonators in diamond. *Nano Letters*, 0(0):null, 0.

[71] Michael J. Burek, Nathalie P. de Leon, Brendan J. Shields, Birgit J. M. Hausmann, Yiwen Chu, Qimin Quan, Alexander S. Zibrov, Hongkun Park, Mikhail D. Lukin, and Marko Lonar. Free-standing mechanical and photonic nanostructures in single-crystal diamond. *Nano Letters*, 12(12):6084–6089, 2012.

[72] S.A. Maier. *Plasmonics: Fundamentals and Applications*. Springer, 2007.

[73] P.B. Catrysse and S. Fan. Propagating plasmonic mode in nanoscale apertures and its implications for extraordinary transmission. *Journal of Nanophotonics*, 2(1):021790–021790–20, 2008.

[74] P.B. Johnson and R.W. Christy. Optical constants of the noble metals. *Phys. Rev. B*, 6:4370–4379, Dec 1972.

[75] E.D. Palik. *Handbook of Optical Constants of Solids*. Academic Press, 1985.

[76] L. Novotny and C. Hafner. Light propagation in a cylindrical waveguide with a complex, metallic, dielectric function. *Phys. Rev. E*, 50:4094–4106, Nov 1994.

[77] Hocheol Shin, Peter B. Catrysse, and Shanhui Fan. Effect of the plasmonic dispersion relation on the transmission properties of subwavelength cylindrical holes. *Phys. Rev. B*, 72:085436, Aug 2005.

[78] T.M. Babinec, B.J.M. Hausmann, M. Khan, Y. Zhang, J.R. Maze, P.R. Hemmer, and M. Loncar. A diamond nanowire single-photon source. *Nat. Nanotechnol.*, pages 195–199, 2010.

[79] G.D. Fuchs, V.V. Dobrovitski, D.M. Toyli, F.J. Heremans, C.D. Weis, T. Schenkel, and D.D. Awschalom. Excited-state spin coherence of a single nitrogenvacancy centre in diamond. *Nat. Phys.*, pages 668–672, 2010.

[80] H. Chew. Radiation and lifetimes of atoms inside dielectric particles. *Phys. Rev. A*, pages 3411–3416, 1988.

[81] A. Gruber, A. Drabenstedt, C. Tietz, L. Fleury, J. Wrachtrup, and C. Borczyskowski. Scanning confocal optical microscopy and magnetic resonance on single defect centers. *Science*, pages 2012–2014, 1997.

[82] G. de Lange, Z.H. Wang, D. Riste, V.V. Dobrovitski, and R. Hanson. Universal dynamical decoupling of a single solid-state spin from a spin bath. *Science*, pages 60–63, 2010.

[83] K.-M.C. Fu, C. Santori, P.E. Barclay, L.J. Rogers, N.B. Manson, and R.G. Beausoleil. Observation of the dynamic jahn-teller effect in the excited states of nitrogen-vacancy centers in diamond. *Phys. Rev. Lett.*, page 256404, 2009.

[84] Jae-Ho Min, Gyeo-Re Lee, Jin-kwan Lee, Chang-Koo Kim, and Sang Heup Moon. Improvement of sio¡ sub¿ 2¡/sub¿ pattern profiles etched in cf¡ sub¿ 4¡/sub¿ and sf¡ sub¿ 6¡/sub¿ plasmas by using a faraday cage and neutral beams. *Surface and Coatings Technology*, 193(1):75–80, 2005.

[85] A. Gonzalez-Tudela, D. Martin-Cano, E. Moreno, L. Martin-Moreno, C. Tejedor, and F.J. Garcia-Vidal. Entanglement of two qubits mediated by one-dimensional plasmonic waveguides. *Phys. Rev. Lett.*, page 020501, 2011.

[86] H. J. Lezec, A. Degiron, E. Devaux, R. A. Linke, L. Martin-Moreno, F. J. Garcia-Vidal, and T. W. Ebbesen. Beaming light from a subwavelength aperture. *Science*, 297(5582):820–822, 2002.

[87] S. Carretero-Palacios, O. Mahboub, F. J. Garcia-Vidal, L. Martin-Moreno, Sergio G. Rodrigo, C. Genet, and T. W. Ebbesen. Mechanisms for extraordinary optical transmission through bull's eye structures. *Opt. Express*, 19(11):10429–10442, May 2011.

[88] A.G. Curto, G. Volpe, T.H. Taminiau, M.P. Kreuzer, R. Quidant, and N.F. van Hulst. Unidirectional emission of a quantum dot coupled to a nanoantenna. *Science*, 329(5994):930–933, 2010.

[89] H. Aouani, O. Mahboub, N. Bonod, E. Devaux, E. Popov, H. Rigneault, T.W. Ebbesen, and J. Wenger. Bright unidirectional fluorescence emission of molecules in a nanoaperture with plasmonic corrugations. *Nano Letters*, 11(2):637–644, 2011.

[90] N. Livneh, A. Strauss, I. Schwarz, I. Rosenberg, A. Zimran, S. Yochelis, G. Chen, U. Banin, Y. Paltiel, and R. Rapaport. Highly directional emission and photon beaming from nanocrystal quantum dots embedded in metallic nanoslit arrays. *Nano Letters*, 11(4):1630–1635, 2011.

[91] Y.C. Jun, K.C.Y. Huang, and M.L. Brongersma. Plasmonic beaming and active control over fluorescent emission. *Nature Communications*, 2:283, 2011.

[92] Jason C Reed, Hai Zhu, Alexander Y Zhu, Chen Li, and Ertugrul Cubukcu. Graphene-enabled silver nanoantenna sensors. *Nano letters*, 12(8):4090–4094, 2012.

[93] J Ihm, Steven G Louie, and Marvin L Cohen. Diamond-metal interfaces and the theory of schottky barriers. *Physical Review Letters*, 40(18):1208–1211, 1978.

[94] DA Evans, OR Roberts, GT Williams, AR Vearey-Roberts, F Bain, S Evans, DP Langstaff, and DJ Twitchen. Diamond–metal contacts: interface barriers and real-time characterization. *Journal of Physics: Condensed Matter*, 21(36):364223, 2009.

[95] M. Lipson. Guiding, modulating, and emitting light on silicon - challenges and opportunities. *J. Lightwave Technol.*, pages 4222 – 4238, 2005.

[96] E.S. Hosseini, S. Yegnanarayanan, A.H. Atabaki, M. Soltani, and A. Adibi. High quality planar silicon nitride microdisk resonators for integrated photonics in the visible wavelength range. *Opt. Express*, pages 14543–14551, 2009.

[97] C. B. Murray, C. R. Kagan, and M. G. Bawendi. Synthesis and characterization of monodisperse nanocrystals and close-packed nanocrystal assemblies. *Annu Rev Mater Sci*, pages 545–610, 2000.

[98] B. Lounis and W. E. Moerner. Single photons on demand from a single molecule at room temperature. *Nature*, pages 491–493, 2000.

[99] K. Rivoire, A. Faraon, and J. Vuckovic. Gallium phosphide photonic crystal nanocavities in the visible. *Appl. Phys. Lett.*, page 063103, 2008.

[100] M. Barth, N. Nusse, J. Stingl, B. Lchel, and O. Benson. Emission properties of high-q silicon nitride photonic crystal heterostructure cavities. *Physical Review Letters*, page 021112, 2008.

[101] M. Khan, T.M. Babinec, M. W. McCutcheon, P.B. Deotare, and M. Loncar. Fabrication and characterization of high-quality-factor silicon nitride nanobeam cavities. *Opt. Lett.*, page 421, 2011.

[102] Y. Gong and J. Vuckovic. Photonic crystal cavities in silicon dioxide. *Appl. Phys. Lett.*, page 031107, 2010.

[103] C. F. Wang, R. Hanson, D. D. Awschalom, E. L. Hu, T. Feygelson, J. Yang, and J. E. Butler. Fabrication and characterization of two-dimensional photonic crystal microcavities in nanocrystalline diamond. *Appl. Phys. Lett.*, page 201112, 2007.

[104] S. A. Campbell, H.-S. Kim, D. C. Gilmer, B. He, T. Ma, and W. L. Gladfelter. Titanium dioxide (tio_2)-based gate insulators. *IBM J. Res. Develop.*, pages 383–392, 1999.

[105] G. Subramania, Y.-J. Lee, A.J. Fischer, and D.D. Koleske. Log-pile tio_2 photonic crystal for light control at near-uv and visible wavelengths. *Adv. Mat.*, pages 1–5, 2009.

[106] T. Alasaarela, T. Saastamoinen, J. Hiltunen, A. Saynatjoki, A. Tervonen, P. Stenberg, M. Kuittinen, and S. Honkanen. Atomic layer deposited titanium dioxide and its application in resonant waveguide grating. *Appl. Opt.*, pages 4321–4325, 2010.

[107] M. Furuhashi, M. Fujiwara, T. Ohshiro, M. Tsutsui, K. Matsubara, M. Taniguchi, S. Takeuchi, and T. Kawai. Development of microfabricated tio_2 channel waveguides. *AIP Advances*, page 032102, 2011.

[108] P. K. Tien. Light waves in thin films and integrated optics. *Appl. Opt.*, 10(11):2395–2413, Nov 1971.

[109] N. Daldosso, M. Melchiorri, F. Riboli, F. Sbrana, L. Pavesi, G. Pucker, C. Kompocholis, M. Crivellari, P. Bellutti, and A. Lui. Fabrication and optical characterization of thin two-dimensional si3n4 waveguides. *Materials Science in Semiconductor Processing*, 7(46):453 – 458, 2004. ¡ce:title¿Papers presented at the E-MRS 2004 Spring Meeting Symposium C: New Materials in Future Silicon Technology¡/ce:title¿.

[110] Q. Quan, P.B. Deotare, and M. Loncar. Photonic crystal nanobeam cavity strongly coupled to the feeding waveguide. *Appl. Phys. Lett.*, page 203102, 2010.

[111] S. Fan. Sharp asymmetric lineshapes in side-coupled waveguide-cavity systems. *Appl. Phys. Lett.*, pages 908–910, 2002.

[112] L. Zhou and A. Poon. Electrically reconfigurable silicon microring resonator-based filter with waveguide-coupled feedback. *Opt. Express*, pages 9194–9204, 2007.

[113] A. Guarino, G. Poberaj, D. Rezzonico, R. Degl'Innocenti, and P. Gunter. Electrooptically tunable microring resonators in lithium niobate. *Nature Photon.*, pages 407–410, 2007.

[114] K. Preston, B. Schmidt, and M. Lipson. Polysilicon photonic resonators for large-scale 3d integration of optical networks. *Opt. Express*, pages 17283–17290, 2007.

[115] Nicolas Martin, Christophe Rousselot, Daniel Rondot, Franck Palmino, and Ren Mercier. Microstructure modification of amorphous titanium oxide thin films during annealing treatment. *Thin Solid Films*, 300(12):113 – 121, 1997.

[116] Qimin Quan, Irfan Bulu, and Marko Lončar. Broadband waveguide qed system on a chip. *Phys. Rev. A*, 80:011810, Jul 2009.

[117] A.H.J. Yang, S.D. Moore, B.S. Schmidt, M. Klug, M. Lipson, and D. Erickson. Optical manipulation of nanoparticles and biomolecules in sub-wavelength slot waveguides. *Nature*, 457:71–75, 2009.

[118] T. Alasaarela, T. Saastamoinen, J. Hiltunen, A. Säynätjoki, A. Tervonen, P. Stenberg, M. Kuittinen, and S. Honkanen. Atomic layer deposited titanium dioxide and its application in resonant waveguide grating. *Appl. Opt.*, 49(22):4321–4325, Aug 2010.

[119] Yi Cui, Mikael T. Bjrk, J. Alexander Liddle, Carsten Snnichsen, Benjamin Boussert, and A. Paul Alivisatos. Integration of colloidal nanocrystals into lithographically patterned devices. *Nano Letters*, 4(6):1093–1098, 2004.

[120] Robert Plass, Serge Pelet, Jessica Krueger, Michael Grtzel, and Udo Bach. Quantum dot sensitization of organicinorganic hybrid solar cells. *The Journal of Physical Chemistry B*, 106(31):7578–7580, 2002.

[121] Shengye Jin and Tianquan Lian. Electron transfer dynamics from single cdse/zns quantum dots to tio2 nanoparticles. *Nano Letters*, 9(6):2448–2454, 2009. PMID: 19453136.

[122] B. O. Dabbousi, J. Rodriguez-Viejo, F. V. Mikulec, J. R. Heine, H. Mattoussi, R. Ober, K. F. Jensen, and M. G. Bawendi. (cdse)zns coreshell quantum dots: synthesis and characterization of a size series of highly luminescent nanocrystallites. *The Journal of Physical Chemistry B*, 101(46):9463–9475, 1997.

[123] Daniele Gerion, Fabien Pinaud, Shara C. Williams, Wolfgang J. Parak, Daniela Zanchet, Shimon Weiss, and A. Paul Alivisatos. Synthesis and properties of biocompatible water-soluble silica-coated cdse/zns semiconductor quantum dots. *The Journal of Physical Chemistry B*, 105(37):8861–8871, 2001.

[124] C.C. Evans, K. Shtyrkova, J.D. Bradley, E. Ippen, and E. Mazur. Spectral broadening of femtosecond pulses in polycrystalline anatase titanium dioxide waveguides. In *Advanced Photonics Congress*, page JW4D.4. Optical Society of America, 2012.

[125] S Pezzagna, B Naydenov, F Jelezko, J Wrachtrup, and J Meijer. Creation efficiency of nitrogen-vacancy centres in diamond. *New Journal of Physics*, 12(6):065017, 2010.